POLITECNICO DI MILANO
DEPARTMENT OF AEROSPACE SCIENCE AND TECHNOLOGY
DOCTORAL PROGRAMME IN AEROSPACE ENGINEERING

GRID-SEARCH APPLICATIONS FOR TRAJECTORY DESIGN IN PRESENCE OF FLYBYS

Doctoral Dissertation of:
Davide Menzio

Supervisor:
Prof. Camilla Colombo

Tutor:
Prof. Biggs James Douglas

The Chair of the Doctoral Program:
Prof. Pierangelo Masarati

Academic year 2018/19 – cycle XXXII

Dedicated to the love of my life, Sara, who gave me the joy of my life, Ilyas.

Abstract

In the design process of a deep-space exploration mission, two phases can be distinguished: an interplanetary cruise and a final phase in planetary moon-system. In both cases the flyby manoeuvres have a positive impact on the overall mission cost and the scientific return.

This doctoral dissertation focuses on methods, techniques, and tools for modeling the trajectory in presence of flybys. Depending on the gravitational model used and the mission scenario foreseen, various part of the search space can be analysed and different insights derived about the nature of the third-body interaction. The ability of one method to reveal insights on the dynamics depends on the choice of the performance parameters and control variables used to study the trajectory evolution under the effect of the dynamics. Optimisation is a necessary step to confirm/disprove the solution proposed in the preliminary design, derived in simpler dynamics, by evaluating its applicability in the full-body one. While, generally, the inference process is deductive and moves from the model to the data, under specific conditions, the inductive stream can be followed. The improved understanding of the dynamics might positively affect the design process. Petal rotations are a clear example of a technique derived in patched conics, confirmed by the optimisation and later identified into periodic orbits. Crank-Over-Top sequence the one of a not proper modelling.

This work deals with grid-search approaches for the identification of feasible flyby. The main theme encompassing the dissertation regards the reduction of the computational effort associated to the scanning of the search space. We present a three-steps solution: recombining the search spaces associated to the pre- and post-encounter trajectories, switching from an epoch-based parametrisation of the search space to an orbital elements formulation and implementing pruning techniques, based on bounding regions defined by delta-v levels and orbital elements variations derived for limiting cases of the flyby. Following this logic, the 3D Flyby map is developed to study flyby in the three-body dynamics, to compare difference in the patched conics modelling of the flyby effect, and to design the sequence of resonant flybys for Europa Clipper tour. The different effect of direct and retrograde flybys on the post-encounter trajectory and the higher efficiency of the former represent the most significant observations.

Sommario

NELLA fase di progettazione di una missione di esplorazione dello spazio profondo, si possono distinguere due fasi: un trasferimento interplanetario e un fase finale nel sistema di lune orbitanti il pianeta considerato. In entrambi i casi, la fionda gravitazionale incide positivamente sul costo complessivo e sulla ricerca scientifica condotta della missione.

Questa tesi di dottorato si concentra su metodi, tecniche e strumenti per modellare la traiettoria in presenza di flyby. A seconda del modello gravitazionale utilizzato e dello scenario di missione previsto, è possibile analizzare varie parti del search-space e ricavare diverse intuizioni sulla natura dell'interazione col terzo corpo. La capacità di un metodo di rivelare intuizioni sulla dinamica dipende dalla scelta dei parametri di performance e delle variabili di controllo utilizzate per studiare l'evoluzione della traiettoria sotto l'effetto della dinamica. L'ottimizzazione è un passo necessario per confermare/confutare un disegno preliminare d'orbita, ricavato in una dinamica approssimata, valutando la sua bontà in uno ad alta fedeltà. Mentre, in generale, il processo di inferenza è deduttivo e passa dal modello ai dati, in condizioni specifiche, il flusso induttivo può essere seguito. La migliorata comprensione della dinamica può influenzare positivamente il processo di disegno dell'orbita. Le petal rotations sono un esempio lampante di modello derivato in una dinamica approssimata (patched conics), confermato poi dall'ottimizzazione e solo successivamente identificato come orbita periodica. La sequenza Crank-Over-Top, al contrario, è l'esempio di un modello non adatto.

Questo lavoro si occupa di metodi di ricerca a griglia per l'identificazione di flyby attuabili. Il filo conduttore della disertazione riguarda la riduzione dello sforzo di calcolo associato alla scansione del search-space. Presentiamo una soluzione a tre fasi: la ricombinazione dei search-spaces associati alle traiettorie di precedenti e successive al passaggio ravvicinato, il passaggio da una parametrizzazione temporale del search-space ad una formulazione in elementi orbitali e l'implementazione di tecniche di pruning, basate su regioni di delimitazione definite dal delta-v e dalla variazione di elementi orbitali derivata per caso limite del flyby. Seguendo questa logica, la 3D Flyby map è stata sviluppata per studiare il flyby nella dinamica dei tre corpi, per confrontare le differenze rispetto alla modellazione patched conics dell'effetto del flyby e per progettare

sequenze di flyby risonanti per il tour Europa Clipper. Il diverso effetto di flybys diretti e retrogradi sulla traiettoria successiva al passaggio ravvicinato e la maggiore efficienza dei primi rispetto ai secondi rappresentano le riflessioni più significative.

Acknowledgements

First of all, I would like to express a special thanks to my advisor Prof. C. Colombo for being a constant example of perseverance, patience and for having taught me that a good researcher is not the one who never falls, but the one who, after falling, finds the strength to get back up.

My thanks extend to the staff and colleagues of the Dept. of Aerospace Science and Technology of the Politecnico di Milano for their priceless advice for both my career and my research activity, especially to Prof. F. Bernelli and M. Lovera.

Ialso acknowledge the contribution of my dissertation reviewers Prof. G. Avanzini and M. Lo for their comments and brilliant suggestions.

Part of this research was carried out at the Jet Propulsion Laboratory. A heartfelt thanks goes to Dr. Stefano Campagnola for our countless discussions which guided me in my research and addressed me in my future career. A special thanks to the other colleagues of the Outer Planet Mission Analysis Group, in particular to Jon, Martin, Anastassios, Etienne, Ricardo and Brian and to those sharing with me trailer, Javier, Anton, Sebastian, my fellows Kenshiro and Cristian.

I am grateful to all friends who supported me and encouraged me to strive towards my goal. A truly thank goes to Fabio, Diogene, Matteo, Siemeng, Stefan, Ioannis, Juan, Elisa, Narcis, Mirko, Gabriella, Marco and Kharthik.

Wholehearted and deeply thanks are directed to my entire family. Mum and dad, thanks for all your support and the sacrifices you have made and being such a good grandparents. To my mother in law that became my second family for her constant support and delicious dinners. To my little sisters Fatima, Martina, and Nadia for being supportive and "infinitely" patient. Thank you grandparents Anna, Lino, Augusto, and Emilia I know that wherever you are, you are proud of me.

To my brothers Noor, Ahmed, Osama, Faroq, Mohammed and Bilal and in general to the ASM for our prayers together.

The deepest gratitude goes to my beloved wife Sara who guided me in the dark moment and gift me with the strongest source of light and joy I could possibly desire, my lovely Ilyas.

The doctoral research presented in this thesis has received funding from the European Research Council (ERC) under the European Unionâs Horizon 2020 research and innovation programme as part of project COMPASS (Grant agreement No 679086). Ermenegildo Zegna Founders Scholarship has to be acknowledged for sponsoring part of the visiting period at the Jet Propulsion Laboratory.

Contents

Bibliography **95**

List of Figures

List of Tables

List of Acronyms

CR3BP Circular Restricted Three-BodyProblem

COTs Crank-over-the-top sequences

FTC Feasible Transfer Condition

HTO Hohmann Transfer Orbit

MGA Multi Gravity Assist

NASA National Aeronautics and Space Administration

NEA Near-Earth-Asteroids

SMD Space Manifolds Dynamics

SOI Sphere of Influence

S/C Spacecraft

CHAPTER 1

Introduction

1.1 Background

Since the beginning of space exploration, analysts have widely exploited gravity assist in the trajectory design of deep-space mission to reduce the propellant consumption and contain the overall mission cost. The idea behind the flyby consists in leveraging the interaction with the gravitational field emitted by a secondary body in order to modify the trajectory of the S/C(Spacecraft) with the respect to the primary body in a predictable manner. Historically, we have seen a constant increase in the complexity of the trajectory of deep-space probes driven either by a reduction of the budget allocated to the mission, or by an increase in the mission objectives and tasks. When the technological progress, alone, does not allow to accommodate the increasingly complex mission scenarios, innovative trajectories are implemented and exploit the multi-body dynamics with planetary flybys.

Although gravitational perturbations had been known and observed altering the trajectory of comets since the eighteenth-century, the first theorisation of the flyby technique is attributed to Kondratyuk [39] and described the possibility of escape/capture via an exchange in momentum between the S/C and the body at which the close encounter is performed. However, a systematic implementation of the flyby in the trajectory design did not take hold until the development of the patched conics theory by

Minovitch [51]. In his work, the alteration in orbital velocity of the S/C is a consequence of the change in the system of reference due to the passage from the influence of a body to another. Nevertheless, it is through Battin's work [6] and the successful execution of flybys at Venus and Jupiter by Mariner 10 and Pioneer 11, respectively, that the flyby technique was consecrated in astrodynamics literature, and played a key role in reducing the fuel consumption for several deep-space missions.

Depending on the phase of the mission, the flyby is exploited in different ways. During the interplanetary journey, its effect is mainly used to accelerate/decelerate the S/C in order to target another encounter opportunity, modifying significantly the orbital shape in semi-major axis and eccentricity, and to ultimately escape/get captured as theorised by Kondratyuk [39]. Several successful missions executed interplanetary flyby to reach and study the gas giants [25,47,53] and go beyond [32,38], to target NEA (Near-Earth-Asteroids) [49, 60, 67] and the inner rocky planets [30]. However, the advent of the exploration of planetary moon system tour has created new scenarios for the inclusion of flybys in the trajectory design. Galileo's moon-tour of the Galilean moons represents the first application of the flyby driven by science objectives [8, 28, 33]. The improvement in the understanding of the flyby dynamics and the exploitation of its effect in the trajectory design is evident with Cassini's tour [73]. Its trajectory achieved capabilities never seen before, effectively reducing the propellant consumption, obtaining impressive results targeting low-altitudes passages at small bodies with limited bending power and performing valuable observations. These achievements allowed the NASA (National Aeronautics and Space Administration) to extend its mission for seven more years [15]. Europa Clipper, in the end, represents the culmination of the flyby employment as a result of the maturity in flyby knowledge and understanding. The trajectory design, indeed, is stressed by an extremely complex mission scenario in which the use of flybys in the trajectory design is tailored to satisfy specific scientific, mission and safety requirements, otherwise not met, while delta-v is drastically decreased [12–14].

The complexity of the mission scenario of Multiple-Gravity Assisted (MGA) trajectories makes difficult to perform a comprehensive search of feasible transfers in a multi-dimensional solution space that is further constrained by all the trajectory requirements [22]. Several methods were proposed to solve MGA (Multi Gravity Assist) trajectories. Ahead of analysing them in detail, it is important to provide a first categorization of such approaches.

A first demarcation line, about the different approaches described in the literature, can be drawn by distinguishing search methods from global optimisation approaches. While the former aim to outline the solution space and identify the feasible trajectories,

scanning through its possibilities point-by-point, the latter instead, navigate through the search space seeking for the point solution that minimises a predefined performance index. If the search space is properly mapped, search solutions are always globally optimal [46], yet less accurate when compared to global optimisation solutions. Nevertheless, accuracy can be restored by local optimisation in the post-processing, making the two methods interchangeable.

Another difference concerns the type of MGA problem that is approached to be resolved. In particular, planning represents the mission scenario and is opposed to scheduling, which identifies the optimal configuration of the trajectory in time and satisfies the mission scenario [46]. In the first case, the designer attempts to identify the number and sequence of flybys enambling a given mission scenario, while in the latter case, he exploits the sequence of planet identified in the planning step to resolve the phasing for a specific time frame. The identification of the optimal trajectory, that satisfies the requirements while minimising the cost function, is the result of an iterative process between planning and scheduling, making them the two sides of the same coin.

Lastly, a further distinction can be made on the dynamics, which describe the laws of motion of the S/C as a result of the interaction of its propulsion system with the gravitational model adopted. The two effects on the S/C trajectories are considered as decoupled, in order to better guide the reader through this overview of the methods relevant to the work presented in this disseration. A different design approach is considered depending whether the S/C is powered with an impulsive or low-thrust propulsion system and whether a patched conics or three-/n-body problem dynamics is taken into account.

Graphical methods represent a special class of search technique, which appear particularly appealing for the possibility to provide insights on the flyby dynamics. In particular, contour plots offer an immediate visualisation of the optimal trajectories by displaying the trend of the performance index, e.g the delta-v, against two variables that fully define the trajectory, for instance the epoch of departure and arrival. The most simple example of graphical methods applied to trajectory design is the porkchop plot [72].

Conic approximation represents the baseline for MGA trajectories design. Branch and bound techniques are applied to construct the transfer orbit as a sequence of Keplerian arcs connecting two minor bodies but remaining bounded to the dynamics of primary, larger body. Flybys resolves the velocity discontinuities at each conjunction with the secondary, smaller body. The patched conics model applied to flyby trajectories relies on the simple hypothesis of the Sphere of Influence (SOI), which is used to split the space in different domains within which only one body governs the laws

of motion. The transfer orbit far from the secondary body can be considered as beam of an infinite number of trajectories associated to all the possible arrival conditions at the secondary body that generate a tube of infinitesimal radius. This concept explains that far from secondary body all the entry conditions at the secondary coexist and that the desired one can be targeted with no or significant small correction. Switching from one arrival condition to another is inexpensive far from the secondary. Different approaches used a variety of orbital parameters derived from the Keplerian elements to study the effect of the flyby on the overall trajectory: the asymptotic distance Δ and the radius of periapsis r_p, the b-plane coordinates, η and ξ, pump and crank angles, α and κ respectively. Depending on the parameter used, different graphical methods were developed. The period-periapsis map ($P - r_p$) [34, 55] and the Tisserand graph ($T - r_p$) [65] address the planning of the MGA trajectories by displaying the trajectory variation induced by several close encounters and grouping flybys in different families according to the disposition of their orbits in the plot. The difference between the three methods consists in whether they can handle elliptic [34, 55, 65], parabolic [34, 65] and hyperbolic orbits. The v-infinity sphere [64] and the leveraging graph [19] display the effect of the flyby on the post-encounter orbit for arbitrary phasing [42] against the asymptotic velocity coordinates. The b-plane in the end allows to identify hazardous close passages that could eventually lead to a collision [69].

The simplicity of the patched conics method presents a great advantage, as it allows to describe the S/C motion by invariant quantities, but several drawbacks.Indeed, it offers a limited understanding on the chaotic nature of the interaction between two or more gravitational fields and constrains the design of flyby to high energy ones.

Differently from the two-body dynamics, in the three-body dynamics the total energy is the unique invariant of motion. Such condition prevents to describe the trajectory analytically and requires to numerically propagate the S/C trajectory from an initial state to study its evolution in the three-body dynamics. Studying the complete search space of the state vector can be computationally intensive, therefore, depending on the application, different methods have been developed to scan the solution space and grasp insights on the dynamics of the close encounter in the three-body dynamics.

SMD (Space Manifolds Dynamics) studies the natural transportation of the system at very low energy via invariant manifolds and exploits homoclinic and heteroclinic connections to link trajectories from different domains [40, 41]. An alternative to the SMD methods that stick to three-body dynamics for the trajectory design, consists in approximating the dynamics by mapping the effect of the third body perturbation on an osculating orbit, parametrised by the Keplerian elements. Depending on how the gravitational interaction is modelled, it is possible to distinguish between two classes

of methods: semi-analytical or fully numerical methods, accordingly. On one side the Keplerian [2, 59] and on the other the Flyby map [21]. The Tisserand-Poincaré graph [20] represents, instead, an upgraded version of the Tisserand graph derived for the three-body dynamics.

All the methods listed so far belong to the search category. Tackling the scheduling problem with a search approach could appear a good strategy, since exhaustive insights can be derived about the dynamics and a global optimal solution can be identified. However, most of the methods appear extremely sensitive to the grid discretisation, making the search of feasible flyby computationally prohibitive when a finer resolution is desiderable [23, 24]. Nevertheless, other methods were proposed to effectively constraint the search space by limiting the time-of-flight (ΔT) [7], the relative velocity at the flyby (v_∞) [35], the total delta-v (Δv) directly [3], the semi-major axis or some other orbital quantity [22, 70].

Table 1.1 gathers the contributions, that were introduced in this paragraph and are relevant for this dissertation, and frames them in the five categories previously identified. In particular, the publications are distinguished depending whether the authors adopted a grid search or global optimisation method, to schedule (ϕ) or plan (E) the trajectory design of S/C powered by impulsive (High) or low-thrust in patched conics (2B) or three-body (3B) dynamics and whether specific visualisation tools are employed to represent the feasible flyby solution determined by the method adopted.

Table 1.1: *Relevant methods for flyby trajectory design.*

	Method		Problem		Dynamics				graphical methods
					Gravity		Propulsion		
	grid	opt	ϕ	E	2B	3B	High	Low	
VILM [63]	x			x	x		x		
$P - r_p(E < 0)$ [55]	x			x	x		x		x
$P - r_p(E \leq 0)$ [34]	x			x	x		x		x
$T - r_p(\forall E)$ [65]	x			x	x		x		x
b-plane [69]	x			x	x		x		x
ΔT pruning [7]	x		x		x		x		
$e^{\sin}$ shape-based [54]	x		x		x			x	
v_∞ pruning [35]	x		x		x		x		
Keplerian map [59]	x		x			x	x		x
v_∞ sphere [64]	x			x	x		x		x
Δv pruning [3]	x				x				
Leveraging graph [19]	x		x		x		x		x
T-P graph [20]	x		x	x		x	x		x
Keplerian map refinement [45]	x	x	x			x	x		
Flyby map [21]	x		x			x	x		x
Kick map [2]	x		x			x	x		

1.2 Research questions

The objective of this doctoral research consist in exploiting graphical methods applied to the design of interplanetary trajectories, on one side, to improve the understanding of the dynamics and, on the other, to revisit the design process.

Considering the objectives set, this dissertation reviews the mechanisms employed by the trajectory design in presence of flyby. To do that, the process generating optimal flyby solutions is analysed from the simplest and most basic tasks, e.g in patched conics the Keplerian arc associated to the two-point boundary value problem (2PBVP). In this context, it can be observed that the main search approach applied to the Lambert's problem for different departure/arrival condition identifies a significan number of solutions with high delta-v. Therefore, the present work aims to address the possibility to identify a priori a region of the solution space with low delta-v and to improve an epochs-based search of feasible trajectories.

The next step focuses on the flyby examining whether the resolution in cascade of the pre- and post-encounter trajectories from the epochs triplets (departure, flyby, arrival) could not be performed differently and whether the possibility exists to evaluate the flyby of the transfer orbits itself, bypassing the close encounter distance and turning angle concepts.

In the end, the accuracy of the patched conics in modelling the effect of the flyby is questioned.

1.3 Research contribution and thesis organisation

The dissertation opens Chapter 2 with an analysis of the porkchop plot computed considering circular coplanar dynamics. In particular, the contribution of this thesis consists in the analytical determination of the location of the minimum delta-v and the characterisation of the shape associated to constant delta-v contour based on the solutions associated to tangential manoeuvre at the departure and arrival. Chapter 2 closes with the extension of the location and shape analysis from zero to multi-revolution transfers. The multi-revolution porkchop plot is generated.

Chapter 3 deals with the problem of the flyby: a recombination of the solutions associated to incoming and outgoing transfer legs, resolved in parallel, is performed at the common time of flyby. A modelling of the trajectory as an inverse Lambert problem is presented and legitimated by the fact epochs-based search is inefficient. A method to evaluate the effect of a flyby in terms of Keplerian elements is provided and Gauss' planetary equations derived for the flyby acceleration concludes the chapter.

A pruning technique based on the creation of a delta-v bounding region from the

tangential solutions is offered in Chapter 4 and it is based on the observation that epochs-based search identifies a solution space characterised by high delta-v while low delta-v trajectories are confined into the neighbourhood of the minimum location. A root-finding method is then applied for the refinement of the delta-v bounding region in circular coplanar dynamics, but also for the real ephemerids model. In this way, the pruning of direct trajectories is extended to transfer with flybys, modifying the generation of the delta-v bounding region and improving it with limits derived by Gauss' Variational equation.

In Chapter 5, the effect of the flyby is studied with CR3BP (Circular Restricted Three-BodyProblem) dynamics. An extended version of the Flyby map is offered to account for the out-of-plane dynamics. Chapter 5 concludes with the comparison between the flyby effect numerically integrated and the one modeled by patched conics.

Chapter 6 accounts for different techniques for the refinement or optimisation of the trajectory that were developed during the research: two different strategy for the flyby optimisation, a root-finding approach for the extraction of the resonant flyby from the flyby map and a continuation method based on psuedo-arclength parametrisation for the identification of families of flyby at prescribed close approach distance. An application of the Flyby map to Europa Clipper tour design is shown in Chapter 7. Chapter 8 provides final remarks and conclusions on the most relevant findings of the work.

1.4 Bibliography disclaimer

During the years of my Philosophiae Doctor (PhD), I presented updates of my work in many conferences. Major part of this work have been extended and is currently have been submitted for review to scientific journals or are about to be submitted. The most significant publications are listed below.

Journal Publication

- D. Menzio and C. Colombo, "New insights on the porkchop plot andits possible applications." Celestial Mechanics and Dynamical Astronomy, To be submitted
- D. Menzio, S. Campagnola, and C. Colombo, "Flybys in the spatialcircular restricted three body problem." Journal of Guidance, Control and Dynamics, To be submitted
- D. Menzio and C. Colombo, "Pruning techniques to reduce the porkchop plot search space." Celestial Mechanics and Dynamical Astronomy, To be submitted
- D. Menzio, S. Campagnola, and C. Colombo, "An application ofthe flyby map to

europa clipper tour design." Journal of Guidance, Control andDynamics, To be submitted

Conference Proceedings

- D. Menzio and C. Colombo, "The combined lambert-tisserand method applied tothe single flyby problem". In IAC proceedings, 2017. Presented at the International Astronautical Congress, Adeilade (AU).
- D. Menzio and C. Colombo, "An analysis of the pork-chop plot for direct, multi-revolution and fly-by missions." In Advance in the Astronautical Sciences, pages 1739 1753, 2018. Presented at the 4th IAA Conference on Dynamics and Control of Space Systems in Changsha (CN).
- D. Menzio and C. Colombo, "Adapted syzygy functions for the preliminary de-signof multi gravity assists trajectories." In IAC proceedings, 2018. Presented at the International Astronautical Congress in Bremen (DE).
- D. Menzio and C. Colombo, "Flybys in the spatial circular restricted three body problem. In AAS/AIAA proceedings, 2018. Presented at the Astrodynamics Specialist Conference in Portland (USA).

Part I

Interplanetary cruise

CHAPTER 2

Insights on the targerting problem

The porkchop plot is a useful visualisation tool that allows to analyse transfer orbit with respect to different performance parameters, such as the characteristic energy at the departure and at the arrival, the total delta-v, transfer duration, the maximum distance to Sun, etc. [27]. In its most common application, the porkchop plot is used to represent the characteristic energy, C_3, associated to different departure and arrival conditions for a specific targeting problem. It is due to its distinctive shape, resembling indeed to a steak of meat, which earned the chart such a peculiar name [72].

An extensive literature about this subject is not available per se, but it is associated to studies on the geometrical interpretation of the Lambert's problem. Literature is available about its formulation [4, 5, 50], its extension to handle different trajectory scenarios (e.g. multi-revolutions trajectories [10,62] and low-thrust coast arc [58]), and its application to real missions (to Mars, [1, 48, 74], Near Earth Asteroids [29, 66, 75], Jupiter [26] and beyond [63, 72]).

The first use of the porkchop plot dates back to the Voyager missions [72], when it was developed with the specific purpose of intercepting Saturn within 1981, but avoiding close encounters on some particular dates, such as Thanksgiving and Christmas.

Despite more than four decades of use, the porkchop plot is not currently exploited at its full potential. Indeed, the majority of algorithms available in the literature for

resolving the targeting problem presents a large portion of the solution space affected by a large delta-v. Understanding the effect of the dynamics on the delta-v distribution could be exploited to limit the search space and to improve the search algorithm. The possibility to know the location of the delta-v minima a-priori and to have an indication of the contour regions occupied by specific delta-v level would be extremely advantageous and could prevent to resolve the Lambert's problem for all the grid points of the search space. In this way, it would be possible to avoid unnecessary computations for solutions that are known in advance to be not optimal. Moreover, additional minima could be included if multi-revolution transfer are considered.

Therefore, the following sections offer an analysis of the porkchop plot that aims to investigate the location of the minimum delta-v solutions. The shape of constant delta-v contour lines are evaluated with respect to the solutions associated to tangential manoeuvres. Moreover, multi-revolution transfers are considered where the time of flight, and in turn the delta-v, grows to such an extent as to invalidate the use zero-revolutions trajectories. Indeed, the porkchop plot can be filled with additional minima obtained stacking the multi-revolution solutions on top of the zero-revolution ones.

2.1 Analysis of the classical porkchop plot

The general definition of a porkchop plot is a chart displaying the contour lines at constant total delta-v against different combinations of departure/arrival dates. Each pair defines univocally a transfer orbit. The porkchop plot can be considered as the first graphical methods employed in mission analysis to obtain an immediate and clear identification of the regions of the solution space satisfying a specific requirement, e.g. low delta-v. In fact, the porkchop plot represents against a grid of different departure and arrival dates the numerical solution of several targeting problems, most commonly known as Lambert's problems. Their solution was derived by Lagrange manipulating the Kepler's equation for the transfer time, see Eq.2.1:

$$\begin{gathered}\sqrt{\frac{\mu}{a^3}}\Delta t = \alpha - \beta - (\sin\alpha - \sin\beta) \\ \sin\alpha = \sqrt{\frac{s}{2a}} \quad \sin\beta = \sqrt{\frac{s-c}{2a}}\end{gathered} \tag{2.1}$$

The semi-major axis, a, is found from the non-linear Kepler equation, as a function of the time of flight, Δt, the gravitational parameter, μ, and the values of the eccentric anomalies on the rectilinear ellipse, α and β. These angles are geometrical terms functions exclusively of the semi-perimeter, s, and the chord, c, of the so called space triangle which depend only on the departure and arrival positions [57].

Although the porkchop plot is generally the final result of a grid-search algorithm

applied to several Lambert's problems, the trend of the delta-v solutions can give insights on the dynamics of the problem. This information can be used to reduce the dimensionality curse by which brute-force techniques are generally affected.

To have a clear understanding of the solutions represented by the porkchop plot, some simplifications must be introduced. Hence, circular and coplanar trajectories are considered here in order to restrict the trend of the delta-v solutions to the smallest numbers of variables. Comparing the results obtained from real and simplified ephemerides, one can observe from Fig. 2.1 how the real eccentricity and inclination of the departure and arrival planet's orbits spoil the smoothness of constant delta-v contour lines associated to the circular coplanar case. The assumed simplified shape does not capture the topology of the contour obtained for the real ephemerides. In fact, the inclination difference between the departure and arrival orbits results in the vanishing of global minimum and the appearance of two local minima separated by a ridge, as it can be seen from Fig. 2.1. Nonetheless, considering the aim of this research focused on constraining the search space to a region of prescribed delta-v, one can observe that delta-v contour levels obtained from circular coplanar orbits approximate well the region occupied by similar/lower delta-v associated to real ephemeris. Therefore, the idea behind this work consists in locating the delta-v minima and characterising the area around it in terms of the shape of the contour lines with constant delta-v derived for the circular coplanar case.

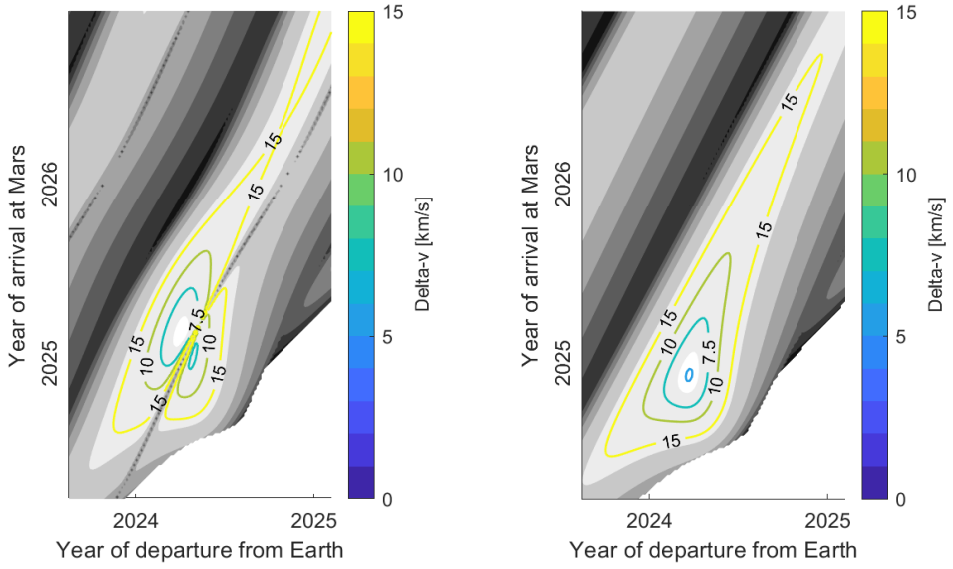

Figure 2.1: *The porkchop plot for a Earth-Mars transfer opportunity, obtained considering real (left) and simplified (right) ephemerids.*

The focus of the research moves from the search and characterisation of the delta-v minima to the identification of an approximate region derived for a simplified model

but containing the minima of the real case scenario, legitimating the analysis presented in this work.

2.2 An analytical solution for the locus of minimum delta-v

For circular coplanar orbits of the departure and arrival planets, orbital mechanics predicts that the Hohmann transfer is the solution with minimum delta-v [56], and is located at the intersection of the red dashed lines in Fig. 2.2.

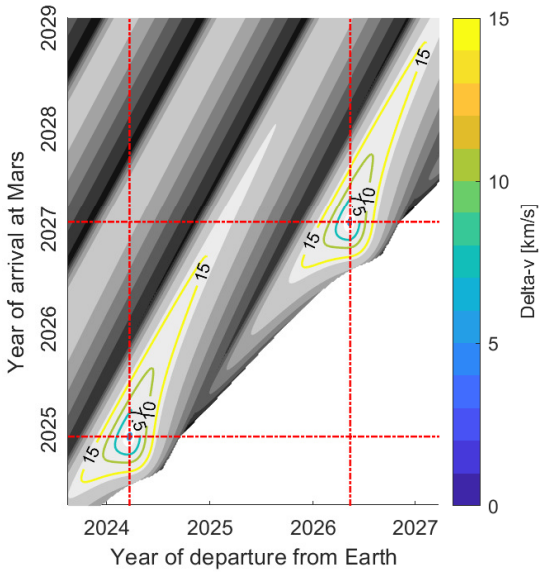

Figure 2.2: *The repetitiveness of the porkchop plot every synodic period, represented by evenly spaced red dash-dotted lines associated to the departure and arrival dates of different delta-v minima.*

Fig. 2.2 shows that the minimum delta-v solution repeats with the frequency of conjuction, f_{syn}. This quantity is associated to the synodic period of the system constituted by the departure and arrival planets and defined in Eq. 2.2:

$$f_{syn} = \frac{1}{2\pi}\left(\sqrt{\frac{\mu}{a_d^3}} - \sqrt{\frac{\mu}{a_a^3}}\right) \tag{2.2}$$

as the difference of mean motions of the departure and arrival planets, specified in the equations with the subscripts d and a, respectively. The angular speed of each planet is expressed as the square root of the gravitational parameter, μ, of the central body, divided by the semi-major axis a.

The characteristics of the HTO(Hohmann Transfer Orbit) can be summarised in two conditions: tangential thrust at the terminal points and minimum semi-major axis. Condition that for circular coplanar orbits is verified when the semi/major axis is equal to the average of the orbital radii of the departure and arrival planets. For the targeting problem, such conditions can be translated into purely geometrical relations, allowing

to derive an analytical expression for the minimum delta-v solution as a function of the departure and arrival epochs, t_d and t_a, and orbital radii, r_d and r_a:

$$\begin{cases} t_a = t_d + \pi\sqrt{\frac{(r_d+r_a)^3}{8\mu}} \\ \sqrt{\frac{\mu}{r_a^3}}t_a = (\sqrt{\frac{\mu}{r_d^3}})t_d - (\varphi_a(t_0) - \varphi_d(t_0) - \pi) \end{cases} \tag{2.3}$$

In Eq. 2.3, φ represents the angular phasing measured from the vernal equinox, Υ, at the initial time t_0 from which the time of departure t_d is computed. The two conditions, which will be called from now on with the symbolic expression Δt_{HTO} and $\Delta\varphi_\pi$, impose that the transfer time equals half a Hohmann period and that the phasing angle between the position vectors of the departure and arrival planets correspond exactly to 180 degrees.

Eq. 2.3 can be rewritten in non-dimensional units with respect to the arrival planet normalising the two equations with its mean motion:

$$\begin{cases} t_a = t_d + \frac{\pi}{\sqrt{8}}\left(\frac{r_d}{r_a}+1\right)^{1.5} \\ t_a = \left(\frac{r_a}{r_d}\right)^{1.5} t_d - \Delta\varphi \end{cases} \tag{2.4}$$

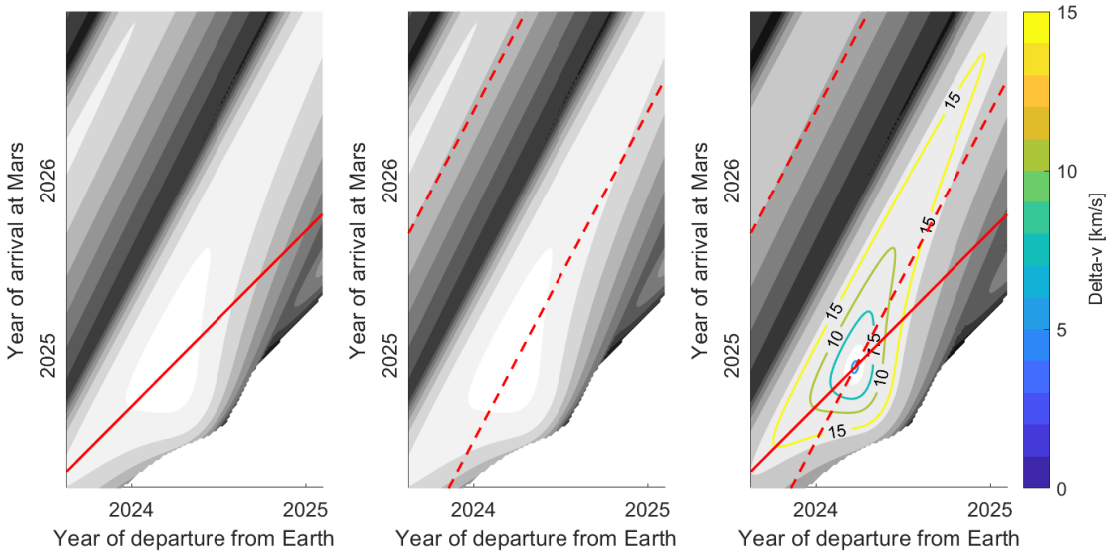

Figure 2.3: *The identification of the delta-v minimum at the intersection of Δt_{HTO} (on the left and on the right) and $\Delta\varphi_\pi$ (on the center and on the right) lines, determining the locus of the points with transfer time equal to half Hohmann period and with phasing angle difference equals to 180 degrees, represented with a continuous and broken line.*

The two geometric relations in Eq. 2.3 appears in the porkchop plot as two lines with different slopes, represented with a continuous and dashed line in Fig. 2.3. Their intersection determines the exact point at which the HTO takes place. Eq. 2.4 shows

that the location of the minimum delta-v solution in the case of circular coplanar orbits depends on only two parameters: the ratio between the orbital radii of the departure and arrival planets and the initial phasing angle difference.

It is interesting to note that the two parameters have a different effect on the Δt_{HTO} and $\Delta\varphi_\pi$ lines: the orbital radii ratio affects the y-intercept of the former and the slope of the latter while the initial phase angle difference influence only the y-intercept of the latter. The net effect of selecting a different departure/arrival planet is a translation in the arrival epoch, t_a, direction driven by the orbital radii ratio, $\frac{r_a}{r_d}$, for the Δt_{HTO} line and a coupled roto-translation induced by the orbital radii ratio, $\frac{r_a}{r_d}$, and the orbital phasing difference, $\Delta\varphi$, for the $\Delta\varphi_\pi$ line. Although, the arrival time adaptation preserves the repetitiveness of the delta-v minima with the synodic period, see Fig. 2.4, nevertheless, a modification of the shape of the constant delta-v contour lines is expected and will be addressed in the following paragraphs.

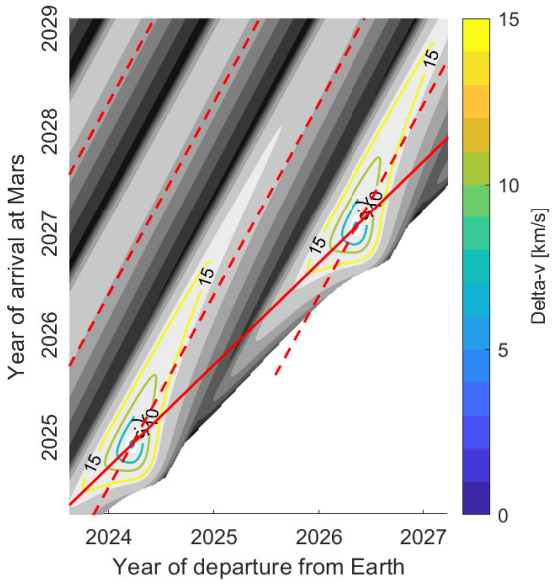

Figure 2.4: *The identification of two consecutive delta-v minimum based on purely geometrical relations.*

In conclusion, the main remark of this paragraph is that the location of minimum delta-v solutions is predictable with no need of solving any non-linear equations, but exploiting purely geometrical relations.

2.3 The analysis of the contour lines at constant delta-v

In the previous section, it was shown how it is possible to assess the position of the minimum delta-v solutions from the planets phasing and the time of flight. This paragraph focuses on how the contour lines assume such a characteristic triangle-like shape, in order to verify if it is possible to constraint the search space into a control region around

the delta-v minimum.

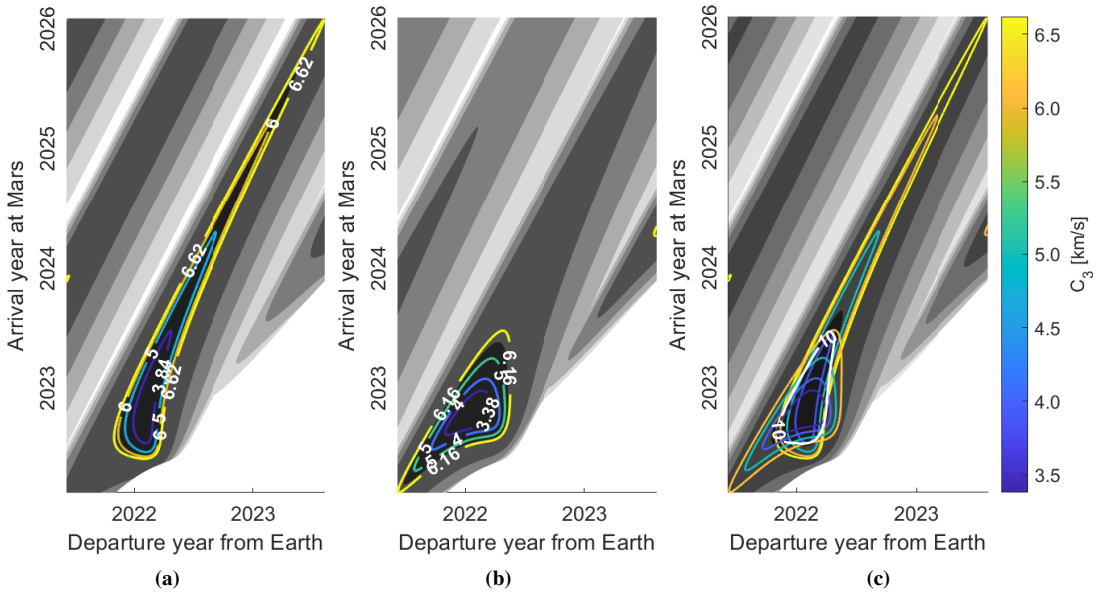

Figure 2.5: *The generation of a constant delta-v contour line (c) as the sum of the relative velocities at departure (a) and arrival (b) planets respectively.*

Given the definition of the characteristic energy $C_3 = \frac{v^2}{2} - \frac{\mu}{r} = \frac{v_\infty^2}{2}$ as the square of excess velocity, v, needed to escape from the gravitational attraction of a massive body on an orbit of radius r, Fig. 2.5 displays how each contribution of the relative velocities at the departure and at the arrival sum up to generate a delta-v contour line. Indeed, Fig. 2.5 shows that each delta-v contour line originates at the intersection of complementary levels in total delta-v for the departure and arrival relative velocities, which are deemed as those escape and capture manoeuvres whose combination equals exactly the total delta-v generating the the contour line of interest.

Fig. 2.6 represents pairs of complementary departure/arrival relative velocities with the same color and shows how a constant delta-v contour line is generated at the intersection of manoeuvres different in magnitude but whose sum is constant. Although, the relative velocities at departure and arrival explain the generation process of the single contour line, however, the motivation behind the contour shape remains hidden in the data. In fact, from the contour line of the relative velocities at departure and arrival it is impossible to address the effect of orientation of the manoeuvre on the delta-v. Indeed, the fundamental difference between tangential and secant manoeuvres lies in the need to correct either the shape or the orientation the transfer with respect to the departure/arrival orbit and is believed to play a central role in explaining the constant delta-v contour shape.

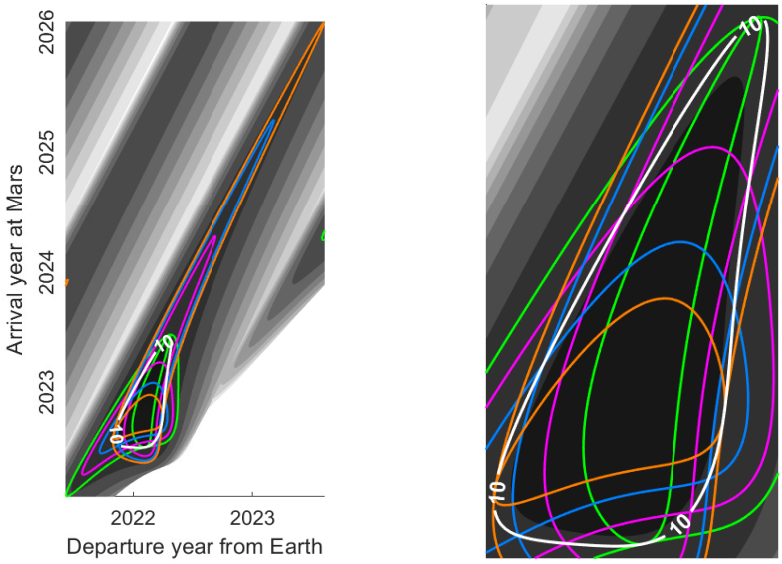

Figure 2.6: *The generation of a* 10 *km/s delta-v contour line from the complementary relative velocities at departure from Earth and arrival at Mars. In particular green, magenta, cyan and orange lines are associated to the pairs of manouevres with 3.84-6.16, 5.00-5.00, 6.00-4.00, 6.62-3.38 km/s delta-v respectively, identifying at their intersection the delta-v contour level represented with the white line.*

The indication of the manoeuvre direction can be obtained by representing the dates associated to a tangential manoeuvre at departure or arrival, displayed with the blue and green scaled lines in Fig. 2.7.

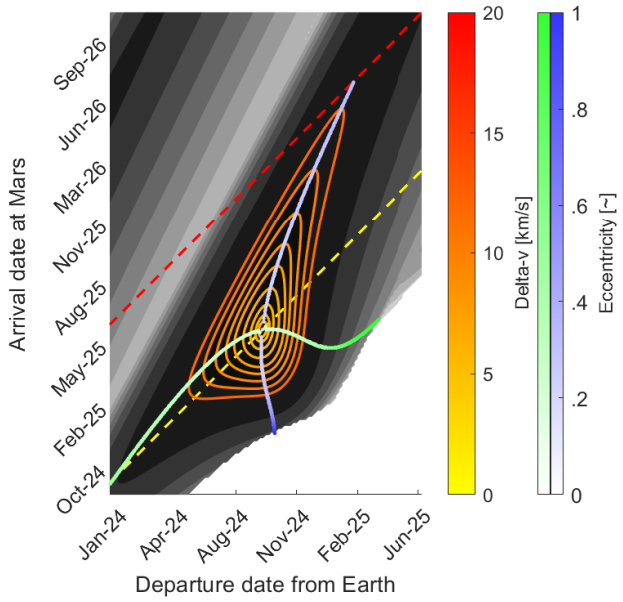

Figure 2.7: *The trend of constant delta-v contour lines over the solutions associated to tangential manoeuvres at departure or at arrival represented with in blue and green lines, respectively. The colour scaling is associated to the eccentricity of the transfer orbit and the yellow and red dashed lines show the* Δt_{HTO} *and* $2\Delta t_{HTO}$ *-lines, with the latter identifying an upper limit for zero-revolution transfers above which one-revolution solutions present a lower delta-v.*

By scaling the colour of the tangential solutions on the eccentricity, it is possible to note that, as expected, the intersection of the two curves occurs at the smallest eccentricity, condition that coincides with the delta-v minimum. Moving away from the intersection point, the eccentricity tends to increase. Tangential solutions provide interesting insights on the nature of the delta-v contour shape, in fact Fig. 2.7 shows that two of the three lobes of the delta-v contour line appear directed along one of the two extremities of each of the two lines, while the third looks to be encloses by the other two sides. Moreover, the greater elongation of the upper lobe with respect to the others can be explained by the fact that it is obtained where the manoeuvre is more effective, i.e. closer to the primary which in this case coincides with the departure.

Some intuitions on the lower-right vertex of the triangle-like shape can be derived by looking at the trend of the semi-major axis of the transfer orbit, represented on the background of Fig. 2.8 through its inverse normalised on the value associated to the Hohmann transfer in a grey scale contour fashion. In fact, it can be noted that the orientation of the third lobe is directed along the solutions presenting the semi-major axis of a HTO. However, for low time of flight, the transfer orbit exhibits an increase in eccentricity, as shown by the solutions for tangential manoeuvres ending in the areas associated to parabolic semi-major axes. Such regions shapes the sides of the third lobe of the constant delta-v contour line, giving it a sharp look.

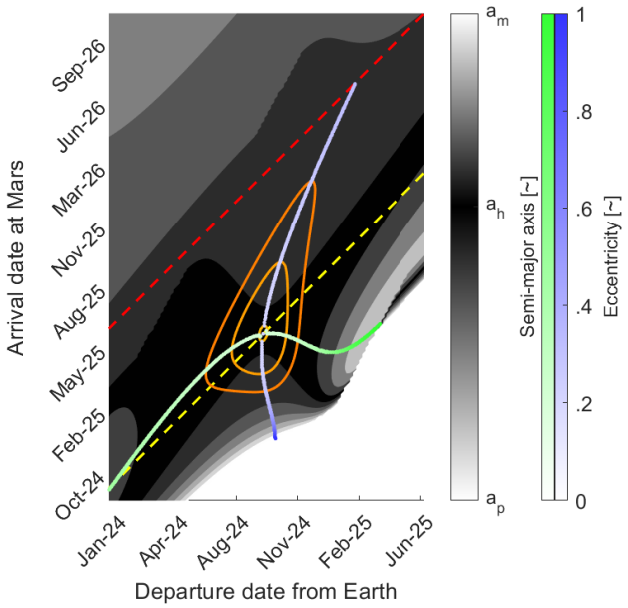

Figure 2.8: *The trend of the constant semi-major axis contour lines, represented through its inverse value scaled on the Hohmann transfer one, over the delta-v contour lines and the solutions associated to tangential manoeuvres at departure or at arrival represented with blue and green lines, respectively. The colour scaling is associated to the eccentricity of the transfer orbit and the yellow and red dashed lines show the Δt_{HTO} and $2\Delta t_{HTO}$ -lines, with the latter identifying an upper limit for zero-revolution transfers above which one-revolution solutions present a lower delta-v.*

In the end, it is interesting to note that, among the solutions lying on the constant delta-v contour line, those displaying tangential firing at the departure, which is expected to be more efficient, allow to perform a steeper secant manoeuvre at the arrival, see Fig. 2.9. At the same time, tangential manoeuvres at the arrival leave lower delta-v to switch from the initial orbit to transfer one and exhibit a milder angular difference between transfer and initial orbits. The "mixed" scenario implementing two secant manoeuvres can be considered as the transition phase between the departure and arrival tangential cases, just described.

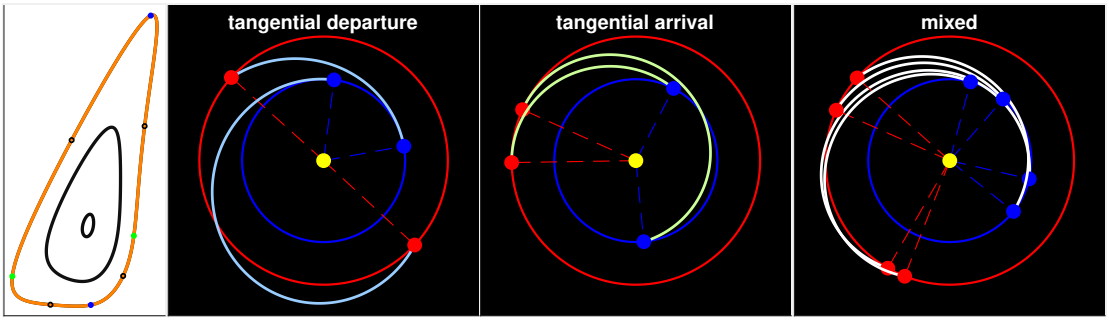

Figure 2.9: *The representation of the trajectories associated to a* 10 *km/s delta-v contour line. In blue, green and white the transfer orbits implementing a tangential manoeuvre at the departure or arrival or a secant manoeuvre, respectively.*

2.4 From the classical to the multi-revolution porkchop plot

When the time of flight is high enough, the Lagrange equation for the Lambert's problem, see Eq. 2.1, can be modified as following:

$$\sqrt{\frac{\mu}{a^3}}\Delta t = 2N\pi + \alpha - \beta - (\sin\alpha - \sin\beta) \tag{2.5}$$

where N takes into account the number of revolutions that the S/C is required to perform prior arrival to the target.

Fig. 2.10 provides an intuitive reason why considering multi-revolution solutions for an increased search space would be beneficial from a delta-v perspective. It displays the trend of semi-major axis and eccentricity against the time of flights for zero, one and two revolutions cases, represented with a continuous, dashed and dash-dotted lines respectively. It can be noted that, below a certain time of flight no solution is available for multi-revolution transfers. But as soon as the time grows enough, such trajectories present a lower semi-major axis and a lower eccentricity when compared with the solutions at fewer revolutions.

Multi-revolution trajectories, if exist, are more efficient in delta-v with respect to

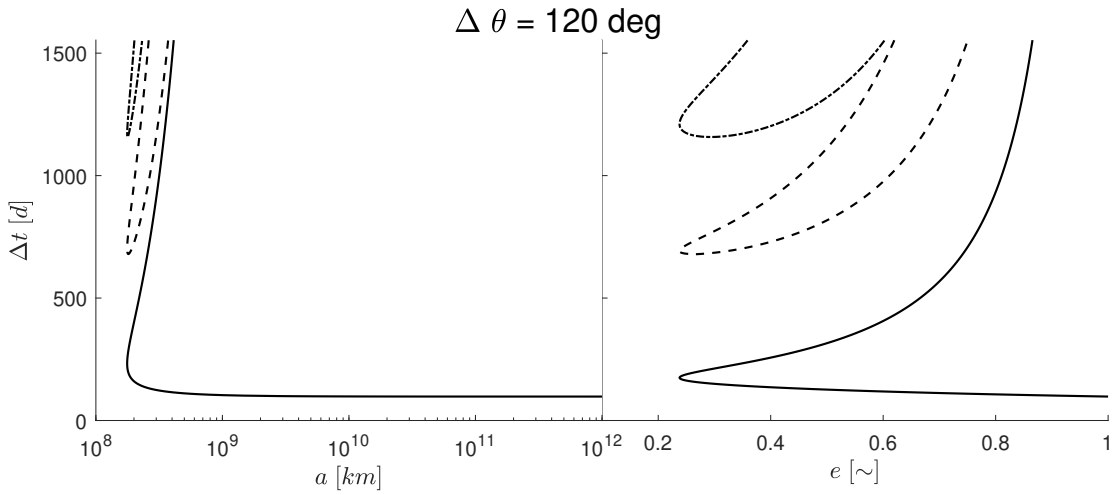

Figure 2.10: *The evolution of the semi-major axis (left) and eccentricity (right) with respect to the time of flight for an Earth-Mars transfer in* $120\,\mathrm{deg}$ *phasing configuration . The continuous, dashed and dash-dotted curves are associated to 0, 1 and 2 revolutions transfer trajectories, respectively.*

zero-revolutions solutions. As it can be seen from Fig. 2.10, for similar time of flights, zero-revolutions orbits require higher semi-major axis and eccentricities which in turn affect badly the delta-v [61, 62]. In the case study presented, a reduction of few tens of (between 10 and 50) km/s is obtained switching from a zero-revolution trajectories to another with one-revolution.

Differently from the zero-revolutions transfer that presents a monotonous trend of the semi-major axis and eccentricity with respect to the time of flight, i.e. any line parallel to x-axis identifies either one or zero intersection with the curve, multi-revolution trajectories present a short and long solutions depending on whether the S/C travels along the shortest or the longest path for a given orbit. In particular, when $\Delta\theta < \pi$, the upper/lower branch of the semi-major axis/eccentricity plot corresponds to the long transfers, while the lower/upper branch corresponds to the short ones, and vice versa for $\Delta\theta > \pi$ [62].

The identification of the minimum delta-v

Similarly to Eq. 2.5, the Δt_{HTO} term for the explicit solution of the minimum delta-v, see Eq. 2.4, can be modified to identify the locus of the points that present a time of flight equal to an odd multiple of half Hohmann period, as indicated in Eq. 2.6:

$$\begin{cases} t_a = t_d + \pi \frac{2N+1}{\sqrt{8}} \left(\frac{r_d}{r_a} + 1 \right)^{1.5} \\ t_a = \left(\left(\frac{r_a}{r_d} \right)^{1.5} \right) t_d - \Delta\varphi \end{cases} \tag{2.6}$$

Representing the smallest delta-v solutions obtained for a multi-revolution transfer on

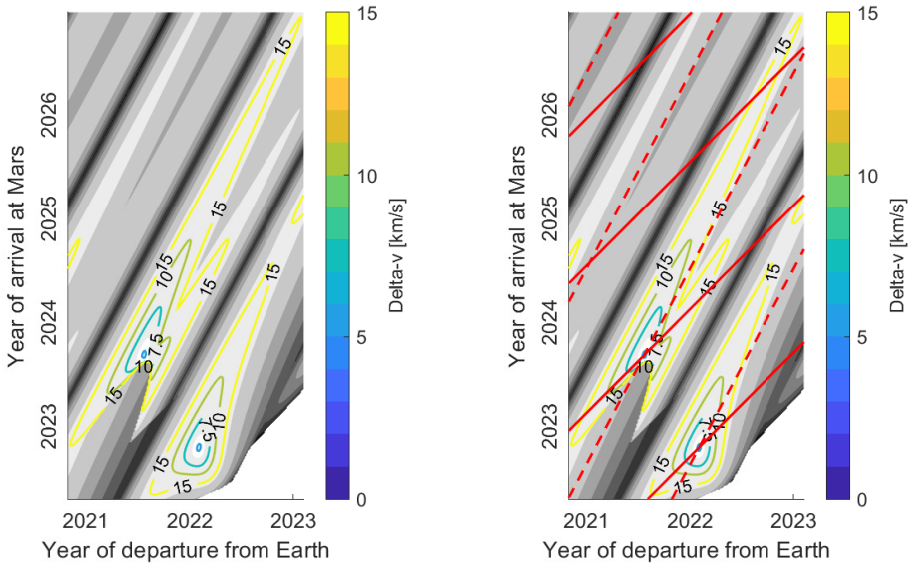

Figure 2.11: *On the right, the triangle-like and butterfly-like constant delta-v contour lines to the zero and one revolution transfers, respectively. On the left, the identification of the delta-v minima at the intersection of $n\Delta t_{HTO}$ and $\Delta\varphi_\pi$ lines, represented with a continuous and broken lines, respectively.*

the porkchop plot it is interesting to observe that the associated minimum is still centered at the intersection between $\Delta\varphi_\pi$-lines and $n\Delta t_{HTO}$-lines, where n is an odd number, i.e. $n = 2N + 1$, see Fig.2.11.

Analysis of constant delta-v contour lines

A similar evaluation of the shape of the constant delta-v contour lines to those performed for the zero revolutions transfer can be made analysing the solutions in departure and arrival times associated to tangential manoeuvre at departure or at arrival, represented in Fig.2.12 with the blue and green lines respectively, whose colour is scaled with respect to the eccentricity.

As expected and as before, the Hohmann transfer is identified at the intersection of the two curves associated to tangential manoeuvres. Instead, differently from the triangle-like shape generated from zero-revolutions trajectories, the orientations of all lobes are captured by each extremity of the splines associated to tangential firing. It is interesting to note that for the same delta-v level, the number of epochs associated to long transfer solutions is significantly higher compared to the one assigned to short transfers. However this effect is the result of the fact that the search space is parametrised as a function of the time. Moving far from the minimum delta-v solution, with the increase of the eccentricity, the difference between short and long transfer time of flight grows which means that for a linear scaling of the axis it's natural to observe the area associate to solution space associated to long transfer bigger than the short one. Nevertheless substituting the departure and arrival date with the true anomaly would re-

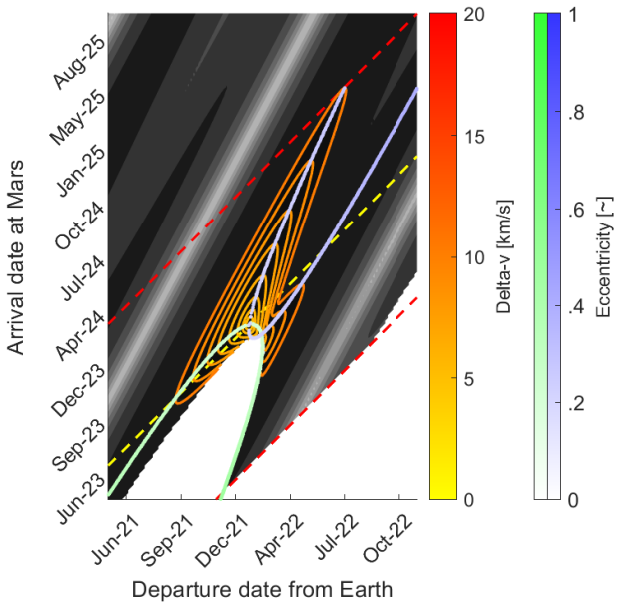

Figure 2.12: *The trend of the constant delta-v contour lines for the one revolution transfer over the solutions associated to tangential manoeuvres at departure or at arrival represented with in blue and green lines, respectively. The colour scaling is associated to the eccentricity of the transfer orbit. From below upwards, the red, yellow and red dashed lines display the solution associated to* 2, 3 *and* $4\Delta t_{HPO}$*. The area within the red lines represents the region of the search space in which the one-revolution transfer is expected to present lower delta-v compared to the zero- and two-revolutions one.*

solve the issue and make the two regions appears of the same size. A similar situation can be observed comparing the area subtended by zero and one-revolution contour lines obtained for the same delta-v. Despite the different shape, the difference in area is observable and can be explained by the fact the significant difference in time of flight. Indeed, for the same semi-major axis, zero and one-revolution transfers present the same delta-v nevertheless one-revolution solutions on a constant delta-v contour line display on average a time of flight 1.5 longer than zero-revolution one. If the contour lines were identical in shape, the one derived for one-revolution should occupy 1.5 more pixels than the zero-revolutions one, however given the different shape an estimate of the ratio of the two areas is pointless since the explanation of their different appearance is addressed.

Nevertheless the predominant elongation of the upper lobes of the domain with respect to the lower ones can be still associated to the fact that manoeuvres closer to the primary, and in that case at the departure, are more efficient and therefore requires less delta-v.

All these insights can be further investigated by representing the trajectories associated to a specific contour line, see Fig. 2.13. Two types of orbits can be identified: those found at the intersections between the lines associated to tangential manoeuvres

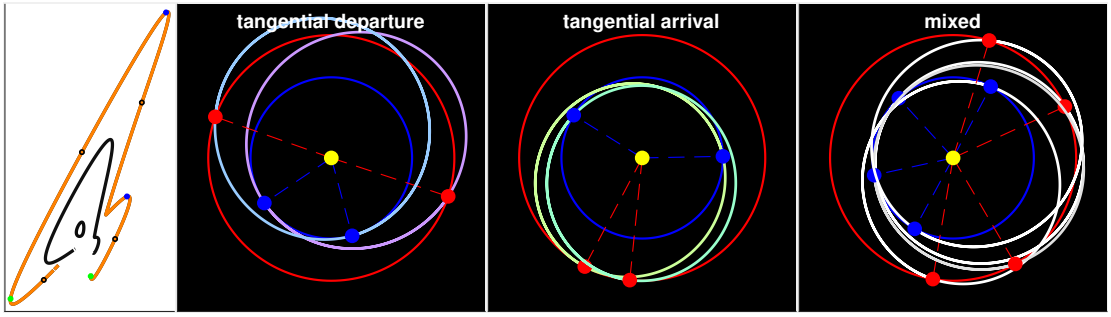

Figure 2.13: *The representation of one revolution trajectories associated to the* 10 *km/s delta-v contour line. In particular, cyan and purple are associated to long and short transfer with a tangential manoeuvre at the departure. Green and yellow for one at the departure while white orbits implement all secant tangential manoeuvres.*

and the reference constant delta-v contour line, and those obtained performing all secant firing. It can be observed that performing a tangential manoeuvre at the departure, which appears to be more efficient, leaves more delta-v to be spent at the arrival and therefore results in a steeper crossing between the transfer and the arrival orbit. On the other end, tangential firing at the arrival, less efficient with respect to the departure one, prevents from performing steep manoeuvre at departure, requiring a shallower angular difference between the departure orbit and the transfer.

In the end, all secant manoeuvres, captured in the "mixed" scenario, represent a transition phase between the two cases, similarly to zero revolutions transfer case, see Fig. 2.9. The relative small delta-v level prevents from appreciating significant differences between long and short transfer, which have been represented in Fig. 2.13 with cyan and purple colours for the departure case and with a green and yellow for the arrival one.

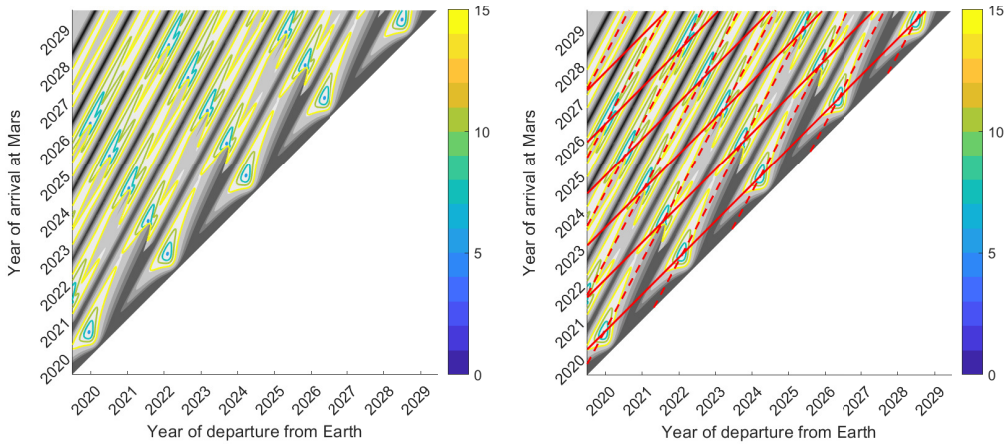

Figure 2.14: *On the right, the zero and multi-revolutions minimum delta-v contour line, up to the* 4^{th} *revolutions, represented in the porkchop plot. On the left, the identification of the delta-v minima at the intersection of* $n\Delta t_{HTO}$ *and* $\Delta\varphi_{\pi}$ *lines, represented with a continuous and broken dashes respectively.*

Such considerations enables to open new scenarios with respect to those identified for the zero revolutions case and to populate the porkchop plot of new minima, see Fig.2.14 whose center can be located with no need to resolve the associated Lambert's problem but exploiting the geometric relations.

CHAPTER 3

Search space reduction for flyby trajectories

In the design of MGA trajectories, the ”branch and bound” algorithm represents one of the most used methods to identify optimal transfers [22]. The underlying idea of the approach consists into breaking the trajectory of the S/C in several legs connecting each pair of planets for a predetermined sequence of flybys. The different targeting problems are resolved in cascade for distinct combination of departure and arrival dates. The optimal solution is finally identified as the one which permits to minimize the cost function while satisfying the constraints.

Such method requires a massive computational cost since the computational complexity grows exponentially. To reduce the dimensionality growth of the search space, in the first part of the chapter, a method based on the combinatorial evaluation of consecutive targeting problems is proposed. In particular, the arrival and departure relative velocities associated to consecutive legs are recombined at the common node for each date of flyby. The recombination allows to restore a quadratic growth for computational effort, similar to the case of direct transfers. In the second part of this chapter, a method inspired by shape-based algorithms, derived for low-thrust trajectories, is applied for the impulsive thrust case to reverse the Lambert problem by solving Kepler equation for the time-of-flight instead of the semi-major axis. This is possible since the search space is parametrised not anymore in epoch but in orbital elements which

appears to be a more compact set compared to its temporal counterpart. Moreover, the inverse Lambert problem allows an explicit resolution for the time of flight of the transfer without passing through any non-linear equation. Flybys connecting consecutive transfer legs are evaluated by approximated functions expressed in terms of the Keplerian elements.

3.1 Grid-search recombination for triplets

Switching from direct transfer solution of the simple targeting problem to flyby trajectories can be beneficial from the point of view of fuel/cost mission saving, new launch windows opportunities and a significant increase in scientific return.

The idea behind the flyby exploitation consists in leveraging the interaction with the gravitational pull of a secondary attractor in order to modify in a desired manner the trajectory of the S/C with respect to the primary body.

The conventional approach consists in treating each transfer leg independently by resolving separately the associated Lambert's problems and analysing the boundary conditions at the flyby planet. Patched conics models the effect of the close encounter with an instantaneous change in magnitude and direction of the heliocentric velocity [31, 51].

Therefore, each flyby can be evaluated depending on how the Lambert's solutions for two consecutive legs recombine at the flyby planet in terms of the difference in magnitude and orientation relative velocities compared to the one attainable by the close approach.

The relative velocities at the flyby planet, $\mathbf{v}_\infty^\pm$, which are computed as the difference of the heliocentric ones, $\mathbf{v}^\pm$, solutions of the targeting problems for the pre- and post-encounter trajectories, and the planetary heliocentric velocity, $\mathbf{v_{pl}}$:

$$\begin{aligned} \mathbf{v}_\infty^- &= \mathbf{v}^- - \mathbf{v_{pl}} \\ \mathbf{v}_\infty^+ &= \mathbf{v}^+ - \mathbf{v_{pl}} \end{aligned} \tag{3.1}$$

identify two hyperbolic trajectories in the SOI of the flyby planet. Their patching can be ensured by applying a correction manoeuvre at infinite [31] that covers the difference of the in-/out-coming relative velocities at the boundaries of the flyby planet:

$$\Delta v_\infty = \left| v_\infty^- - v_\infty^+ \right| \tag{3.2}$$

An additional cost must be paid when the flyby does not provide the necessary contri-

bution in terms of desired turning angle:

$$\Delta v_\infty = \sqrt{{v_\infty^+}^2 + {v_\infty^-}^2 - 2v_\infty^+ v_\infty^- cos(\delta - \delta_{\max})} \tag{3.3}$$

where δ is the desired turning angle computed as the angular distance measured between in-/outgoing infinite velocities and $\delta_{\max}$ represents the maximum turning angle that the flyby can offer when the closest approach is performed at the minimum allowed periaspidal distance, $r_{p_{\min}}$ [6, 27, 57]:

$$\delta_{\max} = max_{v_\infty^\pm} \left(2 \sin^{-1} \frac{1}{1 + \frac{r_{p_{\min}} v_\infty^2}{\mu}} \right) \tag{3.4}$$

From a design perspective, considering a flyby along the trajectory implies resolving one additional targeting problem per each flyby. A convectional grid-search algorithm for the design of flyby trajectories would perform the resolution of each Lambert leg in cascade, situation inducing the growth of the computational effort by an exponential factor. In fact, if the direct transfer case demands the evaluation of Eq. 3.4 for n epochs of departure over m epochs of arrival, the computational effort in the case of one flyby grows from quadratic, $n \times m$, to cubic ,$n \times m \times l$, where n, m and l are associated to the number of departure, flyby and arrival dates. This brute-force approach requires to re-evaluate multiple times the same targeting problem. A more elegant implementation would resolve the two Lambert's problem separately and recombine the solutions at the common node that share the same date of flyby. From now on two new terms are introduced namely doublets and triplets, that refer to a set of epochs for the simple and flyby targeting problem. In particular, doublets represent a set of departure and arrival dates, while triplets a set of departure, flyby and arrival dates.

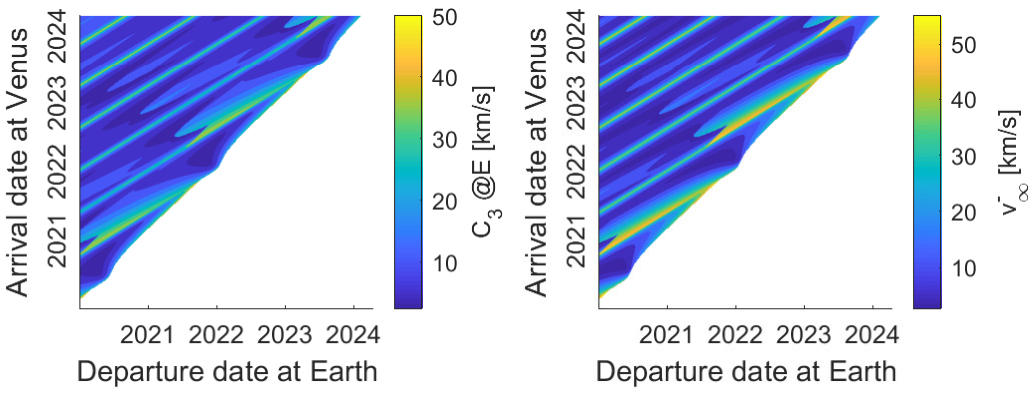

(a) C_3 *at departure from Earth*

(b) v_∞^- *at arrival at Venus*

Figure 3.1: *The porkchop plot in C_3 and v_∞ for the Earth-Venus leg.*

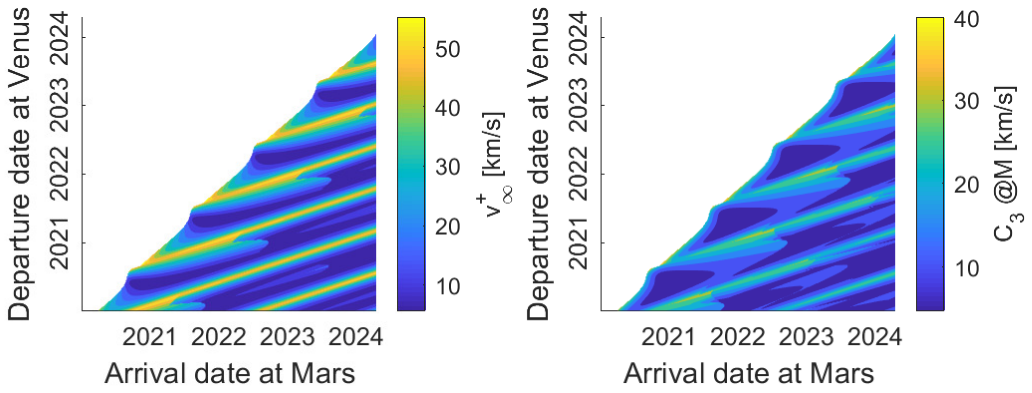

(a) v_∞^+ *at departure from Venus* **(b)** C_3 *at arrival at Mars*

Figure 3.2: *The porkchop plot in C_3 and v_∞ for the Venus-Mars leg.*

Fig 3.1 and Fig. 3.2 represents the relative velocity at departure and at arrival in a porkchop plot flavour for the an Earth-Venus and Venus-Mars transfers:
The recombination of the search space for two consecutive doublets at the same date of flyby enables to construct a slice of solution space of the triplets in the departure and arrival dates hyperplane on which it is possible to observe the total delta-v at the terminal points, see Fig. 3.3, the relative velocity difference at the flyby and the desired turning angle, see Fig. 3.4.

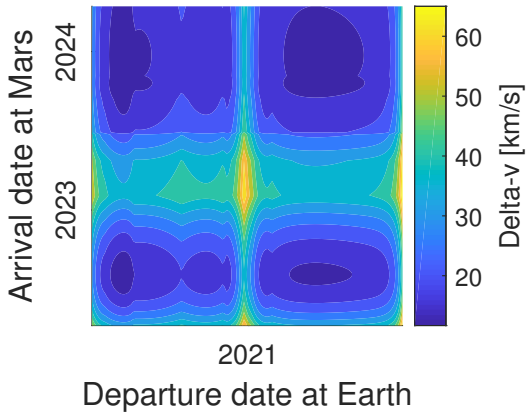

Figure 3.3: *The total delta-v at terminal points for an Earth-Mars trajectory with a flyby at Venus on the 1^{st} January 2022.*

Repeating the recombination for all the date of flyby allows to scan the complete search space of the triplets. The proposed grid-search algorithm allows to reduce the number of computation to $n \times m + m \times l = m \times (n + l)$ targeting problems restoring the quadratic growth for the computational effort from the cubic one observed in the classical cascade approach, .

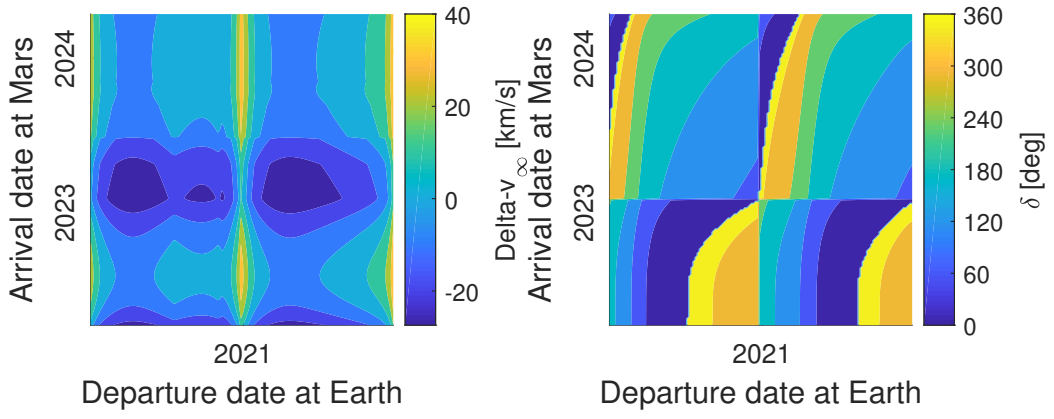

(a) v_∞ *difference* **(b)** *turning angle,* δ

Figure 3.4: *The infinite velocity difference and the turning angle for an Earth-Mars trajectory with flyby at Venus on the* 1^{st} *January 2022.*

3.2 Inverse Lambert problem

In the previous section a method to reduce the computational effort of the grid-search of triplets was presented. The presented approach for the design of flyby trajectories rejects the classical cascade approach employed for sequence of targeting problems, forcing a repetitive scanning of the same terminal conditions, and proposes, instead, a separate analysis of each Lambert leg on its specific time grid and a subsequent re-combination of solutions for common dates of flyby. Despite the improvement, the approach remains bounded to an epoch-based search. Thus, the exploration of the full solutions space results impractical [46], a fortiori, considering that patched conics solutions might vanish or experience unpredictable increase in delta-v when optimised in the full model. Therefore, in order to further reduce the search space, the epoch parametrisation is substituted with another one based on the Keplerian elements of the transfer orbit. Such approach is more efficient from different points of view:

- the orbital elements are slower varying parameters compared to Cartesian state vectors, meaning that fewer number of points need to be evaluated to obtain the same sampling on dates;
- the Keplerian formulation of the targeting problem enables an explicit resolution of the inverse Lambert problem.

Hence, instead of resolving the non-linear targeting problems associated to a given set of triplets and evaluate the solutions in terms of the total delta-v (sum of the components at the terminal points and at the flyby), the orbital parameters, associated to the pre- and post-encounter transfer orbits, are separately scanned and evaluated together

in terms of an approximated quality of the flyby trajectory expressed in the form of an equality constraint. The feasible solutions are converted back to triplets resolving for the time of flights, similarly to shape-based methods for low-thrust trajectories [52,54], and matching the date of flyby.

The degenerate flyby solution

An extreme case which offers an insight into the parametrisation of the triplets problem in Keplerian elements is the degenerate flyby, a transfer orbit obtained for the limiting case of the zero-effect flyby which could be considered as the one obtained for a flyby to a massless body, $\mu \to 0$, or for a close approach at an infinite flyby altitude, $r_p \to \infty$. The problem is formulated in the literature [6] as an orbit determination problem based on three observations performed at different times. In this particular case, the observations coincide with the ephemerides of three arbitrary planets whose evolution in the simple case of circular coplanar orbits is given as follows:

$$L_i = \sqrt{\frac{\mu}{{r_i}^3}} t_i + \varphi_i\left(t_0\right) \qquad \text{with} \qquad t_i = \sum_{j=1}^{i-1} t_j \qquad \text{for } i = 1,2,3 \tag{3.5}$$

where L_i represents at the same time the true anomaly of i^{th} planet and the true longitude of the degenerate transfer orbit at the t_i instant. Considering the introduction of the true longitude by Eq. 3.5 to characterise the position along the transfer orbit, it is convenient to switch from an orbital parameters treatment of trajectory into an equinoctial ones, that for circular coplanar orbits are reduced to the semilatus rectum, p, and the components of the eccentricity vector, k and h defined as:

$$p = a(1-e^2) \quad k = e\cos\varpi \quad h = e\sin\varpi \quad \text{with} \quad \varpi = \cancel{\Omega} + \omega$$

where ϖ constitutes the longitude of the periapsis that in the coplanar case equals the argument of the periapsis. Then the condition of belonging to the same orbit can be stated as a system of three equations in three variables that imposes that the linearised orbit equation [6] is satisfied for each observation, as follows:

$$\frac{p}{r_i} - k\cos L_i - h\sin L_i = 1 \tag{3.6}$$

By applying the Cramer's rule and classical trigonometry identities [6], it can be shown that the equinoctial elements can be derived as a function of the orbital radii of the planets, r_1, r_2 and r_3, and true longitudes, L_1, L_2 and L_3, of the three observations

performed at the departure, flyby and arrival times, t_1, t_2 and t_3 respectively:

$$\begin{cases} p = \frac{r_1 r_2 r_3 (\sin L_2 - L_1 + \sin L_1 - L_3 + \sin L_3 - L_2)}{r_1 r_2 \sin L_2 - L_1 + r_1 r_3 \sin L_1 - L_3 + r_2 r_3 \sin L_3 - L_2} \\ k = \frac{r_1 (r_2 - r_3) \sin L_1 + r_2 (r_3 - r_1) \sin L_2 + r_3 (r_1 - r_2) \sin L_3}{r_1 r_2 \sin L_2 - L_1 + r_1 r_3 \sin L_1 - L_3 + r_2 r_3 \sin L_3 - L_2} \\ h = \frac{r_1 (r_3 - r_2) \cos L_1 + r_2 (r_1 - r_3) \cos L_2 + r_3 (r_2 - r_1) \cos L_3}{r_1 r_2 \sin L_2 - L_1 + r_1 r_3 \sin L_1 - L_3 + r_2 r_3 \sin L_3 - L_2} \end{cases} \tag{3.7}$$

The space triangles associated to the pre- and post-encounter trajectories, which in the case of the degenerate flyby are the same orbit, are fully defined by the differences in true longitudes, ΔL, and the semi-major axis, a. Therefore, the time of flights, Δt_{12} and Δt_{23}, can be explicitly derived from Eq. 2.1 since the eccentric anomalies, α and β, are unambiguously defined as a function of the equinoctial elements and the true longitude pairs, $\{L_1, L_2\}$ and $\{L_2, L_3\}$, [4].

The departure, flyby and arrival epochs can be extracted by the solution space where the FTC derived for the short transfer arc is verified:

$$\text{FTC} : \begin{cases} \cos\left(n_2 \Delta t_{12} + \varphi_{12}\left(t_1\right)\right) - \cos\left(L_2\left(t_2\right) - L_1\left(t_1\right)\right) \\ \cos\left(n_3 \Delta t_{23} + \varphi_{23}\left(t_2\right)\right) - \cos\left(L_3\left(t_3\right) - L_2\left(t_2\right)\right) \end{cases} \rightarrow 0$$
$$\text{subject to} \quad \begin{array}{l} \sin\left(n_2 \Delta t_{12} + \varphi_{12}\left(t_1\right)\right) > 0 \\ \sin\left(n_3 \Delta t_{23} + \varphi_{23}\left(t_2\right)\right) > 0 \end{array} \tag{3.8}$$

Long transfer solutions can be evaluated solving the FTC with respect to the long time of flight, obtained as difference between the orbital period and the short time of flight, and changing the sign to the inequality constraints in Eq. 3.8.

Eccentricity parametrisation of sub-optimal triplets search space

A feasible flyby (with a non-zero effect) requires to evaluate two separate orbits to describe the pre- and post-encounter transfers. Their difference in Keplerian elements can be related to a finite close encounter, differently from the degenerate flyby that can be considered as a case limit for an altitude of the close approach tending to infinity.

In order to reduce the number of variables under study without sacrificing the optimality of the solution space, the hypothesis of tangential thrust at the terminal points, departure and arrival, is introduced.
In the degenerate flyby, the orbital elements of the transfer were obtained directly as a function of the planets true anomalies. The epochs of conjunction, coinciding with departure, flyby and arrival dates, were derived where the equation of times of flight. In this case, conversely, it is necessary to choose an orbital element to parametrise each leg. The tangentiality constraint for the delta-v at the terminal points identifies explic-

itly the true anomalies of conjuction and enables to derive the departure and arrival dates that solve the FTC for the time of flight. A similar approach was used in the literature for shape-based algorithm applied to low-thrust trajectories [52, 54] and before for the case of the degenerate flyby. The eccentricity represents the best choice for the shaping parameter, since, unlike the semi-major axis, it is bounded. The eccentricities and the initial/final dates for each leg determine unambiguosly the two trajectories. In fact, the semi-major axes of the transfers can be easily derived as a function of eccentricity and orbital radii of departure and arrival planets, r_1 and r_3. Instead, the arguments of the periapsis for the pre-/post-encounter transfers are directly connected to the departure/arrival dates, t_1 and t_3, by the true anomalies, f_1 and f_3:

$$\begin{aligned} &1: \quad a_1(e_1) = \tfrac{r_1}{1-e_1} \qquad \omega_1(t_1) = f_1(t_1) \\ &2: \quad a_2(e_2) = \tfrac{r_3}{1+e_2} \qquad \omega_2(t_3) = f_3(t_3) - \pi \end{aligned} \tag{3.9}$$

In Eq. 3.9, the absence/presence of π in the definition of the arguments of the periapsis defines whether the departure and arrival conditions are periapses or apoapses. In the end, the departure/arrival can be derived from the FTC resolving for the time of flight, by replacing the semi-major axis and the true anomalies difference for each leg, accounting for the aperture of the space triangle, with the eccentricity relations derived in Eq. 3.9 and Eq. 3.10 in the case of the short transfers:

$$\begin{aligned} &\text{FTC:} \quad \begin{cases} \cos\left(n_2\Delta t_{12} + \Delta\varphi_{12}(t_1)\right) - \cos\left(\Delta f_{12}\right) \\ \cos\left(n_3\Delta t_{23} + \varphi_{23}\left(t_2^+\right)\right) - \cos\left(\Delta f_{23}\right) \end{cases} \rightarrow 0 \\ &\text{s.t.} \quad \begin{aligned} \cos\left(\Delta f_{12}(e_1)\right) = +\cos f_2^- &= \tfrac{1}{e_1}\left(\tfrac{r_1}{r_2}(1+e_1) - 1\right) \\ \sin\left(n_2\Delta t_{12} + \Delta\varphi_{12}(t_1)\right) &> 0 \\ \cos\left(\Delta f_{23}(e_2)\right) = -\cos f_2^+ &= \tfrac{1}{e_2}\left(1 - \tfrac{r_3}{r_2}(1-e_2)\right) \\ \sin\left(n_3\Delta t_{23} + \Delta\varphi_{23}\left(t_2^+\right)\right) &> 0 \end{aligned} \\ &\text{where} \quad \begin{aligned} t_2^- &= t_1 + \Delta t_{12} \\ t_3^- &= t_2^+ + \Delta t_{23} \end{aligned} \end{aligned} \tag{3.10}$$

Eq. 3.10 identifies the initial dates, t_i, for the pre- and post-encounter transfers, t_1 and t_2^+ respectively, that satisfy the FTC while imposing that the aperture of the space triangle, Δf, equals the difference in initial phasing of the planets for each targeting problem. $\Delta\varphi(t_i)$, considers the angular distance covered by the final planet rotating at speed n_f for the time of flight of the transfers. Similarly to the degenerate flyby case, long transfers can be considered by changing the sign of the inequality in Eq. 3.10 and

substituting the time of flight with its complementary for the short transfer with respect to the orbital period. It can be noted that in Eq. 3.10 the condition of existence of the cosine for the aperture of the space triangle, or for the true anomaly difference, imposes that the right term is bounded to ± 1 which in turn limit the eccentricity to the minimum and maximum values admissible for a transfer leg between the initial and final planet. For the pre-encounter orbit, the eccentricity ranges are derived by Eq. 3.11:

$$\frac{1}{e_1}\left(\frac{r_1}{r_2}(1+e_1)-1\right)\begin{cases} \leq \quad 1 \rightarrow e_{\min} = \frac{r_2-r_1}{r_2+r_1} \\ \geq -1 \rightarrow e_{\max} = 1 \end{cases} \tag{3.11}$$

where the minimum eccentricity equals exactly to the Hohmann transfer between the initial and arrival planets with orbital radii, r_1 and r_2 respectively. A similar expression can be obtained for post-encounter orbit.

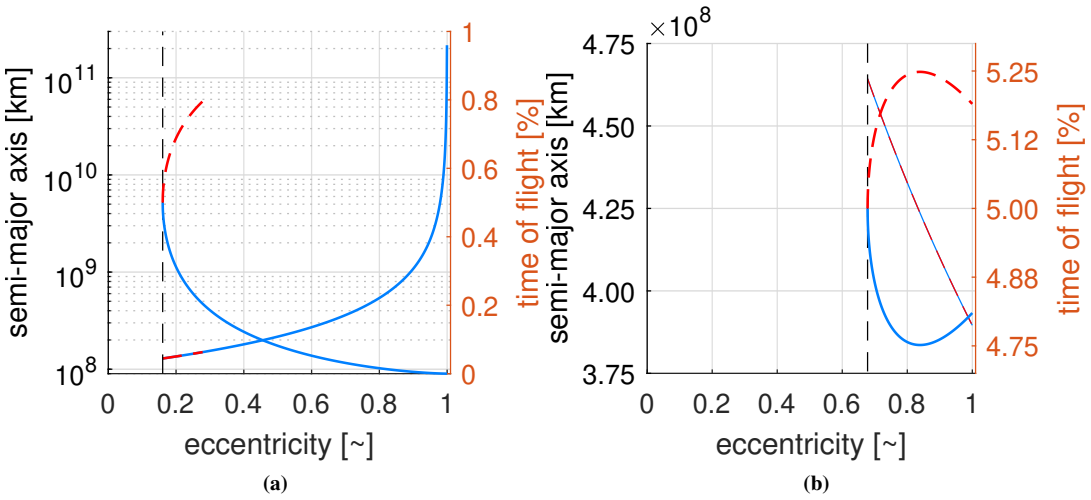

Figure 3.5: *The dependency of the semi-major axis and the associated time of flight on the eccentricity for the Venus-Earth (a) and Earth-Jupiter (b) legs tangential at the terminal points of the overall trajectory, i.e. the departure and arrival conditions from Venus and at Jupiter respectively. In a blue solid and red broken lines, the solution for the short and long transfers, limited in time of flight to one Hohmann period.*

Fig. 3.5 displays the trend of the semi-major axes for the short and long transfer solutions, in blue and red respectively, as a function of eccentricity.

A Venus-Jupiter trajectory with a flyby at Earth is considered as test case. The sub-optimality condition imposes the pre- and post-encounter transfers to be tangent at the departure and arrival orbits, condition that locates the pre-encounter periapsis and the post-encounter apoapsis on the orbit of Venus and Jupiter, respectively. It can be observed that the tangentiality constraint at the terminal points have two different effects on the time of flight: in the Venus-Earth leg the time of flight of the long transfer grows unbounded and it is limited at the value of the one Homann period, condition that allows

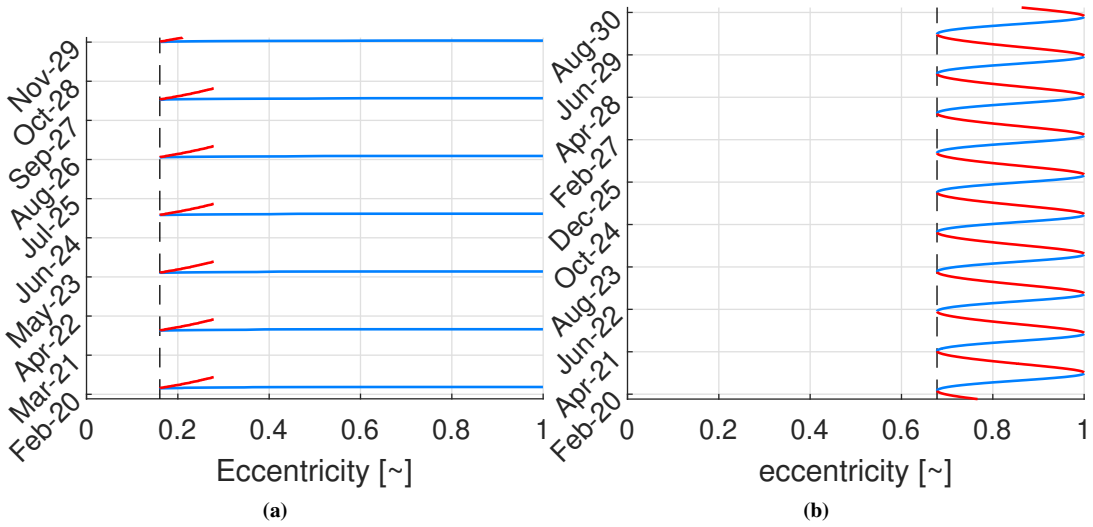

Figure 3.6: *The solution of the FTC in terms of the initial date of departure for the Venus (a) and of escape from Earth (b) correlated to eccentricity of the pre- and post-encounter legs tangential at the terminal points of the overall trajectory. In a blue solid and red broken lines, the solution for the short and long transfers, limited in time of flight to one Hohmann period.*

not to consider one-revolution transfers, on the other hand the Earth-Jupiter leg appears automatically bounded by the eccentricity ranges and the tangentiality condition at the arrival, see Fig. 3.5:

The FTC, see Eq. 3.10, allows to pass from a phase-free trajectory [42] to a solution coherent with the temporal evolution of the initial and arrival planets. Fig. 3.6 shows the solution of the FTC for the initial time, t_1 and t_2^+ associated to the dates of departure at Venus and escape from Earth, correlating the shaping parameters, e_1 and e_2, for the pre- and post-encounter transfers:

The final dates, t_2^- and t_3, associated to the arrival at Venus and Jupiter for the pre- and post-encounter transfers, respectively, can be computed from the initial dates adding the the time of flight, see Eq. 3.10. Fig. 3.7 displays in a porkchop plot the tangential solutions at the departure from Venus and arrival at Jupiter for the short and long transfer, in blue and red respectively:

Although, the two legs are fully defined, they are still not connected, task that is addressed by two equality constraints ensuring that the solutions reconnect at the flyby in terms of encounter date and effect of the close passage, which is evaluated by an approximating function in orbital parameters. A first possibility to link the pre- and post-encounter trajectories is represented by the Tisserand parameter, T, which approximates the orbital energy of a trajectory, see Eq. 3.12. Under the assumption of being evaluated outside the SOI of the secondary, the Tisserand parameter remains reasonably constant during a close approach as a result of its close connection with the

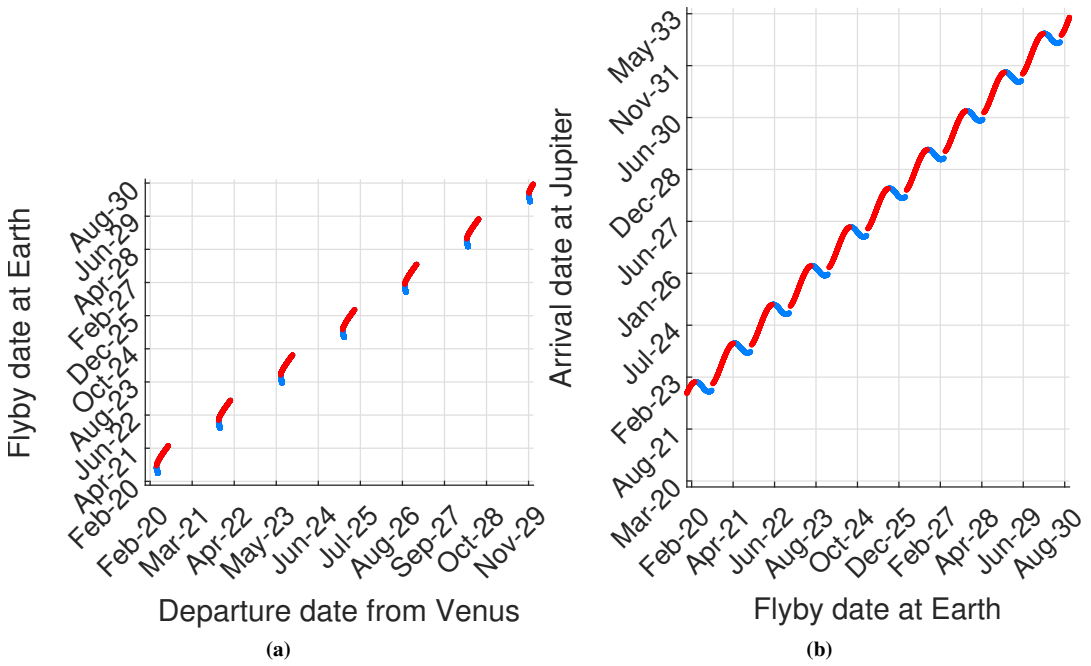

Figure 3.7: *The pork-chop plot representation for the Venus-Earth (a) and Earth-Jupiter (b) legs tangential at the terminal points of the overall trajectory, i.e. the departure and arrival conditions from Venus and at Jupiter respectively. In a blue solid and red broken lines, the solution for the short and long transfers, limited in time of flight to one Hohmann period.*

energy which constitutes the unique invariance of the three-body dynamics. Such characteristic make the Tisserand parameter suitable to evaluate the quality of the flyby. A relation in the orbital parameters can be expressed in the variational formalism 3.12:

$$T = \frac{1}{a} + 2\sqrt{a\left(1-e^2\right)} \quad \rightarrow \quad \Delta T = \Delta\frac{1}{a} + 2\Delta\sqrt{p} = 0 \tag{3.12}$$

where a and p are the non-dimensional semi-major axis and semlatus rectum. Eq. 3.12 imposes the ballistic condition which is verified when the pre- and post-encounter transfers are at the same orbital energy or in a patched conics perspective when the inbound and outgoing infinite velocities are equal, which translates into enforcing Eq. 3.2 to be exactly zero. This condition, however, represents only one side of the coin, in fact although the ballistic condition is satisfied the turning angle is completely overlooked and no conditions ensures that the desired value does not exceed the maximum admissible.

3.3 Gauss' variational equation for flybys

A different way to evaluate the quality of the flyby from ballistic condition expressed as the Tisserand parameter variation, just presented, can be formulated translating the

minimum close approach distance condition into orbital elements. This approach can be performed applying Gauss' variational equations [6] to the flyby problem. The following equation

$$\begin{aligned} \frac{da}{dt} &= \frac{2a^2}{h}\left(e\sin f a_r + \frac{p}{r}a_\theta\right) \\ \frac{de}{dt} &= \frac{r}{h}\left\{\frac{p}{r}\sin f a_r + \left[\left(1+\frac{p}{r}\right)\cos f + e\right]a_\theta\right\} \\ \frac{d\omega}{dt} &= \frac{r}{he}\left[-\frac{p}{r}\cos f a_r + \left(1+\frac{p}{r}\right)\cos f a_\theta\right) \end{aligned} \tag{3.13}$$

describes the orbital elements variation, here limited to the coplanar case, under the effect of the disturbing acceleration of the close approach, expressed in radial and ortho-normal components, a_r and a_θ, induced by the incoming transfer orbit defined with respect to the primary where h represents the angular momentum and f the true anomaly at which the transfer orbit crosses the circular orbit of radius r of the flyby planet.

Considering that the time of flight of a flyby occurs in an infinitesimal fraction of the S/C trajectory, then the acceleration can be exchanged with the velocity difference. Similarly, the time derivative of the orbital elements can be regarded as the finite variation at the infinitesimale time dt. Under this assumption, the heliocentric velocity variation measured at the boundaries of the SOI can be chosen to model the disturbing acceleration inducing the orbital element variations. The strategy ensures the applicability of the perturbation approach, described by Eq. 3.13, to the specific problem of the flyby.

In the hodograph representation [6], the relative velocity at the close encounter can be rewritten from the heliocentric one

$$\frac{h\mathbf{v}}{\mu} = e\sin f\,\mathbf{i}_r + (1+e\cos f)\,\mathbf{i}_\theta \tag{3.14}$$

in radial and ortho-normal components as a function of the orbital parameters:

$$\mathbf{v}_\infty = \frac{\mu}{h}\left(e\sin f\,\mathbf{i_r} + \left(1+e\cos f - \sqrt{\frac{p}{r}}\right)\mathbf{i}_\theta\right) \tag{3.15}$$

Eq.3.15 allows to write the pre- and post-encounter heliocentric velocity as a function of the components of the relative velocity, v_r^- and v_θ^-, the entry angle at infinite, α^- and the turning angle at the flyby, δ, see Eq.3.16:

$$\begin{aligned} \mathbf{v}^- &= \mathbf{v}_\infty\left(\sin\alpha^-\mathbf{i_r} + \cos\alpha^-\mathbf{i}_\theta\right) + \mathbf{v_{pl}}\mathbf{i}_\theta \\ \mathbf{v}^+ &= \mathbf{v}_\infty\left(\sin\left(\alpha^- \pm \delta\right)\mathbf{i_r} + \cos\left(\alpha^- \pm \delta\right)\mathbf{i}_\theta\right) + \mathbf{v_{pl}}\mathbf{i}_\theta \end{aligned} \tag{3.16}$$

where α is the incoming/outgoing flight path angle, or pump angle which is deemed

as the entry/exit angle described by the relative velocity at the entry condition with the SOI, v_{pl}, and δ is the turning angle with the sign, $\mp$, accounting whether the flyby is prograde or retrograde, indicated respectively with type I and type II.
Substituting the variations in radial and ortho-normal components:

$$\begin{aligned} \delta v_r &= v_\infty \left(\sin\alpha^+ - \sin\alpha^-\right) \\ \delta v_\theta &= v_\infty \left(\cos\alpha^+ - \cos\alpha^-\right) \end{aligned} \tag{3.17}$$

and differentiating with respect to the outgoing pump angle, α^+, the value related to the maximum variation induced on the orbital elements by the flyby can be identified by setting to zero the associated derivative. It is interesting to note that the maximum variation appears to be function of the eccentricity, e, and the true anomaly, f alone, as reported below:

$$\begin{aligned} \alpha^+_{\Delta a_{\max}} &= \arctan\left(\tfrac{e\sin f}{1+e\cos f}\right) \\ \alpha^+_{\Delta e_{\max}} &= \arctan\left(\tfrac{(1+e\cos f)\sin f}{(2+e\cos f)\cos f+e}\right) \\ \alpha^+_{\Delta \omega_{\max}} &= \arctan\left(-\tfrac{(1+e\cos f)\cos f}{(2+e\cos f)\sin f}\right) \end{aligned} \tag{3.18}$$

Their counterparts, i.e. the minimum variation of each Keplerian element, can be intuitively obtained at π radiants difference from the pump angle associated to the maximum variation:

$$\alpha^-_{\Delta a_{\min}} = \alpha^+_{\Delta a_{\max}} + \pi \tag{3.19}$$

and similarly for the eccentricity, e, and the argument of the periapsis, ω.

Feasible values of the outgoing pump angle, α^+, are those that satisfy the limits identified by the maximum and minimum turning angles, as defined followingly:

$$\{\alpha^+_{\mathrm{I/II}} | \quad \delta_{\min} < \mp\Delta\alpha \leq \delta_{\max}\} \tag{3.20}$$

obtained for an encounter at the SOI, associated to $\delta_{\min} \approx 0$, and at the minimum periapsis, assigned to $\delta_{\max}$, see Eq. 3.21:

$$\begin{aligned} \delta_{\min} &= \left(1 + \tfrac{v_\infty^2 a_{pl}}{\mu_{pl}^{4/5}\mu^{1/5}}\right)^{-1} \approx 0 \\ \delta_{\max} &= \left(1 + \tfrac{v_\infty^2 r_{pl}}{\mu_{pl}}\right)^{-1} \end{aligned} \tag{3.21}$$

Re-substituting the filtered values in Gauss Planetary Equations, see Eq.3.20, allows to obtain the maximum and minimum range for the semi-major axis, eccentricity and argument of the periapsis of the post-encounter orbit, see Eq. 3.22:

$$\begin{aligned} a_1 + \Delta a_{\min} \leq a_2 \geq a_1 + \Delta a_{\max} \\ e_1 + \Delta e_{\min} \leq e_2 \geq e_1 + \Delta e_{\max} \\ \omega_1 + \Delta \omega_{\min} \leq \omega_2 \geq \omega_1 + \Delta \omega_{\max} \end{aligned} \tag{3.22}$$

CHAPTER 4

Search space pruning for flyby trajectories

The design of MGA trajectories is a complex problem that is generally solved in cascade at the risk of an explosion of the dimensionality caused by the pursuit of high resolutions that induces a fine discretisation of the grid.

In Ch. 3, we presented two methods to reduce the computational complexity of the solution space of flyby trajectories based on one side on the recombination of the search spaces associated to the doublets sharing the same node, and on the other on a reformulation of the targeting problem that permits to parametrise its search space on the orbital elements, more compact compared the epoch-based one.

A different way to achieve fast preliminary design of flyby trajectories can be obtained by reducing the dimensionality growth through the removal of those solutions that violates certain parameters, such as the time of flight [7], delta-v [35], the infinite velocity [3], the semi-major axis or other orbit-related quantities [22]. These methods are generally called pruning [9] and consist on a coarse sampling of the search space to evaluate the behaviour of the subset with respect to certain performance indices whose bounding allows to reduce the original search space into a domain of interest [22]. The conventional treatment of MGA trajectories as sequence of different targeting problems popularised a fragmented vision of the solution space into as many subsets as doublets. Incremental pruning aims to the consecutive pruning of each subset in order

to reduce the overall search space.

In the literature, pruning and in particular thrust constraints have been applied mainly to evolutionary algorithms, such as differential evolution [7,35], particle swarm optimisation [35], ant colony [22] and differential algebra [3], given their ability to reproduce in the population a representation of the complete solution space. However, incremental pruning represents an interesting option to be explored for standard grid-search algorithm. However, performing sampling even only on the doublets subsets of the search space can be twofold problematic: on one side it is not trivial identifying the proper mesh, not too loose and not too fine, for the specific targeting problem, and on the other a mesh that works for one doublets might not work for another and requires some tuning.

The idea proposed in this work follows from the insights derived from the analysis of the porkchop plot and the grid reduction. In fact from the shape analysis of constant delta-v contours, a closed region can be derived and used to effectively bound the grid search to initial conditions within a predefined delta-v. A simple root-finding approach is implemented to refine the bounding region on the actual contour line. This step is necessary not only to shrink the constraints, but also to pass from an initial guess obtained in the circular coplanar dynamics to the delta-v contour computed in the real ephemerides model. Finally, for the flyby a different approach is presented which relies on combining the shape pruning to the variational gravitational equations developed for the flyby in Ch. 3 to further reduce the search space of the post-encounter leg.

4.1 Pruning approach for targeting problem

In Ch. 2, it has been shown how tangential manoeuvres can be used to characterise the shape of constant delta-v contours as they give an indication for the orientation of the lobes of the porkchop plot. In Ch. 3, instead, tangential delta-v at the terminal points of the trajectory allows reducing the targeting problem into an explicit expression for the time of flight as a function of the eccentricity only. The epochs associated to the event are identified by the FTC, in Eq. 3.10, where the phasing between departure and arrival planets is related to the time of flight.

In this work the knowledge acquired so far will be applied to prune the search space for direct trajectories.

4.1.1 Generation of a bounding region from tangential solutions

To derive the delta-v associated to arcs with a tangential manoeuvre at departure/arrival, the value of the true anomaly for the secant manoeuvre at arrival/departure, $f_{a/d}$, can be computed from Eq. 3.10, recalling that $\cos\Delta f = \pm\cos f_{a/d}$ which results in Eq. 4.1:

$$f_{a/d} = \tan^{-1}\left(\text{sign}\left(\sin\left(n_a \Delta t + \varphi(t_d)\right)\right)\sqrt{(1-\cos^2(\Delta f))}, \pm\cos(\Delta f)\right) \tag{4.1}$$

The delta-v for transfer leg with a tangential manoeuvre at departure/arrival can be computed as the sum of the norm of the relative velocities at the terminal points derived on the hodograph plane, see Eq. 3.15 as in Eq. 4.2:

$$\Delta v = \left|\sqrt{\mu\frac{1\pm e}{r_{d/a}}} - \sqrt{\frac{\mu}{r_{d/a}}}\right| + \sqrt{\frac{3\mu}{r_{a/d}} - \mu\frac{1\mp e}{r_{d/a}} - 2\mu\sqrt{\frac{1\pm e}{{r_{a/d}}^3}r_{d/a}}} \tag{4.2}$$

The first and last term of Eq. 4.2 are associated respectively to the tangential and secant contributions. Eq. 4.2 evaluated at the minimum eccentricity of the transfer returns as expected the delta-v of the HTO, as in Eq. 4.3:

$$\Delta v = \left(\sqrt{\frac{r_a}{r_d}\frac{2\mu}{r_a+r_d}} - \sqrt{\frac{\mu}{r_d}}\right) + \left(\sqrt{\frac{\mu}{r_a}} - \sqrt{\frac{r_d}{r_a}\frac{2\mu}{r_a+r_d}}\right) \tag{4.3}$$

It is worth mentioning that, despite the true anomaly of the secant crossing takes into account the different types of transfer, short or long, through the sign in Eq. 4.1, the delta-v does not. This behaviour derives from the symmetry of the orbit with respect to the apse line. As shown by Eq. 3.14 and Eq. 3.15, complementary solutions in time of flight with respect to orbital period, or similarly in true anomaly, present opposite and equal trend for the radial and ortho-normal components of the velocity, respectively. From the point of view of the delta-v, instead, the two manoeuvres are equivalent since the change of sign is not lost during the normalisation.

Such behaviour explains also the different sizes of the constant delta-v contours for multi-revolution trajectories, see Fig. 2.12, with the area associated to long transfers much bigger than the short ones. The different dimensions in fact can be directly related to the times of flight.

Given the analytical expression of the delta-v for the solutions with a tangential manoeuvre, see Eq. 4.2, it is possible to identify the intersection points for the tangential solutions with a given constant delta-v contour line, without having to compute the targeting problems for the search space of the doublets from which the contour is interpolated. Instead, a bounding region can be derived from the tangential solutions, constituting the vertices of a box ordered to create a compact boundary,as shown in Fig. 4.1 with the red dashed line.

Although the bounding region based on tangential solutions does not capture in detail the topology of the constant delta-v contour, it offers a first guess of the region

around the minima exhibiting lower delta-v compared to the reference one. Nevertheless, the advantages behind the capability to predict this area a-priori can be significant as it allows to:

- discard directly initial conditions for departure and arrival epochs that would require higher delta-v avoiding to compute them;
- specify a fine grid size within the region of interest, without incurring into the dimensionality curse.

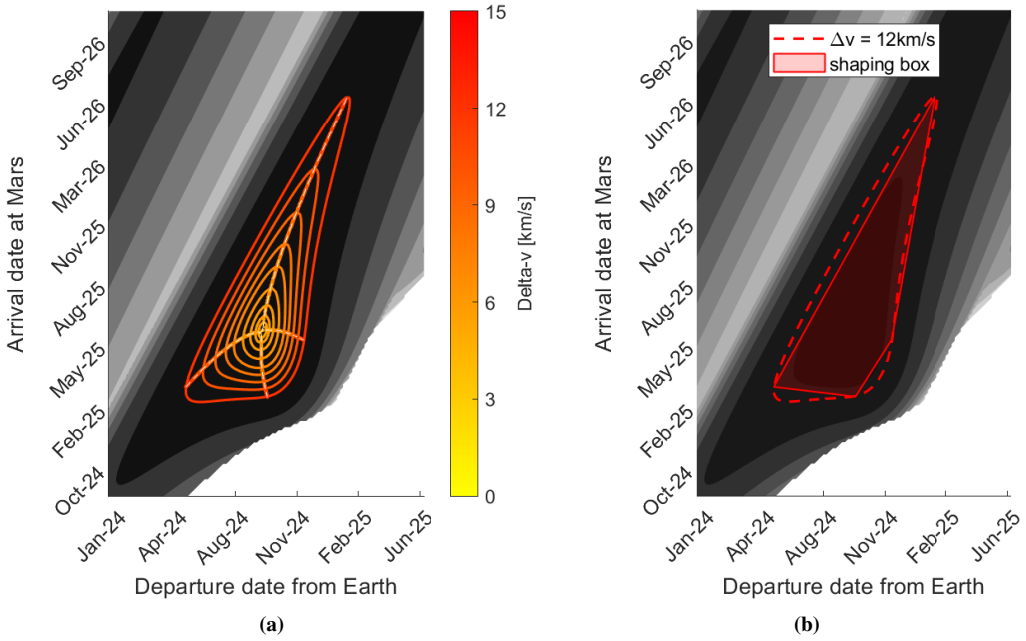

Figure 4.1: *The generation of the bounding region (b) from the 12 km/s delta-v solutions associated to tangential manoeuvres either at departure or at the arrival (a).*

The pruning method based on tangential solutions can raise concerns regarding the different space occupancy of the bounding region compared to actual constant delta-v contour line which is the result of the different shapes. This situation can only worsen considering the application of the bounding region to real ephemerides for which the constant delta-v contour line can differ significantly from the generating one derived for circular coplanar dynamics.

A justification on the last point can be found in the fact that although circular coplanar orbits for the departure and arrival planets represent the best case scenario from a delta-v point of view. In a pruning perspective the control region derived is larger compared to one derived for the real ephemerides case. This should prevent the approach from missing large portions of the region of interest associated to feasible trajectories

within the prescribed delta-v requirement. A straightforward solution for the space occupancy could be obtained by increasing the reference delta-v in order to expand the associated contour line and in turn the bounding region. Nevertheless, the delta-v increment is based on pure heuristics and should be established on an trade-off logic. The objective, in fact, remains that to identify the optimal occupancy configuration that entails the minimum loss of feasible initial conditions with the lowest inclusion of unfeasible ones.

4.1.2 Refinement of the bounding region

In the previous paragraphs, a method for pruning the search space was presented. It consists on the generation of a bounding region at the intersection of the solutions associated to tangential manoeuvres with a reference unknown, since not already computed, constant delta-v contour. The technique is innovative as it allows to achieve a-priori characterisation of the region with a delta-v less than the chosen reference value and to subsequently grid it according to the user needs. However, it requires some practical criterion to overcome the region occupancy difference between the bounding region and the actual contour. Achieving this capability, however, is not a trivial matter.

Instead, as shown in Algorithm 1, a root finding subroutine allows to modify the shape of the bounding region and adapt it to the one of the constant delta-v contour. Its logic consists in optimising the position, in departure and arrival dates, of the midpoints generated by consecutive pairs of vertices of the original bounding region, $\{t_d, t_a\}$, in order to make them shift on the contour line identified by the reference delta-v, Δv_{ref}, maintaining an equal distance from the associated vertices. The process continues until the difference in area between the old and new bounding regions, A_0 and A, does not satisfy the selected relative tolerance.

Algorithm 1 Midpoints generation for constant delta-v refinement.

Require: $\mathbf{t}_d$, $\mathbf{t}_a$, Δv_{ref}, RelTol, $A_0 = 0$, A
  while $|A_0/A - 1| \geq$ RelTol **do**
    Initialise ${\mathbf{t}_{d/a}}^0$ to the vectorised $\mathbf{t}_{d/a}$
    Initialise $\mathbf{t}_{d/a}$ to a matrix of consecutive pairs ${\mathbf{t}_{d/a}}^0(i), \forall i = \{1,2\}, \ldots, \{N,1\}$
    for $j = 1, 2, \ldots, N$ **do**
      find ${t_{d/a}}^{(k)}$
        ${t_{d/a}}^{(0)} \leftarrow \overline{\mathbf{t}_{d/a}(i(j))}$, midpoint of the j pair
        s.t.
          the delta-v of the targeting problem $\mathbf{t}^{(k)}$, $\Delta v\big(\mathbf{t}^{(k)}\big) \rightarrow \Delta v_{\text{ref}}$
          the distance difference from the j pair, $\Delta\big\|\mathbf{t}^{(k)} - \mathbf{t}(i(j))\big\| \rightarrow 0$
      $\mathbf{t}_{d/a}(j,2) \leftarrow {t_{d/a}}^{(k)}$
    end for
    $A_0 \leftarrow A$
    $A \leftarrow \sum_i \overline{\mathbf{t}_a(i)} \Delta \mathbf{t}_d(i), \forall i = \{1,2\}, \ldots, \{2N,1\}$
  end while

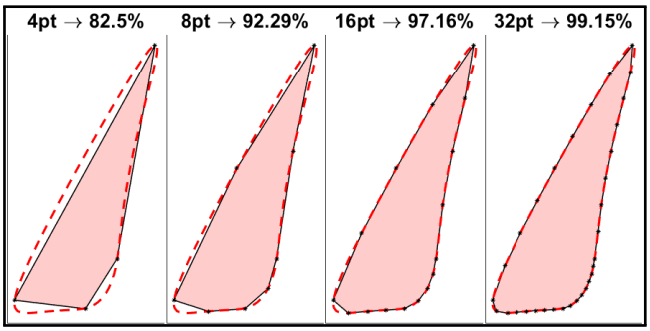

Figure 4.2: *Three iterations of the refinement process of a bounding region generated from a 12 km/s constant delta-v contour.*

Fig. 4.2 shows the number of points for which the bounding region is identified and the associated space occupancy which is computed as the ratio between the area of the bounding region and the one of the exact constant delta-v contour. In just three steps the bounding region can be refined to less than 1% difference from the actual delta-v contour. The refinement process is inexpensive from a computational point of view as it reaches convergence on average in less than three iterations.

In the end, the refinement is the solution to achieve the capability of pruning the search space of transfer orbits targeting real ephemerides. An additional root-finding algorithm is considered to bring the initial guesses derived on the circular coplanar dynamics to real ephemerides, see Algorithm 2

Algorithm 2 Tangential solution refinement on real ephemerides.

Require: $\mathbf{t}_d$, $\mathbf{t}_a$, Δv_{ref}
  for $j = 1, 2, \ldots, N$ with $N = 4$ **do**
    find ${t_{d/a}}^{(k)}$
      ${t_{d/a}}^{(0)} \leftarrow \mathbf{t}_{d/a}(j)$
      s.t.
        the delta-v of the targeting problem $\mathbf{t}^{(k)}$, $\Delta v\big(\mathbf{t}^{(k)}\big) \rightarrow \Delta v_{\text{ref}}$
        the tangential condition holds at d or a, $\mathbf{r}({t_{d/a}}^{(k)}) \cdot \mathbf{v}({t_{d/a}}^{(k)}) \rightarrow 0$
    $\mathbf{t}_{d/a}(j) \leftarrow {t_{d/a}}^{(k)}$
  end for

4.2 Pruning approach for flyby trajectories

In Ch.3, the flyby was treated in a combinatorial manner. In this regard, each transfer orbit is solved independently for the set of departure and arrival dates, and the search space of the doublets are recombined at the common date of flyby.

In fact, each porkchop plot can not be evaluated anymore individually. Instead, the feasibility of the combinatory flyby must be examined based on the delta-v at terminal points, in-/outbound relative velocities difference and the value of the turning angle

compared with the maximum allowed. In this case, the shape pruning must be adjusted. The concepts addressed in this paragraph demands to couple the knowledge matured in the Ch. 3 with the Gauss variational equation for the flyby, to further improve the pruning. The next paragraph is organised as follows. First, the adaptation of the shape pruning is tuned for the flyby problem, and second the pruning of the post-encounter arc is carried out.

4.2.1 Bounding region adaptation to triplets

Passing from direct to flyby trajectories requires attention for the generation of the bounding region. In the previous section, the solution for the pruning relied on the identification of the box vertices at the intersection between the solutions associated to tangential manoeuvre with a reference delta-v computed as the sum of relative velocities at the departure/arrival planets, see Eq. 4.2. Pruning the search space of the triplets on the delta-v of the doublets might result in over-pruning the search space of trajectory. In fact, for the pre-encounter transfer arc, imposing boundaries on the condition at the arrival translates into limiting the infinite velocity at the flyby, and the same happens for the departure condition of the post-encounter leg. Conversely, the bounding region approach can be applied to the incoming and outgoing transfer orbits constraining the tangential solutions on the relevant contribution of the delta-v for the terminal points: the departure condition for the former and the arrival one for the latter, respectively.

Therefore, Eq. 4.2 is now modified accordingly, using Eq. 4.4 and Eq. 4.5:

$$\Delta v_1 = \begin{cases} \sqrt{\mu\frac{1+e}{r_1}} - \sqrt{\frac{\mu}{r_1}} & \text{if} \quad r_1 \cdot v_1 = 0 \\ \sqrt{\frac{3\mu}{r_1} - \mu\frac{1+e}{r_2} - 2\mu\sqrt{\frac{1-e}{{r_1}^3}r_2}} & \text{if} \quad r_2 \cdot v_2 = 0 \end{cases} \tag{4.4}$$

$$\Delta v_3 = \begin{cases} \sqrt{\frac{3\mu}{r_3} - \mu\frac{1-e}{r_2} - 2\mu\sqrt{\frac{1+e}{{r_3}^3}r_2}} & \text{if} \quad r_2 \cdot v_2 = 0 \\ \sqrt{\frac{\mu}{r_3}} - \sqrt{\mu\frac{1-e}{r_3}} & \text{if} \quad r_3 \cdot v_3 = 0 \end{cases} \tag{4.5}$$

Eqs 4.4 and 4.5 provide the expression for the delta-v at the significant terminal points for the pre- and post-encounter orbit tangential to the circular coplanar orbit of the departure/flyby and flyby/arrival planet, respectively.

Conversely, from the pruning for the direct transfer, the bounding region obtained at the intersection of tangential solutions with the terminal delta-vs appears elongated towards a predominant direction, i.e. along tangential manoeuvres. Moreover, bounding regions can be refined to increase space occupancy for circular coplanar and real ephemerides using the methods described above.

4.2.2 Incremental pruning for post-encounter legs

MGA missions foresee multiple flyby along their cruise. Such condition limits the applicability of shape pruning to the first and final targeting problem, with no possibility to interact with the search spaces associated to the targeting problem connecting each flyby. Indeed, following the aforementioned reasoning, bounding the infinite velocity of a close encounter might result in discarding trajectories that were feasible.

A standard approach to evaluate the flyby requires a precise knowledge of the pre- and post-encounter conditions at the flyby to extract from the set of triplets those orbits that satisfy the infinite velocity difference and the turning angle, see Eq. 4.6:

$$\begin{aligned} v_\infty^+ - v_\infty^- &= 0 \\ \cos^{-1}\left(\mathbf{v}_\infty^+ \cdot \mathbf{v}_\infty^-\right) &\leq \delta_{\max} \end{aligned} \tag{4.6}$$

Indeed, the evaluation of the equality and inequality constraints described in Eq. 4.6 requires the resolution of the two Lambert's problems for their specific departure and arrival dates.

Nevertheless, terminal bounding regions can be connected and pruning of the search space of inner transfers can be performed considering the effect of the close encounters induced by the incoming transfer orbit. Starting from one of the terminal transfers and reconstructing the trajectory sequentially, the method requires to resolve the Lambert's problem associated to the pre-encounter condition to constrain the search space of the post-encounter leg a-priori based on the pre-existing knowledge the user might have about it.

Moreover, Gauss planetary equations derived for the disturbing acceleration of a close encounter offers upper and lower bounds for the relevant orbital parameters, i.e. the semi-major axis, the eccentricity and the argument of the periapsis for coplanar transfers, see Eq. 3.22.

For a predefined flyby sequence, physical limits of the post-encounter transfer can be derived, e.g the maximum semi-major axis and the minimum eccentricity, quantities that depends purely on the orbital geometry of the the i^{th} and i^{th+1} planets, as can be seen in Eq. 4.7:

$$a_{\max} = r_i + r_{i+1} \quad e_{\min} = \frac{|r_i - r_{i+1}|}{r_i + r_{i+1}} \tag{4.7}$$

Comparing these values with the limits derived by Gauss planetary equations for the incoming conditions at the flyby permits to exclude all the solutions whose minimum post-encounter semi-major axis is larger than the maximum and vice versa, i.e. whose maximum post-encounter eccentricity is lower than the minimum one, see Eq. 4.8:

$$a_{i-1,i} + \Delta a_{\min} > a_{\max} \quad e_{i-1,i} + \Delta e_{\max} < e_{\min} \tag{4.8}$$

For a Earth-Mars trajectory with a Venus flyby, the flyby pruning combined with the shape-based one derived from the arrival delta-v allows to considerably reduce the search space for the Venus-Mars leg, as it can be seen comparing Fig. 4.3a with Fig 4.3b:

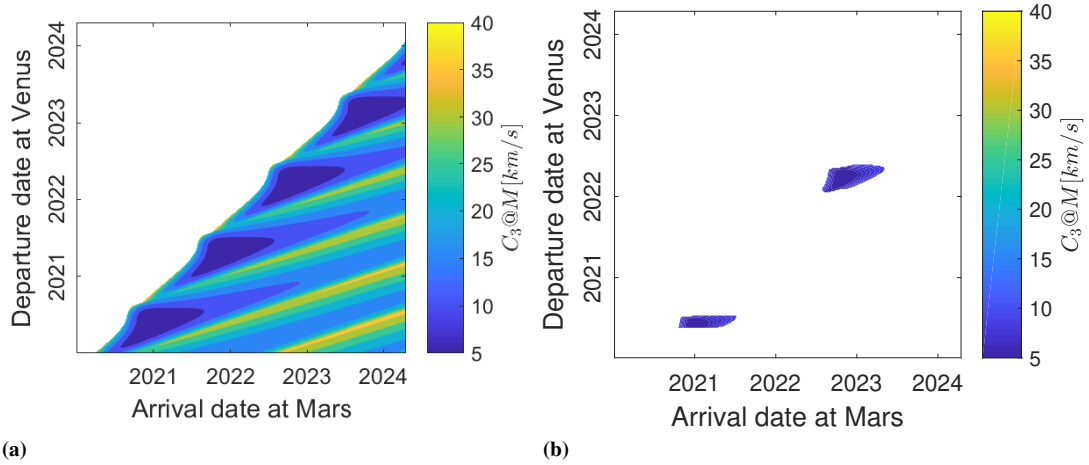

Figure 4.3: *On the left and on the right, the complete and reduced through shape-based and flyby pruning search space associated to the Venus-Mars leg for an Earth-Mars trajectory with a flyby at Venus.*

It is worth mentioning that the flyby pruning allows to automatically discard region of the search space that the shape-based one would have maintained, for instance the area around the second and forth delta-v minima at the arrival with Mars.

Part II

Final phase in planetary moon system

CHAPTER 5

Fly-by-map in the three-body problem

Planetary moon systems, such as the one of Jupiter and Uranus, present a significant different dynamics compared to the one observed in the solar system. In fact, despite a similar ratio in mass parameters (at least for the heaviest bodies), a difference of three order in magnitude for the orbital radii makes the system more compressed and, therefore, sensitive to the interaction of the gravitational attraction of the heaviest moons. Indeed, flybys at moons experience stronger perturbations compared to the planetary ones. In this situation, patched conics trajectories can undergo to significant deviations when optimised in the full body dynamics. A treatment in the three-body dynamics should be favoured.

In three-body dynamics, the trajectory can not be described analytically and has to be numerically propagated from an initial state. Studying the complete search space of the state vector, to analyse the interaction between the two gravitational fields, can be computationally intensive. An alternative to the state, is represented by osculating orbital elements, employed in mapping approaches. They approximate the dynamics by mapping the effect of the third body perturbation on an osculating orbit. Depending on how the gravitational interaction is modelled, semi-analytical or fully numerical methods are distinguished. Among the former the Keplerian map [2, 59] assesses the orbital variation via integration through Picard's iteration of a kick function approx-

imating the effect of third body at the close encounter. Instead, the flyby map [21] restores the numerical propagation after having observed that the kick approximation of the dynamics is affected by not negligible differences in modelling the third body interaction for energies that are still outside the limits of fully ballistic trajectories [45].

In planetary moon system the different ratio between the out-of-plane and in-plane components makes three-dimensional trajectories interesting and relevant to be studied. In particular, in the frame of the Europa Clipper mission, polar or high inclined close encounters are targeted to provide wide and high resolution coverage of the moon surface [12]) while containing the radiation dose [18].

The chapter deals with the extension of the applicability of the flyby map to the spatial dynamics proposing a new parametrisation required to handle the augmented degrees of freedom.

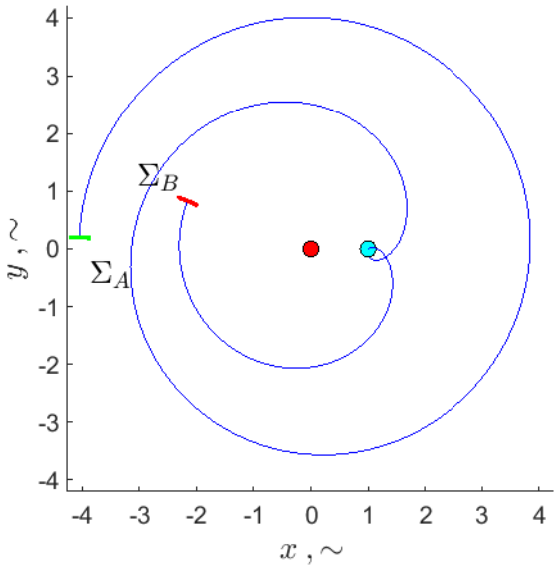

Figure 5.1: *The representation of Poincaré sections, Σ_A and Σ_B, along the orbit identifying the boundary conditions of propagation.*

5.1 The planar Flyby map

Whereas in the patched conics the effect of a close encounter can be immediately revealed by a discontinuity in the orbital elements, in the three-body dynamics the occurrence of a flyby is difficult to be evaluated from a variation in the state. Indeed, although the effect of a close approach is automatically considered in the equations of motion, the passage of the S/C within the SOI of the secondary is commonly used as revealing condition. The Flyby map captures the effect of the close approach on a osculating orbit evaluated at a Poincaré section in the phase space parametrised by (a, T, λ, f) coordi-

nates: the semi-major axis, a, the Tisserand parameter, T, the longitude of the periapsis λ in the rotating frame and the true anomaly, f, of the apsis which defines the position of the surface of section along the orbit at which the Cartesian state is converted into Flyby map parameters. Depending whether the semi-major axis is greater or smaller than the orbit of the secondary, the value of the flyby parameters is computed either at the apo- or the periapsis, in particular:

$$f = \begin{cases} -\pi & \text{if } a > 1 \\ 0 & \text{if } a < 1 \end{cases} \tag{5.1}$$

The Flyby map represents a numerical non-linear mapping:

$$\mathcal{F}: \quad (a_B, T_B, \lambda_B) \xrightarrow{\mathcal{F}} (a_A, T_A, \lambda_A) \tag{5.2}$$

in the phase space, which is convenient to study the flyby in the CR3BP . In the planar case, the Flyby parameters, ρ, can be expressed by three independent variables related to the osculating orbit (a, T, λ). The osculating periapsis, λ_A, modifies the condition of the close approach and can be considered as the control variable. The Tisserand parameter is related to the infinite velocity of the osculating orbit undertaking the close approach and approximates the total energy with an expression of the semi-major axis and eccentricity:

$$T = \frac{1}{a} + 2\sqrt{a\left(1 - e^2\right)} \tag{5.3}$$

Since the Tisserand Parameter is conserved during the flyby, its effect is observed in the variation of the semi-major axis, a, measured at he Poincaré sections, Σ_A and Σ_B, displayed in Fig. **??**, which identify the pre- and post-encounter conditions
Sequentially, three steps are required to compute the flyby map:

1. the initial conditions in flyby map parameters at the Poincaré section, Σ_A defined as:

$$\Sigma_A \equiv \left\{ (a, T, \lambda)_A \, | a_A \neq 1, r_S \left(a_A, T_A, \lambda_A, f_A^-\right) > 5R_{Hill} \right\} \tag{5.4}$$

   where $f_A^- = f - \varepsilon$, are converted in synodical coordinates through the transformation φ:

$$(x, y, \dot{x}, \dot{y})_A = \varphi^{-1}\left(a_A, T_A, \lambda_A, f_A^-\right) \tag{5.5}$$

2. the initial state is propagated numerically in the three-body dynamics until the

crossing with the following surface of section. The equation of motion for the CR3BP can be expressed in non-dimensional variables by Eq. 5.6:

$$\begin{aligned} \ddot{x} - 2\dot{y} &= x - \frac{(1-\mu)(x+\mu)}{((x+\mu)^2+y^2)^{1.5}} - \frac{\mu(x+\mu-1)}{((x+\mu-1)^2+y^2)^{1.5}} \\ \ddot{y} + 2\dot{x} &= y - \frac{(1-\mu)y}{((x+\mu)^2+y^2)^{1.5}} - \frac{(\mu y)}{((x+\mu-1)^2+y^2)^{1.5}} \end{aligned} \tag{5.6}$$

3. at the Poincaré section, Σ_B:

$$\Sigma_B \equiv \left\{ (a,T,\lambda)_B \,|a_B \neq 1, r_S\left(a_B, T_B, \lambda_B, f_B^+\right) > 5R_{Hill} \right\} \tag{5.7}$$

located at least at a distance of 5 Hill radii from the secondary, the final state is transformed back in flyby map parameters, see Eq. 5.8:

$$\left(a,T,\lambda,f^+\right)_B = \varphi\left(x_B, y_B, \dot{x}_B, \dot{y}_B\right) \tag{5.8}$$

where ${f_B}^+ = f + 2\pi + \varepsilon$ and r_S represents the distance of the S/C from the secondary and ε constitutes an infinitesimal quantity.

The Flyby map was successfully used to design low-energy trajectories to Ganimede, Titan and Triton [16]. Nevertheless, its application remains bounded to the planar dynamics, preventing from studying the 3D dynamics whose effect is fundamental to design multi-moon trajectories in the planetary moon systems, for instance the sequence of resonant flybys, Crank-Over-Top sequence (COTs), employed in the tour of Europa Clipper [12, 17].

5.2 The 3D Flyby map

The 3D Flyby map improves the planar one, considering the spatial dynamics of the CR3BP . Despite a similar logic in the workflow, the increased number of degrees of freedom requires additional parameters to describe the dynamics of the flyby. Therefore, the following paragraphs concern the choice of variables to parametrise the phase space, their relation to patched conics, their domain and the properties of the Flyby map.

5.2.1 Parametrisation

The key concept of the Flyby map revolves around the possibility to reduce the analysis of the flyby effect in the CR3BP from the whole state to fewer parameters. In patched conics, close encounters can be studied with a set of three variables, e.g v-infinity, pump and crank angles in the v-infinity globe [64] or the components of impact parameter b [68]. Small variation of these parameters allows to scan all the possible condition

of flyby and study its effect on the post-encounter orbit. This knowledge enables an inexpensive targeting of the close approach from a condition at infinite, far from the secondary.

Similarly to the Keplerian map, the Flyby map maintains the idea of studying the variation of the orbital elements induced by the flyby on an osculating trajectory. Although, it substitutes the semi-analytical integration, handled in the phase space of the orbital elements, with the direct propagation of the state vector in the dynamics of the CR3BP, described by Eq. 5.6. The conversion from the Cartesian state to the Flyby map parameters is performed by the coordinate transformation φ at the positions along the orbit identified by the Poincaré sections. Their use enables reducing the set of coordinates associated to a continuous dynamics into a lower-dimensional discrete set of parameters and allows to take the true anomaly out of the equation. The choice of the Tisserand parameter as Flyby map variable is legitimated by the fact that this quantity is expected not vary as the total energy is conserved in the three-body dynamics.

In the planar case, this reasoning allowed to consider only two parameters to account for the flyby effect. The semi-major axis, a, and the osculating argument of the periapsis, λ, were chosen as output variable and control parameter, respectively. The choice is not equivocal. Indeed, within a narrow interval, the control variable spans all the possible configuration of close approach for the specific energy level considered. At the same time, the semi-major axis is sensitive to the flyby effect induced by the osculating argument of the peri-apsis: in fact, in patched conics, the value assumed by the control variable at the Poincaré section Σ_A directly identifies the exit condition of the v-infinity. The flyby effect in the planar case is a function of one unique variable.

In the 3D dynamics, considering the out-of-planet component requires to handle six coordinates to describe the dynamics. Repeating the reasoning performed for the planar flyby map, if the Tisserand parameter, T, is maintained and the true anomaly, f, is removed by the introduction of the Poincaré section, then the increase of degrees of freedom leaves three free variables in play. A convenient choice of coordinates could be the set of $(a, T, i, \varpi, \omega, f)$ parameters, where ϖ is the osculating longitude of the periapsis, computed as the sum of Ω_{rot}, the right ascension of the ascending node in the rotating frame, and ω, the argument of the periapsis. Fig. 5.2 displays these quantities on a schematic of the orbit of Europa Clipper in the Jupiter-Europa system.

Such formulation is particularly interesting for several reasons. The inclination accounts together with the semi-major axis for the flyby effect, induced by the different combination of the osculating longitude and argument of the periapsis, spanning all the various locations of the close approach. Therefore, semi-major axis and inclination can be considered as output parameters, while the osculating longitude and the argument of

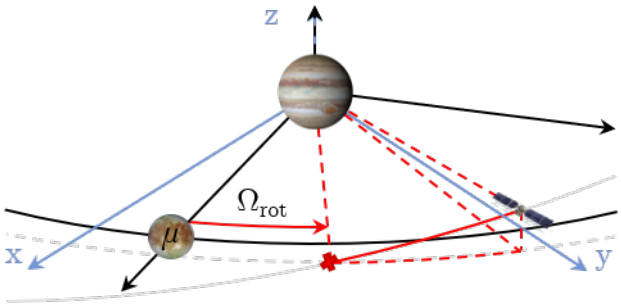

Figure 5.2: *The representation of right ascension of the ascending node, Ω_{rot}, measured from the line connecting the primaries in the inertial frame.*

the periapsis as control variables for the Flyby map. Small variation in the values of the free-variables can results in significant change of the output parameters. At the same, performing a correction of the targeting of a specific close approach from an infinite condition affects the propellant consumption by relatively small delta-vs (few m/s). In the end, the choice of the osculating longitude and the argument of the periapsis as control variables ensures that the transformation, φ, from Cartesian to Flyby map coordinates is invertible and that the attainable set of interesting flyby remains bounded to a neighbourhood of 0, as we will in the next section.

5.2.2 The control variable in patched conics

Identifying a set of initial conditions for the spatial Flyby map that lead to the close encounter is not trivial. A broad search in the domain of the control variables is computationally intensive, however, if the orbital energies under study are high enough, a relation between the orbital elements and the v-infinity parametrised by pump and crank angles [65] can be derived in patched conics. and used as initial guess for the control variables.

Here, the absolute velocity of the S/C with respect to the primary, $\mathbf{v}$, is the sum of the relative velocity with respect to the secondary, v_∞, and its velocity in the inertial reference of the primary, v_{pl}, as shown by Eq. 3.1. The velocity triangle, represented in Fig. 5.3, display this equivalence:

in which γ constitutes the flight path angle and x, y and z are the unit vectors of the synodical frame, co-rotating with the secondary and centred in its barycentre. In this system, the pump angle, α, is defined between the velocity of the secondary and the infinite velocity, while the crank angle, κ, is measured between the line connecting the primaries and the projection of the asymptotic velocity on the plane normal to the ecliptic, see Eq. 5.9

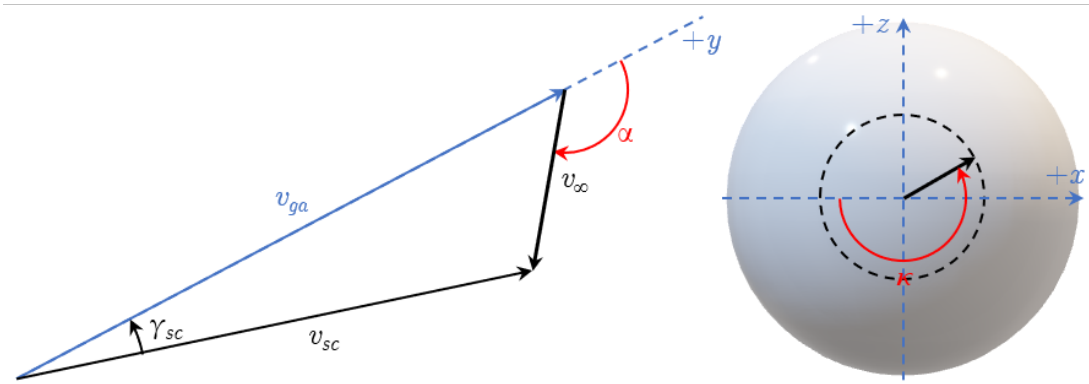

Figure 5.3: *Schematic of the velocity triangle and the pump and crank angles, α and κ, on the left and the right respectively.*

$$\cos\alpha = \frac{1-v_\infty^2-a^{-1}}{2v_\infty} \qquad \tan\kappa = \frac{\tan\gamma_{sc}}{\sin i} \tag{5.9}$$

where i is the inclination measured between the north axis and the angular momentum.

In particular, for a given semi-major axis and a given Tisserand parameter, it is possible to derive an expression of the infinite velocity depending only on the crank angle from which it is possible to derive the Flyby map parameters from Eq. 5.10:

$$\begin{gathered}(a, T, i, \bar{\varpi}, \bar{\omega}, f) = \varphi\left(\mathbf{v}_\infty(\kappa)\right) \\ \mathbf{v}_\infty = v_\infty \begin{bmatrix} \sin\left(\alpha(a)\right)\cos\kappa & \cos\left(\alpha(a)\right) & \sin\left(\alpha(a)\right)\sin\kappa \end{bmatrix}^T\end{gathered} \tag{5.10}$$

where the bar accent refers to the unperturbed quantities.

Their solution corresponds to the two-body orbit intercepting the secondary. Therefore, all the attainable flyby effects can be studied perturbing the control variables around the osculating initial guess and studying the evolution of the associated state under the three-body dynamics.

Such formulation results convenient as it allows to correlate the inclination to the control variables through the crank angle. Since the the crank angle is not defined in the CR3BP , the inclination can be used as a discrete parameter similarly to the semi-major axis and the total energy. Moreover, the inclination can be bounded to only those values that lead to a close encounter with the secondary in patched conics. Fig. 5.4 displays the trend of the inclination, osculating right ascension of the ascending node and argument of the periapsis in blue, green and magenta respectively, as a function of the crank angle, a $4:1$ resonant orbit approaching Europa with 4 km/s of v-infinity. It can be observed that the crank angle unambiguously determines an osculating orbit in patched conics. Although this quantity is bounded to its gravitational model, not representative

in three-body problem and not directly measurable far from the secondary, condition required by the Poincaré section. The inclination, instead, is the perfect candidate given its importance in the design of the resonant flyby sequence of Europa Clipper. Fig. 5.4 shows that the crank angle allows to identify boundaries for the inclination, within which a given level, represented with the dashed black line, intercepts on the blue curve the values of crank angles for which the related osculating longitude and argument of periapsis are computed. These solutions are associated to symmetric trajectories with the respect of the line connecting the primaries, as displayed by Fig. 5.4 for the $4:1$ resonant orbit with 4 km/s of relative velocity with respect to Europa.

Integrating an osculating orbit undertaking a flyby in a more complex dynamics, in this case the one of the CR3BP , results into collision or large deviations in position and velocity. Such situation occurs due to the fact that the dynamics switches from a discrete system with point-less attractors and dimension-less SOI, (either infinite or nill), to a continuous one. In particular, considering multiple bodies with their finite dimension causes the emergence of collision corridors and chaos due to the combined interaction between multiple gravitational fields. The pull of the secondary extends way beyond the limit of its SOI and slightly modifies the condition at the close approach inducing the deviations observed.

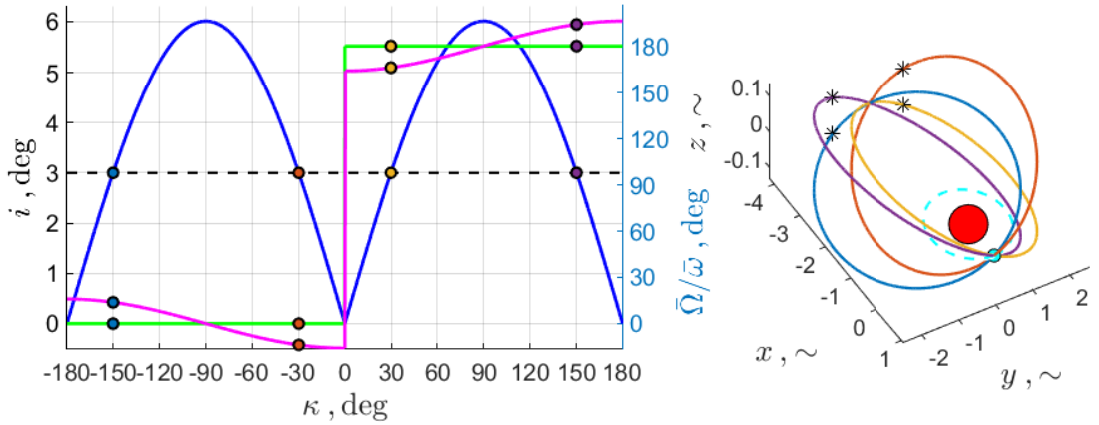

Figure 5.4: *On the left, the domain of attainable inclinations (in blue), right ascensions of the ascending node (in green) and argument of the periapsis (in magenta) as a function of the crank angle for 4:1 resonant orbit at Europa with 4 km/s of infinite velocity. On the right, the orbits with 3 degrees of inclination.*

5.2.3 The attainable set of the control variables

Considering the objective of the Flyby map, among all the different initial guesses assumed by the control variable, only those that results in a close approach within the first period are of interest.

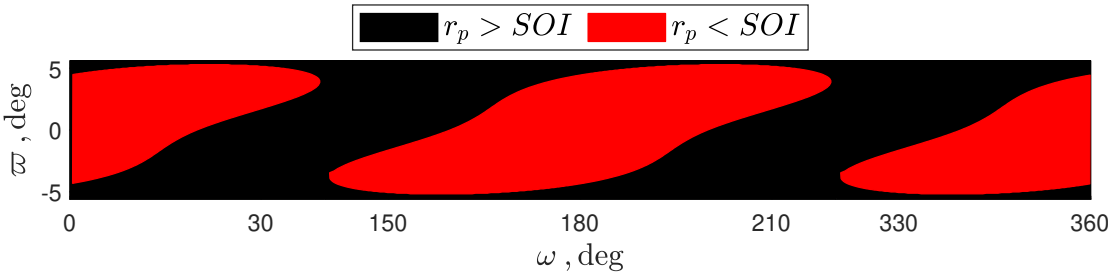

Figure 5.5: *The feasible domain of the argument and osculating longitude of the periapsis for a 4:1 resonant orbit at 3 degrees of inclination and 4 km/s infinite velocity at Europa. In black and red respectively, the initial conditions having a close approach within the first period.*

Exploring the space of the control variables, three different red islands appears as it can be seen from Fig. 5.5. It is curious to note that these regions can be recombined in two identical structures 180 degrees apart in argument of the periapsis.

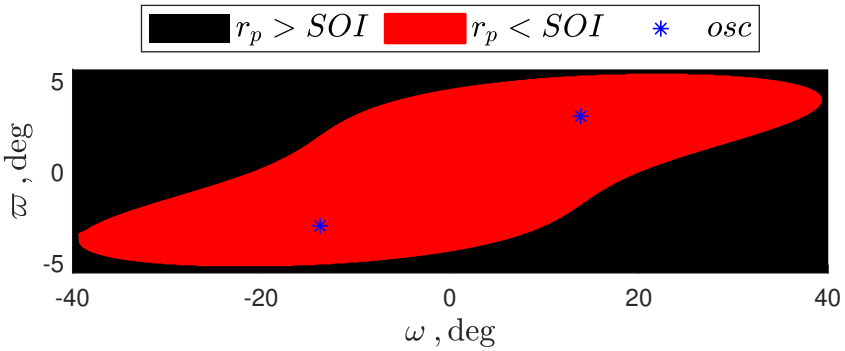

Figure 5.6: *One of the two structure of the feasible domain of the control variables , see Fig. 5.5, obtained for a 4:1 resonant orbit at 3 degrees of inclination and 4 km/s infinite velocity. In black and red respectively, the initial conditions having a close approach within the first orbital period, in blue the unperturbed solutions obtained in patched-conics.*

$$\mathcal{A}(\mathcal{F}) : \left\{ (\omega_A, \varpi_A) \, | r_p \left(a_A, T_A, i_A, \omega_A, \varpi_A, f_A^- \right) \leq R_{\text{Hill}} \right\} \tag{5.11}$$

Eq. 5.11 identifies the attainable set, $\mathcal{A}(\mathcal{F})$, of the control variables for the non-zero flyby effect. This condition is ensured by checking that the close approach distance, $r_{S\min}$ is within the SOI limit. The attainable set is a proper subset of the domain of the control variable $\mathcal{D}(\mathcal{F})$:

$$\mathcal{A}(\mathcal{F}) \subset \mathcal{D}(\mathcal{F}) : \{ \omega_A \in [0, 2\pi), \varpi_A \in [-\pi, \pi) \} \tag{5.12}$$

It is interesting to note that the Flyby map becomes the identity transformation for the values of the control variables that does not belong to the attainable set:

$$(\omega_A, \varpi_A) \notin \mathcal{A}(\mathcal{F}) \Rightarrow \mathcal{F} \equiv \mathbb{I} \Rightarrow (a, T, i, \omega, \varpi)_B = (a, T, i, \omega, \varpi)_A \tag{5.13}$$

The distribution of the control variables is somehow associated to the patched conics initial guess derived in Eq. 5.10. From Fig. **??**, it is easy to observe that two distinct distributions seem to grow around the blue markers, associated to patched conics solutions, and merge together resulting in the the final configuration.

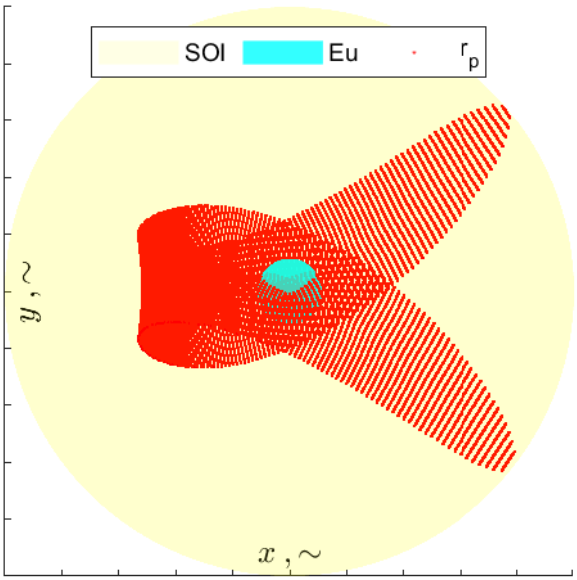

Figure 5.7: *The distribution of close approaches occurring from perturbing the initial longitude and argument of the periapsis of a 4:1 resonant orbit at 3 degrees of inclination and with 4 km/s infinite velocity.*

Fig. 5.7 confirms this hypothesis displaying the location of the close approaches resulting from the feasible initial conditions of the control variables. The distribution appears in an ordered surface of close approaches, which is less chaotic than expected. It folds on itself evolving towards the SOI from the same side, recalling the bimodal behaviour of two distributions, previously mentioned.

In fact, the shape of the interesting part of the domain is directly dependent on the maximum close approach distance considered. In this case, the SOI of Europa defines the criterion to label an initial condition and its associated trajectory feasible or not. Indeed, it can be thought that for a specific maximum altitude of the flyby, there exist four distinct distributions of ther control variables, one per each osculating solution. At the same time, extending hypothetically the close approach distance at infinite, the feasible domain grows and incorporate the domain of the control variables completely.

5.2.4 Properties of the Flyby map

A given level of inclination, such as the one represented in Fig. 5.4, identifies four patched conics solutions for the control variables. Their value determines the centres of the distributions associated to the attainable set, as suggested by Fig. **??**. It is interesting to note that the symmetry of the unperturbed orbits, determined for the set of semi-major axis and Tisserand parameter considered is maintained in the CR3BP .

Indeed, the Flyby map preserves the symmetries of the CR3BP through the coordinate transformation φ, whose effect on the orbit can be visualised in the Cartesian frame.

This property can explains the existence of the two identical structures, 180 degrees apart in argument of the periapsis, associated to the atteinable set of the control variables of the Flyby map. Indeed, the symmetry of the CR3BP with the respect of the out-of-plane component, z, is converted by the transformation φ in the equivalence:

$$(a, T, i, \varpi, \omega) = (a, T, i, \varpi, \omega + \pi) \tag{5.14}$$

Eq. 5.14 allows to reduce the domain of the argument of periapsis by half, considering only the range $(-\frac{pi}{2}; \frac{pi}{2})$. Indeed, the flyby effect obtained by the flipped out-of-plane component, $-z$, is expected to be equal to the one induced by symmetric orbits with respect to the orbital plane.

Similarly a combination of two different symmetries allows to derive the inverse Flyby map F^{-1} from the direct one by a simple sign change:

$$\mathcal{F}^{-1} = \Theta \circ \mathcal{F} \circ \Theta \quad \text{where} \quad \Theta(a, T, i, \omega, \omega) = (a, T, i, -\omega, -\omega) \tag{5.15}$$

5.3 Controlling the Flyby map

In the previous section, it has been shown how it is possible to switch from a planar to a spatial formulation, to reduce tthe study of the flyby effect from Cartesian coordinates into slowly varying parameters and control variables, to perform a grid-search in the space of the free-variables perturbing an initial guess derived in patched conics, to extract from their domain an atteainable set of interesting flybys. In this section, the results are summarised. In particular, the first paragraph presents graphically the flyby effect derived from the 3D Flyby, while the second part carries out the identification process of the two families of flyby trajectories.

5.3.1 The Flyby map graph

Having a bi-dimensional space for the control variables makes the representation of the results less intuitive compared to the planar case. In fact, any output parameter, depending at the same times on both control variables, requires a three-dimensional representation. Moreover, the intrinsic shape of the attainable set of the free-variables complicates further its visualisation. The most clear way to display the flyby effect is via contour plot. In this way, the representation remains 2D moving the output variable to a separate axis and leaving to colour the task of showing its trend.

With that in mind, the information held by each output variable can be evaluated in the light of flyby features and cross-compared to understand better how the close approach modify the orbit. Fig. 5.8 displays the the trend of the output parameters observed at the post-encounter Poincaré section, Σ_B: in particular from the top to the bottom one can observe the distribution of the resonances and inclinations induced by the control variables and a zoom-in, identified by the white square, of the areas experiencing the largest variations in Fig. 5.9.

Eq. 5.16:

$$\begin{aligned} (a,T,i,\varpi,\omega)_A^{(i)} &\xrightarrow{\mathcal{F}} (a,T,i,\varpi,\omega)_B^{(i)} \rightarrow (a,T,i,\varpi,\omega)_A^{(i+1)} \\ (a,T,i,\varpi,\omega)_A^{(i+1)} &= \left(a_A^{(i)}, T_A^{(i)}, i_B^{(i)}, \varpi_B^{(i)} - 2\pi\sqrt{a^3}, \omega_B^{(i)}\right) \end{aligned} \tag{5.16}$$

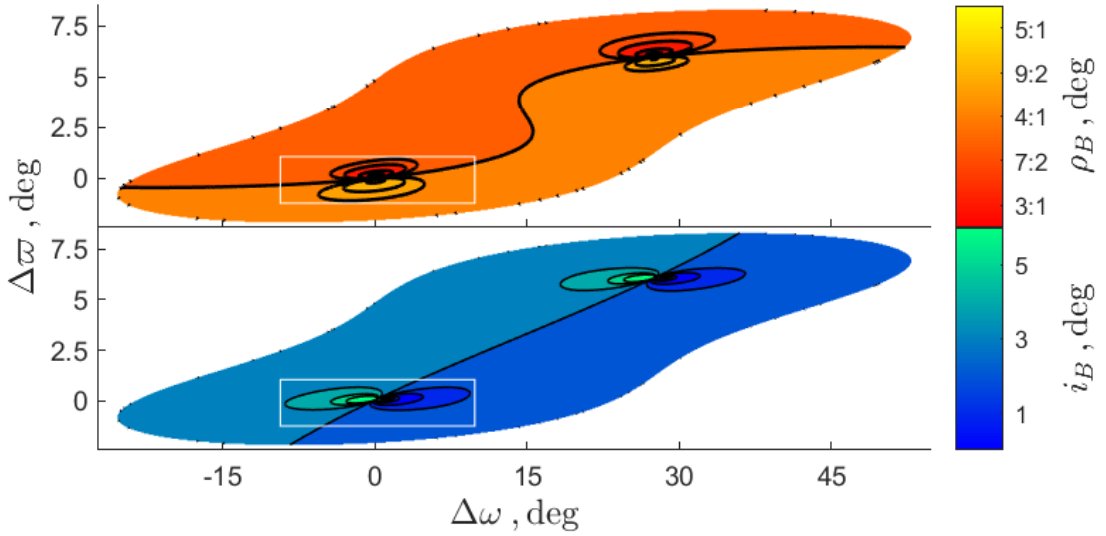

Figure 5.8: *The characteristic information resulting from perturbing the osculating longitude and the argument of the periapsis for a 4:1 resonant orbit at 3 degrees of inclination, 4 km/s infinite velocity and -30 degrees of crank angle. From the top to the bottom, the colour-coded distributions of the period and the inclination of the post-encounter osculating orbit.*

Their trend can be evaluated in light of the distance and orientation distributions

obtained at the close approach.

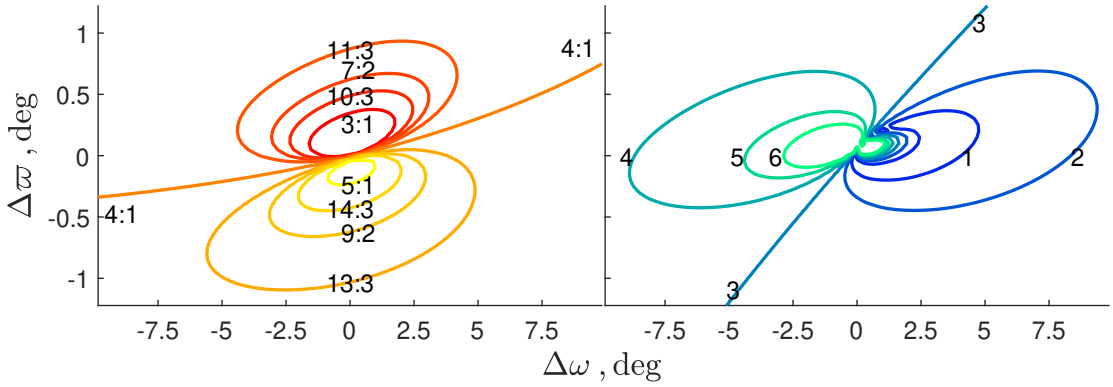

Figure 5.9: *A zoom-in on the areas with the largest variations in period/semi-major axis, left, and inclination, right, displayed with the white box in Fig. 5.8*

Fig. **??** collects from the top to the bottom the trend of minimum altitude, $h_{\min}$, the longitude, λ, and latitude, ϕ, of close encounter, respectively. For tidally locked moon, the synodical moon-centered frame is equivalent to the body fixed one and therefore the rotating coordinates, upon translation, can be directly used to compute latitude and longitude of the spacecraft with the respect of the secondary.

Comparing Fig. 5.9 with Fig. 5.10, one can observe that the there is a perfect overlap between the areas undergoing to the largest variations in semi-major axis and inclination and those associated to a collision. As expected, the largest deviations occurs for the lowest altitude flybys.

Two interesting insights can be deduced comparing the distribution of the output parameters, in Fig. 5.8, with the direction of the close approaches, see Fig. 5.10. In particular, it can be seen that there exist flybys that preserves the orbital period, not modifying the post-encounter semi-major axis. This situation occurs when the close approach lies on the line connecting the primaries, associated to a longitude of 0 or 180 degrees. At the same time, there exist flybys that freeze the inclination, condition experienced when the minimum altitude passage lies on the ecliptic plane,i.e. for 0 degrees latitude. Moreover, a positive increment in inclination is obtained for close approaches occurring in the southern hemisphere, while a reduction is obtained for close approaches occurring in the norther hemisphere.

5.3.2 Families of flybys

The comparison of the period/semi-major axis distribution with the longitude of the minimum altitude passage suggests an intuition that could not be made from a purely patched-conic analysis. Considering a $4:1$ resonant orbit with Europa, flybys can be distinguished depending whether their longitude is in the neighborhood of 0 or π rad.

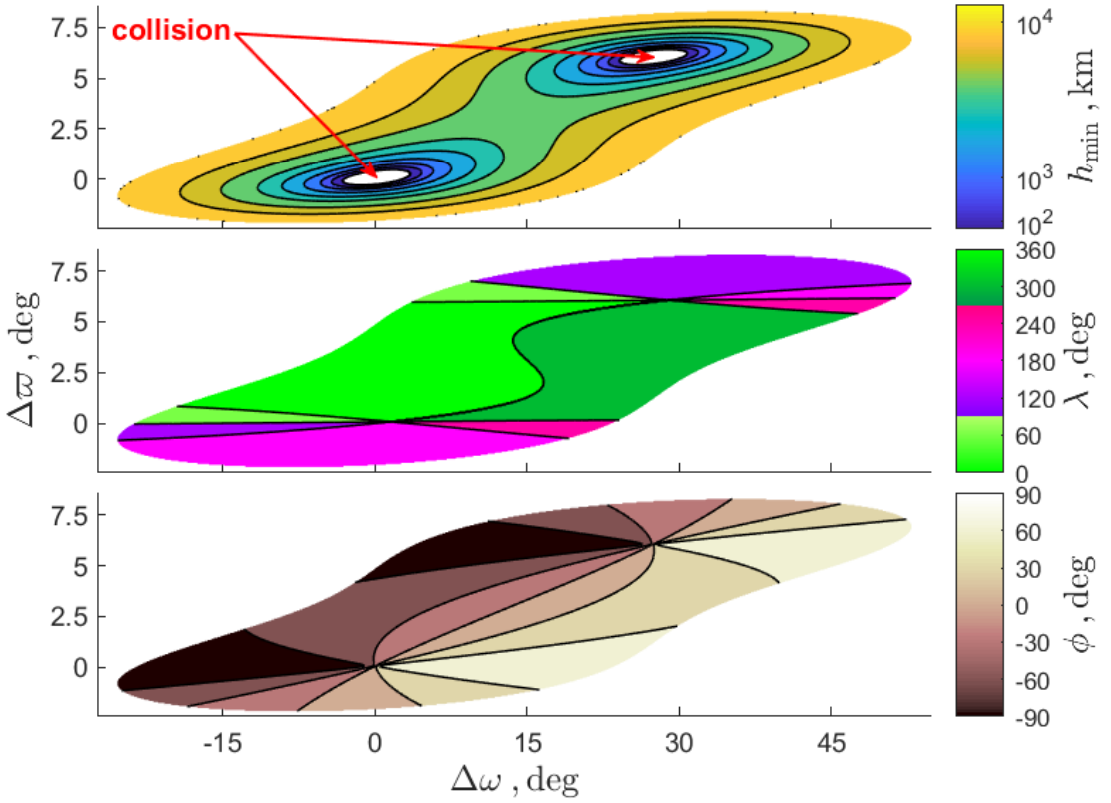

Figure 5.10: *The distribution of the flyby properties resulting from perturbing the osculating longitude and the argument of the periapsis for a 4:1 resonant orbit at 3 degrees of inclination, 4 km/s infinite velocity and -30 degrees of crank angle. From the top to the bottom, the colour-coded distributions of the close approach distance, longitude and latitude.*

From Fig. Fig. 5.11, it can be observed that the transition is more evident on the ϖ-axis. Indeed, the central part of the attainable set is occupied by the green area, associated to sub-Jovian close approach, while the anti-Jovian flyby represented by the magenta regions spans at the side.

For the initial conditions considered for the pre-encounter semi-major axis, the two families of longitude of the close encounter can be related to two families of flybys: indeed, direct (type I) flybys pass behind the orbit of Europa, have their close approach in the anti-Jovian hemisphere and coincide with the magenta area, while retrograde (type II) ones overtake the moon passing from the sub-Jovian hemispheres and are associate to green part of the distribution.

Observing the contours lines associated to the resonances, displayed on the top of Fig. 5.8, those associate to retrograde flyby and lying in the green area appear way more condensed. while the countour lines related to prograde flybys look more outspread.. Such information suggests that there exist two families of flyby, see Fig. 5.11, type I and type II , or prograde and retrograde, or anti-Jovian and sub-Jovian, and that type II

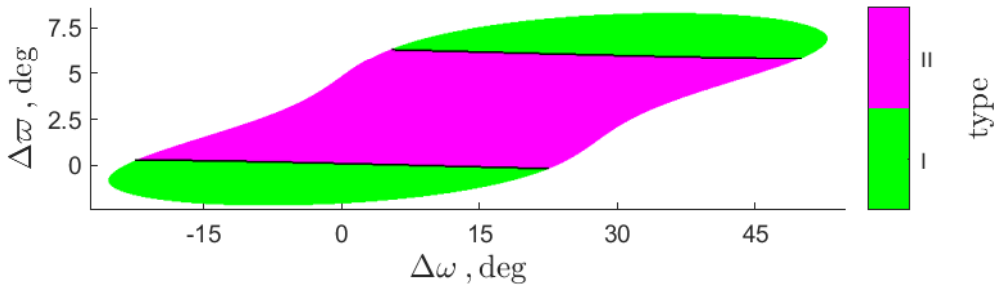

Figure 5.11: *The identification of two families of flyby, type I and type II represented in magenta and green, respectively.*

is less efficient compared to type I.

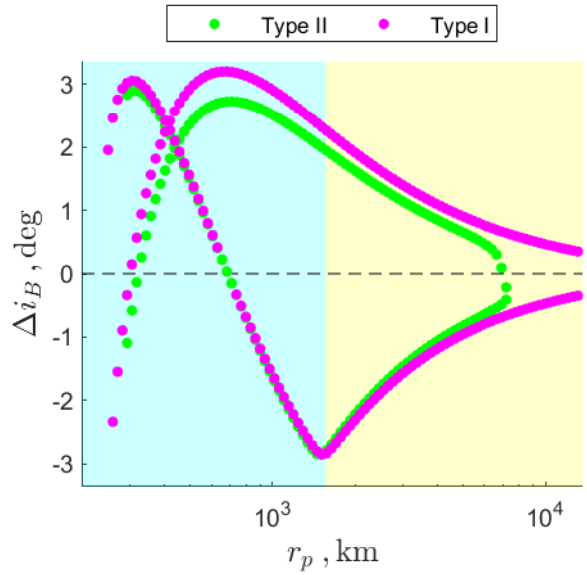

Figure 5.12: *The identification of two families of flyby, type I and type II represented in magenta and green, respectively.*

A quick test to verify this hypothesis consists in representing the variation of one of the output parameters while the other one is preserved. Fig. **??** displays the trend of the inclination variation for a resonant flyby, which preserves the semi-major axis. In particular, it can be observed that at each passage, prograde flybys, in green, induces always a larger deviation in inclination compared to retrograde ones, in magenta.

CHAPTER 6

Trajectory refinement

The trajectory design is a task that any mission analyst aims to perform in the dynamical model closer to the operational scenario. However, this situation occurs rarely. Most of the time, the design is performed in a simpler dynamics, for instance the ones of the two or three-body problem. The trajectory is split in several legs that exist separately and independently from each other and are connected resolving the discontinuity at the boundary conditions through a delta-v manoeuvre that needs to be minimised. Nevertheless, integrated in the full-body accounting for n-body perturbations, such as the solar radiation pressure, the J_2 effect at each planet and the gravitational interaction with other bodies, the trajectory might experience large deviations at the patching points and requires to be refined through optimisation.

Previous chapters dealt with different maps that exploit extensively grid search methods to scan the search space and representation of the transfer and flyby problem in convenient set of elements, and obtain an assessment of the change induced by the dynamics. Specific conditions can be extracted from the data via interpolation, however, when integrated, large errors are measured in the constraints that were used to generate them. The main reason can be searched in the flyby, source of a strong non-linearity that makes the system extremely sensitive to the entry conditions before the flyby itself. In fact, infinitesimal changes of the state at the close approach can

result in significant variations of the trajectory, while far from the secondary, it is difficult to target the conditions at the close encounter that satisfy the requirements of the optimisation as even more small corrections can completely alter the entry conditions at the secondary, inducing a different flyby. Identifying a good strategy to deal with the flyby is necessary to achieve the feasibility required for the optimiser to converge to the minimum.

The chapter provides insights on the flyby optimisation and on the approaches implemented in this work to refine initial guesses interpolated on maps generated by grid search.

6.1 Optimisation of flybys

Refining trajectory with flybys in any dynamics different from the two-body problem one is not a trivial task. Indeed, patched conics allows to evaluate the conditions at the close encounter in terms of the turning angle and the difference between the relative incoming and outgoing velocities, see Eq. 4.6, that must be increased or decreased with delta-v when the inequality constraint is not satisfied, see Eq. 3.3. Instead, in other dynamical models, the trajectory has to be numerically propagated and its modification induced by the flyby is a direct consequence of the interaction of the S/C velocity with the inverse-squared gravitational field of the planet, that depends on the relative position of the S/C with respect to the planet, see Eq. 5.4. Switching from one to another dynamics is a task that can be performed through optimisation. In particular, direct methods alter an initial guess, i.e the Cartesian state, in a gradient descend flavour to resolve the discontinuities that arise from integrating an orbit in a dynamical model different from the one used for design and arrive a continuous realistic trajectory. However, given the orbit sensitivity to the flyby, a reckless optimisation strategy might not converge to the local minimum solution.

The choice on the approach to use is binary and consists in selecting as initial guess a condition at the close approach or at infinite.

6.1.1 Infinite conditions targeting from close encounters

The idea behind this approach relies on breaking the sensitivity to the flyby initialising the optimisation at the point whose variation induces the largest effect on the orbit: the close approach. The strategy consists in propagating the trajectory backward and forward in time from the close encounter state $\mathbf{x}_p$ that minimise the objective function $\mathbf{J}(\mathbf{x})$ and satisfy equality and inequality constraints, $\mathbf{g}(\mathbf{x})$ and $\mathbf{h}(\mathbf{x})$ vectors. Among the different equality constraints that the optimisation might be required to resolve, it is important that the initial state satisfies the close approach condition, see Eq. 6.1:

$$\mathbf{x}_p = \{\mathbf{r}_p, \mathbf{v}_p\} \quad \text{s.t.} \quad \begin{matrix} \mathbf{r}_p \cdot \mathbf{v}_p = 0 \\ r_p \leq R_{\text{Hill}} \end{matrix} \tag{6.1}$$

Eq. 6.1 requires that the initial point from which the trajectory is propagated is the state at the close approach, identified as the point along the orbit within the SOI of the planet of flyby whose relative velocity is perpendicular with respect to its relative position vector, in other words at the hyperbola pericentre

Identified the initial guess, the optimisation can start.
In patched conics, the position vector and the velocity of the close approach can be also explicitly identified by the incoming and outgoing infinite velocities at the planet of flyby in terms of the feasible turning angle and the flyby delta-v, see Eq. 6.2:

$$\begin{aligned} \mathbf{r}_p &= -\frac{\mu}{v_\infty^2}\left(\frac{1}{\sin\frac{\delta}{2}} - 1\right)\frac{\mathbf{v}_\infty^+ - \mathbf{v}_\infty^-}{\|\mathbf{v}_\infty^+ - \mathbf{v}_\infty^-\|} \\ \mathbf{v}_p &= \sqrt{v_\infty^2 + \frac{2\mu}{r_p}}\left(\frac{\mathbf{v}_\infty^- \times \mathbf{v}_\infty^+}{\|\mathbf{v}_\infty^- \times \mathbf{v}_\infty^+\|}\right) \times \frac{\mathbf{r}_p}{r_p} \\ \text{where} \quad \delta &= \begin{cases} \cos^{-1}\left(\frac{\mathbf{v}_\infty^+ \cdot \mathbf{v}_\infty^-}{v_\infty^2}\right) & \text{if } \delta \leq \delta_{\max} \\ \delta_{\max} & \text{otherwise} \end{cases} \end{aligned} \tag{6.2}$$

where δ is the turning angle and with the maximum turning angle δ_{max} defined in Eq. 3.4. If the incoming and outgoing infinite velocities at the close encounter differ in magnitude, a powered flyby must be considered and the close approach distance can be determined iteratively considering the different contribution in turning angles of the incoming and outgoing velocities, see Algorithm 3:

Algorithm 3 Close approach distance for powered flyby.

Require: v_∞^-, v_∞^+, μ, RelTol

Parametrise $\delta^\mp$ as a function of r_p: $\frac{\delta^\mp}{2} \leftarrow \sin^{-1}\left(1 + \frac{v_\infty^{\pm\,2} r_p}{\mu}\right)^{-1}$

Ensure: $\frac{\delta^-}{2} + \frac{\delta^+}{2} - \cos^{-1}\left(\frac{\mathbf{v}_\infty^- \cdot \mathbf{v}_\infty^+}{v_\infty^- v_\infty^+\|}\right) \leq$ RelTol

The associated velocities at the minimum flyby altitude can be determined substituting in Eq. 6.2 the different value of pre- and post-encounter infinite velocities. Instead, if the preliminary design is performed in a different dynamical model, the state of the periapsis can be derived during the trajectory propagation through an event function that checks when the close approach condition, see Eq. 6.1, is satisfied.

Algorithm 4 shows an application of the close approach optimisation strategy to refine flyby in the CR3BP dynamics
with the terms identified by the (i) and (0) superscripts associated to the free-variables

Algorithm 4 Close approach optimisation for flyby refinement in the CR3BP .

Require: $\mathbf{x}_p^{(0)}, t_-^{(0)}, t_+^{(0)}, T, \mathbf{x}_d, \mathbf{x}_a, \mu$

Integrate the trajectory backward and forward: $\mathbf{x}_{d/a}^{(i)} \leftarrow \int_0^{t_{\mp}^{(i)}} \Omega_{\text{CR3BP}} \left(t, \mathbf{x}_p^{(i)}\right) \text{dt}$

Ensure:

$$\min \left(\|\mathbf{v}_d^{(i)} - \mathbf{v}_d(t_-^{(i)})\| + \|\mathbf{v}_a^{(i)} - \mathbf{v}_a(t_+^{(i)})\| \right)$$

$$\text{subject to:} \quad \mathbf{g}(\mathbf{x}): \begin{cases} \mathbf{r}_p^{(i)} \cdot \mathbf{v}_p^{(i)} = 0 \\ \mathbf{r}_d^{(i)} - \mathbf{r}_d(t_-^{(i)}) = 0 \\ \mathbf{r}_a^{(i)} - \mathbf{r}_a(t_+^{(i)}) = 0 \end{cases}$$

$$\mathbf{h}(\mathbf{x}): \begin{cases} \left|t_+^{(i)} - t_-^{(i)} - T\right| - \varepsilon \leq 0 \\ \left\| \frac{2\mu}{r_p^{(i)}} - {v_p^{(i)}}^2 \right\| \leq 0 \end{cases}$$

and their initial guess respectively. It is interesting to note that, while the equality constraints, $\mathbf{g}(\mathbf{x})$ ensure targeting the position of the planets at departure and arrival, $\mathbf{r}_d$ and $\mathbf{r}_a$, the inequality constraint guarantee at least a parabolic velocity at the close approach, avoiding to be captured at the planet of the flyby, and allows a relaxation on the total time of flight, limited to a neighborhood of its original value T, and prevents to over-constrain the optimisation problem. The time of flight associated to the pre- and post-encounter legs are considered with sign with respect to the time origin fixed at the close approach.

6.1.2 Close approach targeting from the SOI

Despite performing a manoeuvre at the minimum flyby altitude results optimal in a delta-v perspective, as the largest effect on the trajectory occurs at the maximum velocity, it does not represent a real operational scenario of the mission. Several reasons contribute to prefer anticipating the manoeuvre execution and performing it far from the close approach in spite of its additional cost:

- the variability of the flyby effect on the post-encounter trajectory induced by small changes in the state at close approach;
- the difficulty in detecting the minimum passage condition autonomously (on board the S/C), independently (e.g without observations) and accurately;
- the relative short time of the flyby and high likelihood to miss the tight execution window associated to the manoeuvre;
- the impossibility of retrieving the S/C due to execution errors.

Moreover, the operational execution of a flyby foresees in general the implementation of two correction manoeuvres to reduce the uncertainty associated to the flyby

knowledge error estimated a couple of days prior and post-encounter via orbit determination, [11].

Therefore, the optimisation of the flyby by correcting the entry and exit conditions at the SOI represents a strategy closer to the actual operational scenario for flyby and a compromise between the extreme cases associated to initialising the optimisation to the close approach or at the terminal points. Although the idea behind the two strategies is similar as it concerns identifying the correction manoeuvres that restore the continuity of the trajectory in a dynamical system more accurate compared to the preliminary design one, the optimisation is more prone to converge in the former case than in the latter. This behaviour is directly connected to the different sensitivity of the initial guess of the flyby dynamics. However, the result at convergence must be similar since the objective function remains evaluated at the terminal points and the constraints imposed achieve essentially the same goal.

Algorithm 5 Flyby refinement in the CR3BP from conditions at the SOI.

Require: $\mathbf{x}_{\text{SOI}}^{\mp\,(0)}$, $t_{d/a}^{(0)}$, $\Delta v_{\text{SOI}}^{\mp\,(0)}$, T, $\mathbf{x}_{d/a}$, μ, $\Delta v_{\min}$

Integrate the trajectory till Eq. 6.1 is satisfied: $\mathbf{x}_p^{\mp}(i) \leftarrow \int_{t_p^{\mp}}^{0} \Omega_{\text{CR3BP}} \left(t, \mathbf{x}_{\text{SOI}}^{\mp\,(i)}\right) \text{dt}$

Augment the velocity at the SOI of the delta-v component: $\mathbf{v}_{\text{SOI}}^{\mp\,(i)} \leftarrow +\Delta v^{\mp(i)}$

Integrate the trajectory till terminal points: $\mathbf{x}_{d/a}^{(i)} \leftarrow \int_{t_p^{\mp}}^{t_{d/a}^{(i)}} \Omega_{\text{CR3BP}} \left(t, \mathbf{x}_{\text{SOI}}^{\mp\,(i)}\right) \text{dt}$

Ensure:

$$\min \left(\Delta v_{\text{SOI}}^{-\,(i)} + \Delta v_{\text{SOI}}^{+\,(i)} + \left\|\mathbf{v}_d^{(i)} - \mathbf{v}_d(t_d^{(i)} + t_p^{-})\right\| + \left\|\mathbf{v}_a^{(i)} - \mathbf{v}_a(t_p^{+} + t_a^{(i)})\right\|\right)$$

subject to:

$$\mathbf{g}(\mathbf{x}): \begin{cases} \mathbf{x}_p^{-(i)} - \mathbf{x}_p^{+(i)} = 0 \\ \mathbf{r}_d^{(i)} - \mathbf{r}_d(t_d^{(i)} + t_p^{-}) = 0 \\ \mathbf{r}_a^{(i)} - \mathbf{r}_a(t_p^{+} + t_a^{(i)}) = 0 \end{cases}$$

$$\mathbf{h}(\mathbf{x}): \begin{cases} \left|t_a^{(i)} + t_p^{+} - t_p^{-} - t_d^{(i)} - T\right| - \varepsilon \leq 0 \\ R_{\text{Hill}} \geq \left\|\mathbf{r}_{\text{SOI}}^{\mp\,(i)} - \{1-\mu, 0, 0\}\right\| \leq 5R_{\text{Hill}} \\ \Delta v_{\min} - \left\|\mathbf{v}_{d/a}^{(i)} - \mathbf{v}_{d/a}(t_{d/a}^{(i)} + t_p^{\mp})\right\| \leq 0 \end{cases}$$

Nevertheless, the feasibility of the correction manoeuvres is not guaranteed considering that their executions far from the discontinuity might result in negligible delta-vs which represents another reason to initialise the optimisation from initial conditions far from secondary but not so far as the terminal points.

The optimisation strategy consists in performing the backward and forward propagation from each of the control points on the SOI. The velocity difference at terminal and control points is minimised where the continuity condition at the close approach and targeting constraints at deperarture and arrival planet are satisfied, see Algorithm 5.

It is interesting to note that, differently from the close approach strategy, the initiali-

sation at the SOI allows more room at the optimiser to identify the minimum solution, since the optimisation presents a higher degree of freedom, computed as the difference between number of independent free-variables and number of equality constraints. Moreover, the close approach condition does not appear anymore among the equality constraints, $\mathbf{g}(\mathbf{x})$ vector, as it is automatically satisfied by in the propagation within the SOI, stopped when Eq. 6.1 is satisfied.
In the CR3BP the absence of the time makes the continuity constraint enough to ensure patching at the close approach; nevertheless, a time update is required in order to ensure a correct targeting with the departure and arrival planets. In the end, the inequality constraints allow a relaxation of the total time of flight and of the definition of the SOI radius and ensure that the correction at the terminal point is not negligible. If the latter constraint results inactive the solution obtained with the SOI initialisation converges to the close approach optimisation.

6.2 Shooting algorithm for resonant flyby identification

The strength of the grid search algorithm consists in the ability to characterise a region of the phase space by representing the trend of variables of interest interpolated on the subset of points on the grid. Depending on whether the value of the output variable is displayed on the same coordinate system of the grid or on a separate one, whose variation is parametrised through a colour scale, surface and contour plots are distinguished. In this work, a piece-wise linear interpolation is performed between each pair of grid points and allows the map to extrapolate the evolution of the output variable without the need to compute it, this is based on the assumption that the variable to be represented is a result of a smooth function. Constant level curves of the output values can be also represented with an hyper-plane parallel to the grid coordinate system, whose intersections with the interpolated surface identify constant level contours. As expected, the contour precision such as the prediction quality on the output variable trend depends directly on the piece-wise linear interpolation and therefore by the grid size.

The results of the Flyby map in terms of the semi-major axis and inclination variations were displayed in Ch. 5 through bi-dimensional contour plot in terms of the argument and osculating longitude of the periapsis, that constitute the grid coordinate system. Among all the different effect of the close approach on the post-encounter trajectories, resonant flyby are interesting since, by freezing the semi-major axis, they enable repetitive encounter with the secondary mass after approximately one synodical period and offer an inexpensive way to modify eccentricity and inclination with respect to the primary. Resonant orbits can be determined in the Flyby map $\mathcal{F}$ with the contour associated to the level set, $\mathcal{L}_a$, described by Eq. 6.3:

$$\mathcal{L}_a(\mathcal{F}) = \{(\omega, \varpi) \,|\, (\omega, \varpi) \in \mathcal{D}(\mathcal{F}) \vee a_B(\omega_A, \varpi_A) = a_A\} \tag{6.3}$$

which identifies the control variables presenting a zero variation of the semi-major axes measured at the Poincaré sections, $\sum_A$ and $\sum_B$ respectively, and related to the pre- and post-encounter conditions. Although the piece-wise bi-linear interpolation in the control variable space manages to extract the resonant condition from the Flyby map domain, $\mathcal{D}(\mathcal{F})$, the sequence of points poorly satisfies Eq. 6.3. Indeed, adopting the argument and osculating longitude of the peripapsis coordinates associated to the contour as initial guess leads to several hundreds of thousands of km difference between the pre- and post-encounter semi-major axis. Adopting a finer grid search would not anyway capture the resonant condition but significantly increase the computational effort required to generate the map. Instead, even a coarse grid offers good initial guesses in the Flyby mapF control variables that can be refined through an optimisation process. Being the degree of freedom of the optimisation positive, with phase space of free-variables bi-dimensional and one constraint, the resonant condition, to be satisfied, the optimisation might fail in characterising the contour. Another constraint must be added to set up a root finding algorithm: the bi-modal behaviour displayed by the close approach distance, represented in Fig. 5.10, make it a good candidate for the parametrisation of the contour. An exponential distribution identifies all the possible level sets of the minimum flyby altitude. The advantage of implementing a close approach parametrisation is double. On one side, it allows to regulate the selection of the initial guesses, performed at the intersection of the contours associated to resonant condition and to the level sets, see Fig. 6.1:

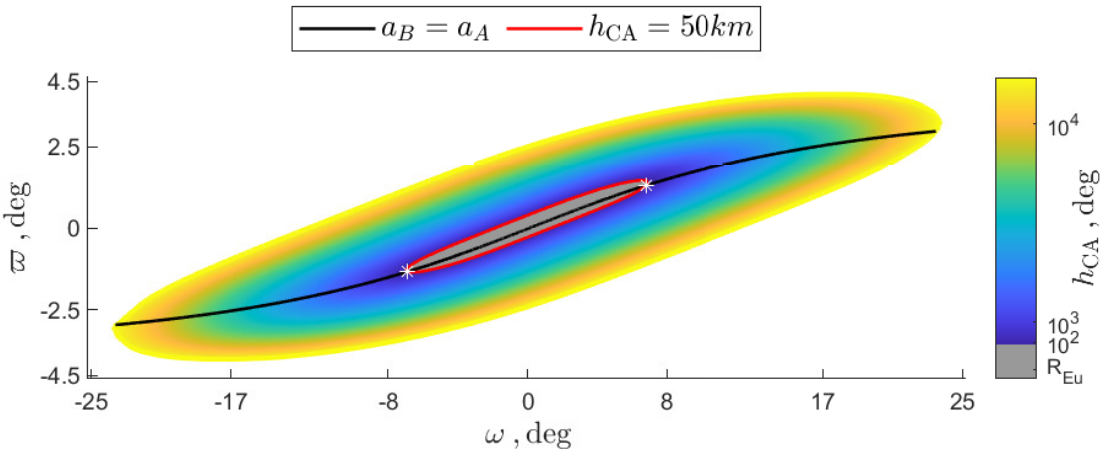

Figure 6.1: *The identification process of the initial conditions, represented with the white star markers in the control variable space, from the piece-wise bi-linear interpolated contours associated to the resonant flyby and the close approach altitude of 50 km, in black and red respectively, for a 4:1 resonant orbit at the maximum inclination and 4 km/s infinite velocity at Europa.*

while on the other, it determines the additional constraints required to initialise the root-finder, see Algorithm 6.

Algorithm 6 The refinement of the contour associated to the resonant condition parametrised on an exponential distribution of the close approach distance through a root-finding algorithm.

Require: ω_A,ϖ_A, a_B, r_p
  Generate an exponential distribution: $\mathbf{C}_{r_p} \leftarrow \text{Exp}(m) | C_{r_p} \in [\min r_p, R_{\text{Hill}}]$
  for $c_{r_p} \in \mathbf{C}_{r_p}$ **do**
    Determine the countour for the level set: $\mathcal{L}_{r_p} \leftarrow \left\{ (\omega, \varpi) \, | r_p \left(\omega_A, \varpi_A \right) = c_{r_p} \right\}$
    Determine the initial guess at the countours intersection: $\{\omega_A^{(0)}, \varpi_A^{(0)}\} \leftarrow \mathcal{L}_a \cap \mathcal{L}_{r_p}$
    Find $\omega_A^{(i)}, \varpi_A^{(i)}$ s.t.
Ensure:
    $a_B \left(\omega_A, \varpi_A \right) = a_A \vee r_p \left(\omega_A, \varpi_A \right) = c_{r_p}$
  end for

These initial guesses can be refined to machine accuracy in few iterations, generally two, solving the system of non-linear equations identified by the contour levels under study.

6.3 Psuedo-arclength continuation for families of resonant flybys identification at different inclinations

The ability to scan the phase space of the control variables and study their effect in identifying different configurations of the close approach that leads to a different post-encounter trajectories make the Flyby map an interesting tool to evaluate the flyby effect in the CR3BP . Nevertheless, anytime a parameter different from the argument and the osculating longitude of the periapsis is modified to study a diverse configuration of the flyby, a new Flyby map has to be generated. However, if a specific sequence of flybys wants to be analysed, several Flyby maps, one per each flyby modifying semi-major axis or eccentricity, might be required to be evaluated to extract from few points from their domain. It is the case of resonant flyby sequences with a prescribed close approach distance, whose implementation in the Clipper tour is fundamental to inspect different quadrants of the surface of Europa. Applying the Flyby map in cascade using the information obtained at the Poincaré section $\sum_B$ to re-initialise the numerical mapping with the arrival inclination represents a possible way to tackle the design of resonant orbits whose variation in inclination is the result of a flyby, however it is not efficient.

Instead of generating several Flyby maps and resolving different root-solving problems, a psuedo-arclength continuation method can be initialised with the refined resonant contour parametrised by the close approach distance and used to identify family of resonant orbits with prescribed close approach distance. Psuedo-arclength continuation is a numerical method that belongs to the category of predictor-corrector solvers.

Such approach originated by the observation that the tangent represents a more natural parametrisation of a curve described by Eq. 6.4 [36, 37]:

$$\mathcal{G}(\mathbf{u}) = 0 \quad \text{where} \quad \mathcal{G} : \mathbb{R}^N \times \mathbb{R} \to \mathbb{R}^N \tag{6.4}$$

in the $\mathbf{u} = \{u_1, u_2, \ldots, u_N\}$ coordinate system that in resonant flyby case can be replaced by the tern i_A, ω_A and ϖ_A, associated to the inclination, argument of the periapsis and osculating longitude of the periapsis of the pre-encounter trajectory measured at the Poincaré section Σ_A. Then Eq. 6.4 becomes:

$$\mathcal{G}\left(i_A, \omega_A, \varpi_A\right) = \begin{cases} a_B\left(i_A, \omega_A, \varpi_A\right) - a_A = 0 \\ r_p\left(i_A, \omega_A, \varpi_A\right) - c_{r_p} = 0 \end{cases} \tag{6.4}$$

where c_{r_p} constitutes a level set of the exponential distribution of close approach distances, C_{r_p}.

Let $\left(i_A^{(i)}, \omega_A^{(i)}, \varpi_A^{(i)}\right)$ be a point on the regular curve, then the tangent to the curve at the point can be determined by $\left(\dot{i}_A^{(i)}, \dot{\omega}_A^{(i)}, \dot{\varpi}_A^{(i)}\right)$ Eq. 6.5:

$$\dot{\mathbf{u}} \in \ker \mathcal{G}_{\mathbf{u}} \quad \rightarrow \quad \mathcal{G}_{\mathbf{u}}\left(\mathbf{u}^{(0)}\right) \cdot \mathbf{u} = 0 \tag{6.5}$$

that can be rewritten in the Flyby map parameters of interest:

$$\begin{bmatrix} \frac{\partial a_B}{\partial x_B}\frac{\partial x_B}{\partial x_A}\frac{\partial x_A}{\partial i_A^{(i)}} & \frac{\partial r_p}{\partial x_e}\frac{\partial x_e}{\partial x_A}\frac{\partial x_A}{\partial i_A^{(i)}} \\ \frac{\partial a_B}{\partial x_B}\frac{\partial x_B}{\partial x_A}\frac{\partial x_A}{\partial \omega_A^{(i)}} & \frac{\partial r_p}{\partial x_e}\frac{\partial x_e}{\partial x_A}\frac{\partial x_A}{\partial \omega_A^{(i)}} \\ \frac{\partial a_B}{\partial x_B}\frac{\partial x_B}{\partial x_A}\frac{\partial x_A}{\partial \varpi_A^{(i)}} & \frac{\partial r_p}{\partial x_e}\frac{\partial x_e}{\partial x_A}\frac{\partial x_A}{\partial \varpi_A^{(i)}} \end{bmatrix} \begin{bmatrix} \dot{i}_A \\ \dot{\omega}_A \\ \dot{\varpi}_A \end{bmatrix} = 0 \quad \Rightarrow \quad \begin{bmatrix} \dot{i}_A^{(i)} \\ \dot{\omega}_A^{(i)} \\ \dot{\varpi}_A^{(i)} \end{bmatrix} = \begin{bmatrix} 1 \\ \frac{g_{13}g_{21} - g_{11}g_{23}}{g_{12}g_{23} - g_{13}g_{22}} \\ \frac{g_{11}g_{22} - g_{12}g_{21}}{g_{12}g_{23} - g_{13}g_{22}} \end{bmatrix} \tag{6.5}$$

It is interesting to note that the Jacobian of the curve defined by Eq. 6.4, accounting for the partial derivative of the minimum flyby altitude and the post-encounter semi-major axis can be expressed by the chain rule as the product of the partial derivative of the initial cartesian state with respect of to the orbital parameters evaluated at the initial point, the state transistion matrix and the partial derivatives of the curve variables with respect to the cartesian state of reference, that are identified during the propagation by the event functions defined by Eq. 6.1 and Eq. 7.2 respectively. Moreover, differently from what the theory suggests, the tangent $\dot{\mathbf{u}}$ can be normalised with respect to one variable, in this case the inclination i_A that constitutes the out-of-plane component with respect to the control variables space of the Flyby map. Therefore, the predictor, $\widetilde{\mathbf{u}}^{(i+1)}$, can be defined through a step, Δs, made in the tangential direction, $\dot{\mathbf{u}}^{(i)}$, from the initial point $\mathbf{u}^{(i)}$. The feasible point that satisfies Eq. 6.4 is searched by the corrector, $\mathbf{u}^{(i+1)}$,

in the normal direction to the tangent, see Eq. 6.6:

$$\begin{aligned} \widetilde{\mathbf{u}}^{(i+1)} &= \mathbf{u}^{(i)} + \dot{\mathbf{u}}^{(i)} \Delta s \\ \mathbf{u}^{(i+1)} : & \begin{cases} \mathcal{G}\left(\mathbf{u}^{(i+1)}\right) = 0 \\ \left(\mathbf{u}^{(i+1)} - \widetilde{\mathbf{u}}^{(i+1)}\right) \cdot \dot{\mathbf{u}} = 0 \end{cases} \end{aligned} \tag{6.6}$$

If the step, Δs is small enough, the psuedo arclength continuation can easily pass through fold and bifurcation points differently from the Newton method, based on natural parameter continuation [37].

CHAPTER 7

Application: the Europa Clipper mission

Europa Clipper is a NASA scientific mission to study Europa and answer the question about its potential sustainability of existing life. The presence of liquid water, heat source and different chemical elements place Europa in the top priority list for NASA planetary exploration program.

The Europa Clipper's trajectory is a multi-moon orbiter mission accounting over 45 Europa, 5 Ganimede and 9 Callisto flybys answering to several design challenges: high resolution distributed observations of the surface of Europa under different luminosity conditions, high datalink and low radiation dose exposure, which constitutes a critical point considering that Europa resides deep inside Jupiter magnetosphere.

The trajectory exploits the gravitational interaction of the Galilean moons with Jupiter's gravity field, yet its design is still based on a patched conics modelling of such effects [12, 13, 43, 44]. Nevertheless, planetary moon systems, such as the Jupiter one, exhibits strong perturbations that induce large errors in position and velocity on the two-body trajectory. Such discrepancies result in large delta-v and therefore in poor convergence when the orbit is refined in the full-model, which considers the dynamics of the six-body problem represented by Jupiter and the Galilean moon system together with the perturbation induced by the Sun and Jupiter J_2 effect. Patched conics legs might disappear or require delta-v so high to invalidate the whole sequence. It is clear

that developing a methodology that could provide good initial guesses is needed. Therefore, the goal of this chapter is to show the applicability of the Flyby map to construct the Clipper's tour taking advantage of a renewed understanding about the chaotic dynamics, induced already by the circular restricted three-body problem. A trajectory with two consecutive resonant flybys at 50 km altitude, similar to those implemented in the Clipper Crank-Over-Top (COT) sequence [12, 13, 43, 44], is investigated and is explained in the following chapter.

7.1 Crank-Over-Top sequence design with the flyby map

The COTs(Crank-over-the-top sequences) are a series of resonant flybys whose purpose consists in distributing observations of Europa's surface at different latitudes. The name derives from the patched conics design, in which the change of inclination induced by the flyby can be modeled by the crank angle, see Fig. 5.4. Starting from an equatorial orbit, several close encounters with Europa allows to cover 180 degrees in crank angle. From the trajectory perspective, the S/C hops through different resonant orbits, that are assumed to share the same semi-major axis, and therefore the pump angle, see Eq. 5.9, and experience an initial increment in the inclination followed by a subsequent reduction of this inclination [13, 17]. In a patched conics perspective, moving in one direction of the crank angle rather than another from a given initial condition is interchangeable since targeting a prograde or retrograde flyby is equivalent far from the secondary body. Moreover it is always possible to return to the initial point performing a flyby in the opposite crank direction with respect to the incoming one at the arrival. However, several tours [12, 43, 44] display a predominant direction with a positive change in crank angle for the resonant flyby sequence. Considering the different effect displayed by prograde and retrograde in the CR3BP , captured by the Flyby map in chapter 4, it is interesting to observe whether the flyby effect in the CR3BP leads to conclusions similar to those extrapolated by the tours analysis. The dynamics of the CR3BP prevents from analysing the out-of-plane effect of equatorial flyby, indeed a state that lies on the orbital plane of Europa will remain bounded to it. Therefore, instead studying the COTs from its departure condition, the analysis starts from a resonant orbit at the maximum admissible inclination derived by patched conics [18] and aims to use the Flyby map to identify the natural continuation in crank angle.

7.1.1 Identification of naturally connected resonant orbits

In the previous chapter, a method to derive the exact resonant flyby from the interpolated contour solution was presented and consisted in exploiting the knowledge of the close approach to identify the initial guess and fine-tune it through a root-finder. In or-

der to build a COTs with a reference close approach distance, the Flyby map is applied in cascade re-initialising the numerical mapping at the arrival inclination obtained at the Poincaré section Σ_B, see Fig. 7.1.

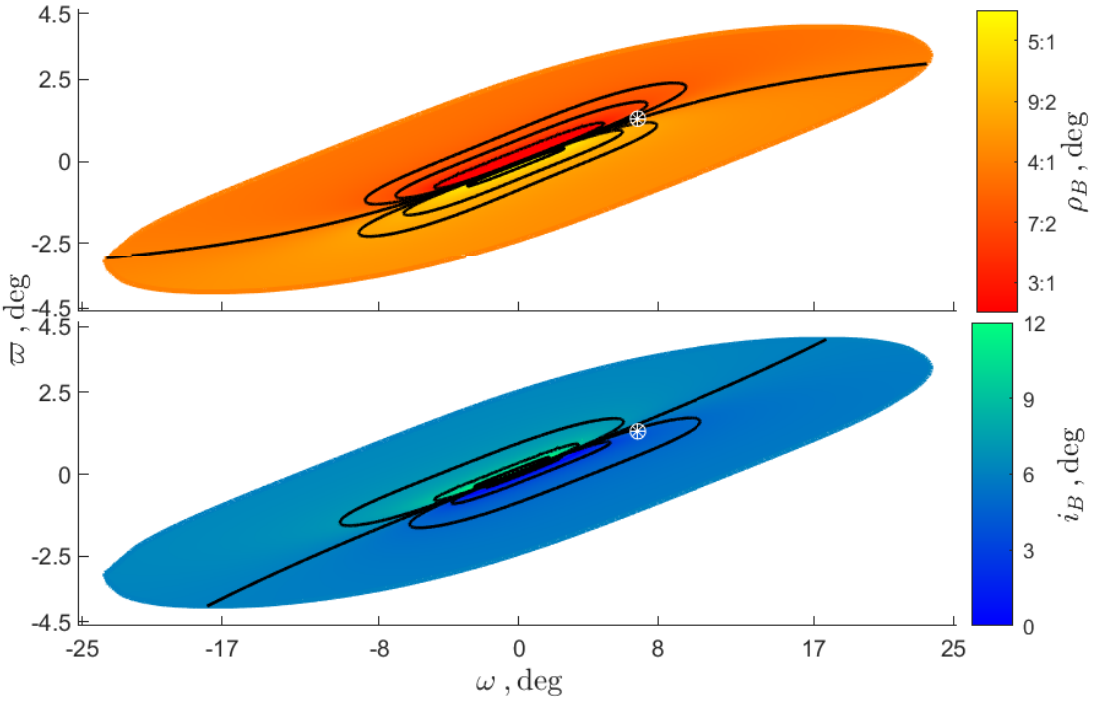

Figure 7.1: *The characteristic information resulting from perturbing the osculating longitude and the argument of the periapsis for a 4:1 resonant orbit at the maximum inclination, 6.006 degrees, with 4 km/s infinite velocity. From the top to the bottom, the colour-coded distributions of the period and the inclination of the post-encounter osculating orbit and the refined solution for a 50 km altitude resonant flyby represented with the white star marker.*

The Tisserand parameter is conserved by the dynamics and the semi-major axis is preserved by the resonant flyby. At the Poincaré section $\Sigma_B^{(i+1)}$, an additional refinement process is required to identify the solutions presenting 50 km altitude resonant flyby. Fig. 7.2 displays the trend of the post-encounter semi-major axis and inclination with respect to the control variables, the argument and the osculanting longitude of the periaspsis.

The refined solutions for the second flyby, represented with the white star markers in Fig. 7.2, must be compared at the patching point with the one generated by the first flyby, see Fig. 7.1. The deviations at the patching point, expressed in terms of miss-distance and delta-v difference, which are collected in Tab. 7.1, show that the natural continuation of the first resonant flyby is the fourth solution, identified by the white starred circle in Fig. 7.2, characterised by an error of more than 16 thousand km in position and of more than 30 m/s in velocity.

Table 7.1: *The identification of the "natural" resonant orbit obtaining comparing the results at the patching.*

x	at $\Sigma_B^{(0)}$	at $\Sigma_A^{(1)}$			
r_x [10^6 km]	-2.7118	-2.7125	-2.7140	-2.7141	-2.7126
r_y [10^6 km]	-0.1383	0.1239	0.0947	-0.0913	-0.1221
r_z [10^6 km]	-0.0486	0.0487	0.0283	-0.0285	-0.0486
v_x [km/s]	-2.6120	2.3360	1.7863	-1.7214	-2.3017
v_y [km/s]	51.2541	51.2674	51.2959	51.2980	51.2690
v_z [km/s]	-0.3135	-0.3134	-0.3196	-0.3195	-0.3134

x	Δx			
r_x [10^6 km]	-0.0007	-0.0022	-0.0023	-0.0001
r_y [10^6 km]	0.2622	0.2.3303	0.0471	0.0163
r_z [10^6 km]	0.0973	0.0769	0.0201	0.0000
v_x [km/s]	4.9480	4.3984	0.8907	0.3104
v_y [km/s]	0.0133	0.0418	0.0439	0.0149
v_z [km/s]	0.0001	-0.0061	-0.0060	0.0001

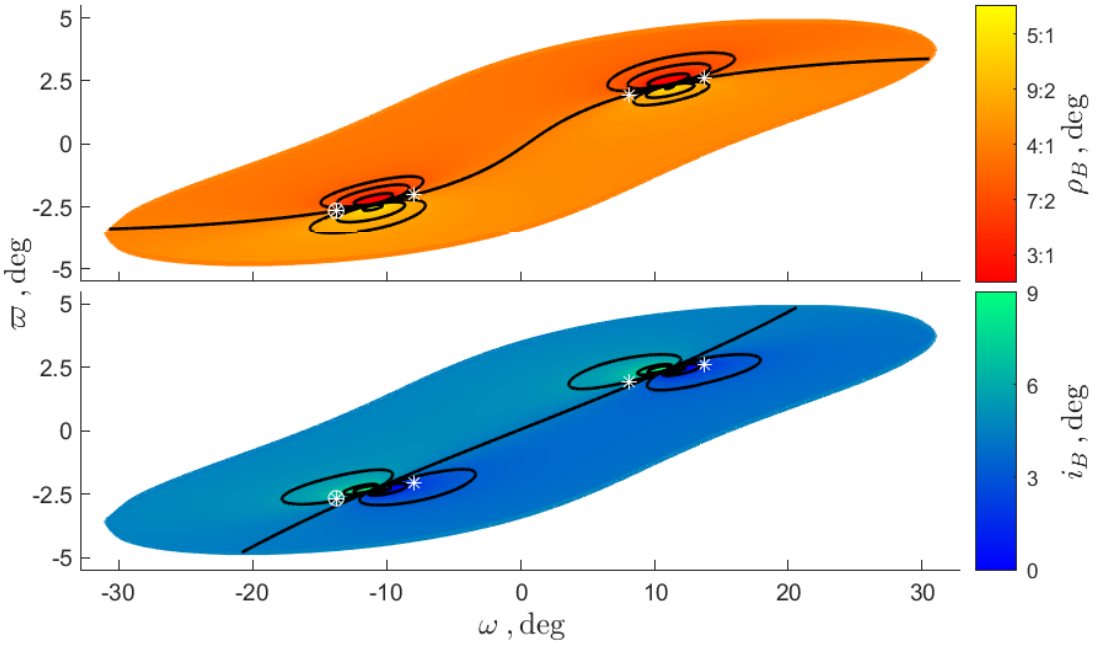

Figure 7.2: *The characteristic information resulting from perturbing the osculating longitude and the argument of the periapsis for a 4:1 resonant orbit at 4.316 degrees of inclination with 4 km/s infinite velocity. From the top to the bottom, the colour-coded distributions of the period and the inclination of the post-encounter osculating orbit and the refined solution for a 50 km altitude resonant flyby represented with the white star markers.*

Such discrepancies in miss-distance and delta-v arise by the approximation of studying at the Poincaré section an orbit subjected to the three-body dynamics with quantities belonging to a different dynamical model, such as the semi-major axis and the inclina-

tion for instance.

7.2 Crank-Over-Top sequence optimisation

In the previous section, the selection of the natural resonant orbit from the initial one was performed. Nevertheless, even if such trajectory presents the smallest errors in position and velocity at the patching points, such discrepancies are too large. Consider, for instance, that for the whole tour Clippers has a total delta-v on the order of 100-200 m/s for a number of flybys ranging from between 50-60, accounting for no more than 5 m/s of delta-v per flyby [12, 43]. An optimisation process is required to reduce the deviations within acceptable margins, minimising the velocity difference at the patching point while preserving the overall features of the orbit, expressed in initial and final semi-major axes and inclinations.

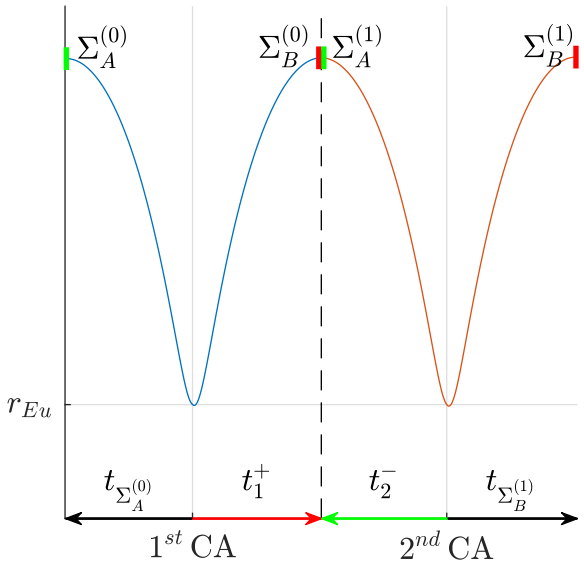

Figure 7.3: *The representation of Poincare sections, Σ_A and Σ_B, along the orbit identifying the boundary conditions of propagation.*

7.2.1 Problem statement

A refined version of the close approach optimisation described in chapter 6 is exploited. Initialised the optimisation with the state at the close approaches, the trajectory is propagated backward and forward in time until crossing with the Poincaré sections, Σ_A and Σ_B at which the constraints and the objective function are evaluated, following the schematic presented in Fig. 7.3.

Let χ be the free-variable vector expressed as:

$$\chi = \left(\mathbf{x}_1^{\mathrm{CA}}, t_1^+, \mathbf{x}_2^{\mathrm{CA}}, t_2^-\right) \tag{7.1}$$

where $\mathbf{x}^{\mathrm{CA}}$ denotes the state at the close approaches, t the time of flight till the patching point and the apex $+/-$ indicates whether the propagation occurs forward or backward respectively. Then, the optimisation problem can be stated as a minimisation of the delta-v at the gap:

$$\mathbf{J} \quad \min \mathbf{v}_2^- - \mathbf{v}_1^+$$

subject to the following equality constraints:

C1 $a_A^{(0)} = a_{ref}$ and $a_B^{(1)} = a_{ref}$
preserve the resonance condition at $\Sigma_A^{(0)}$ and $\Sigma_B^{(1)}$;

C2 $i_A^{(0)} = i_{ref}^{(0)}$ and $i_B^{(1)} = i_{ref}^{(1)}$
maintain inclination variation along the orbit checking the initial and final inclination at $\Sigma_A^{(0)}$ and $\Sigma_B^{(1)}$;

C3 $\mathbf{r}_2^- = \mathbf{r}_1^+$
reduces the miss-match within $(1m)$ tolerance;

C4 $\mathbf{r}_{\mathrm{p}} - R_{Eu} = 50km$ and Eq. 6.1
ensuring that the propagation starts from a close approach at 50 km of altitude.

As it is, the optimisation might get stuck generating unfeasible initial conditions, therefore, the problem is reformulated by incorporating **C4** in the free-variables, converting the Cartesian state at the close approach $\mathbf{x}^p$ into spherical coordinates. The result of embedding the constraints reduce the state vector at the close approach $\mathbf{x}_p$ to $\mathbf{s} = (\lambda, \phi, \mathrm{v}, \beta)$ expressed in terms of the longitude, λ, and the latitude, ϕ, of the pericentre and the magnitude, v and the orientation β of the velocity, measured from the north direction in the plane normal to the position vector.
Such form is particularly convenient as it prevents the optimisation from generating states that lead to a collision and trajectories that are captured at the secondary body, condition that can be obtained by bounding to the velocity v

Finally, in order to further improve the optimisation performances, the Jacobian of the objective function **J** and the constraints, **C1**, **C2** and **C3**, are computed applying the chain rule, as:

$$\frac{\partial J}{\partial \chi} = \begin{bmatrix} \frac{\partial \Delta v}{\partial s} & \frac{\partial \Delta v}{\partial t} \end{bmatrix} = \begin{bmatrix} \frac{\partial \Delta v}{\partial x_f}\frac{\partial x_f}{\partial x_i}\frac{\partial x_i}{\partial s} & \frac{\partial \Delta v}{\partial x_f}\frac{\partial x_f}{\partial t} \end{bmatrix}$$
$$\frac{\partial C}{\partial \chi} = \begin{bmatrix} \frac{\partial C1}{\partial s} & \frac{\partial C1}{\partial t} \\ \frac{\partial C2}{\partial s} & \frac{\partial C2}{\partial t} \\ \frac{\partial C3}{\partial s} & \frac{\partial C3}{\partial t} \end{bmatrix} = \begin{bmatrix} \frac{\partial a}{\partial x_\Sigma}\frac{\partial x_\Sigma}{\partial x_i}\frac{\partial x_i}{\partial s} & 0 \\ \frac{\partial i}{\partial x_\Sigma}\frac{\partial x_\Sigma}{\partial x_i}\frac{\partial x_i}{\partial s} & 0 \\ \mathcal{I}_3\frac{\partial x_f}{\partial x_i}\frac{\partial x_i}{\partial s} & \mathcal{I}_3\frac{\partial x_f}{\partial t} \end{bmatrix} \tag{7.2}$$

where x_Σ, x_f and x_i are associated to the Cartesian state at the Poincaré section, at the final and initial point respectively. Note that Eq. 7.2 does not represent the actual Jacobian which is computed for the full free-variable vector χ shown in Eq. 7.1 and for the complete set of the **C1** and **C2** constraints, but want to be representative of the reasoning that was applied. As a final remark, providing the Jacobian allows to prevent the optimisation from approximating inaccurately the partial deviates computed, otherwise, by the optimiser with finite difference. Such condition is more prone to occur above all the points that are extrapolated during the propagation through event functions, for instance at the crossing of the Poincaré section.

Resonant flyby optimisation

In the previous section, the direct optimisation of two resonant flybys of Europa Clipper COTs sequence is addressed in terms of initialisation and methodology. In this section, we evaluate the result of the optimiser.

First of all, it is interesting to evaluate the difference between the initial and optimal design variables in order to understand how close or far the initial conditions were from the optimal solution. Tab. 7.2 and Tab. 7.3 gather the values of the initial and optimal state and their difference, in terms of the optimisation parameters and the associated state at the close approach. This demonstrates that the difference is of few km (12.749 km and 1.967 km) and few m/s (17.879 and 5.368 m/s) for the position and velocity of the first and second close approaches respectively, and of few min (around a quarter of hour) for the time of flight at the patching point. This information tells that the Flyby map offers initial conditions that are reasonably close to the optimal ones.

At the same time such a small change on the initial conditions has a huge impact on the delta-v and the miss-distance, that improve from 32.99 to 1.47 m/s and from 1750 km to 2.16 cm, as you can see from Tab. 7.4.

Table 7.2: *The difference between the initial and optimal free-variables.*

	χ_0		χ		$\Delta\chi$	
	$1^{st}CA$	$2^{nd}CA$	$1^{st}CA$	$2^{nd}CA$	$1^{st}CA$	$2^{nd}CA$
λ [deg]	-0.9159	-2.3665	-0.9022	-2.3585	0.0137	0.0080
ϕ [deg]	35.6957	62.3576	35.2423	62.2878	-0.4533	-0.0699
v [m/s]	4.4633	4.4631	4.4609	4.4616	-0.0024	-0.0014
β [deg]	-61.1803	-60.4954	-61.2796	-60.5610	-0.0992	-0.0656
t [d h:m:s]	07 04:46:00.58	-07 00:12:49.66	07 04:29:55.40	-07 00:28:26.36	-00:16:05.17	-00:15:36.70

Table 7.3: *The difference between the initial and optimal free-variable in terms of the state at the close approach.*

	χ_0		χ		$\Delta\chi$	
	$1^{st}CA$	$2^{nd}CA$	$1^{st}CA$	$2^{nd}CA$	$1^{st}CA$	$2^{nd}CA$
$r_x - 1 + \mu$ [km]	1.308E+03	7.467E+02	1.315E+03	7.484E+02	7.400E+00	1.742E+00
r_y [km]	-2.091E+01	-3.086E+01	-2.071E+01	-3.083E+01	1.969E-01	3.209E-02
r_z [km]	9.399E+02	1.427E+03	9.295E+02	1.426E+03	-1.038E+01	-9.123E-01
v_x [km/s]	-1.193E+00	-1.785E+00	-1.175E+00	-1.780E+00	1.752E-02	5.314E-03
v_y [km/s]	3.930E+00	3.961E+00	3.931E+00	3.962E+00	1.044E-03	7.651E-04
v_z [km/s]	1.747E+00	1.020E+00	1.751E+00	1.020E+00	3.404E-03	-2.818E-05

Table 7.4: *The values of the objective and constraint functions derived for the initial and optimal condition.*

	χ_0	χ
J [m/s]	3.299E+01	1.472E+00
C1 [km]	-1.977E-05	7.188E-06
	-2.477E-05	-1.247E-06
C2 [deg]	-6.468E-10	-3.220E-10
	-9.207E-11	6.117E-11
C3 [km]	-8.061E+01	2.122E-05
	1.745E+03	3.775E-06
	9.163E+01	2.159E-08

CHAPTER 8

Conclusion

In this report we present an overview of the graphical grid-search methods through which trajectories with flybys can be designed and the effect of a close passage can be studied. The main and most general result achieved during this doctoral research consists in the fact that a map alone is generally not enough to explain the behaviour of the dynamics for the solution space under consideration. Indeed the trend of the performance index at stake conceals information that can be enlightened only by additional parameters. The improved understanding of the dynamics can positively affect the trajectory design by constraining the solution space to a smaller region of interest.

In Ch. 2, the porkchop plot has been analysed for the zero- and multi-revolutions transfer between circular coplanar orbits. Purely geometrical relations, that can be expressed by analytical equations, enable the identification of the minimum delta-v solutions and the analysis of the shape of constant delta-v contours through the solutions associated to tangential manoeuvres at departure/arrival. The extension to the multi-revolutions trajectories allows to populate the porkchop plot with new minima and to evaluate different configurations for the mission scenario in terms of number of revolutions and launch opportunities for departure and arrival dates considered.

The main limitation of this study is represented by the circular coplanar hypothesis for the planets orbits. Its application is legitimated by the sake of a clear understanding

about the effect of the the time of flight and the phasing on the delta-v, situation that requires to favour a smooth constant delta-v contour over the real jagged one. Nevertheless, future work will address the effect of eccentricity and inclination on the minimum delta-v solutions and the shape of constant delta-v contours, try to separate their contributions.

Ch. 3 moves from the targeting problem for the doublets described in Ch. 2 to the triplets. In particular, we present a method to treat the flyby trajectory as two separate targeting problems whose solutions can be recombined at the common date of flyby. The approach prevents the computational effort to grow cubically. Following the reduction in dimensionality of the search space for the triplets, the targeting problem is revisited and tackled as an inverse Lambert's problem, parametrising the trajectory on the orbital elements and resolving for the time of flight. Indeed an orbital element search space can be effectively reduced with respect to its counterpart defined in epochs, and offers to the designer a direct feeling of the orbital geometries at stake. The applicability of the method to the design of flyby trajectories is enabled by different constraints formulated on the orbital elements that address the quality of flyby trajectory. The feasibility of the close encounter is checked by limits on the maximum variation of the orbital elements derived by the Gauss' Planetary Equations applied to the case of the flyby.

The drawback of the method consists in the tangentiality constraint imposed at the terminal points that simplifies significantly the parametrisation of planar trajectories as a function of the eccentricity only. Despite legitimated as suboptimality conditions, the tangentiality constraint reduce the solution space to points and in future work will be abandoned in favour of a more general treatment of the triplets in the flavour of inverse Lambert's problem.

In Ch. 4 the pruning of the search space of both doublets and triplets is addressed. A method to construct bounding region for the terminal points, at which the delta-v is evaluated, is presented and consists in identifying on the porkchop plot the tangential solutions at departure/arrival with prescribed delta-v. These points constitute the vertices of the box that can be refined to match the actual contour of the constant delta-v solutions through a simple root-finding. The limits in orbital elements variation derived in Ch. 3 are used as incremental pruning of the solution space of the post-encounter transfer leg based on the knowledge of the pre-encounter one.

The main advantage of the method consists in the possibility to define the bounding region on a different subset of the search space that presents an analytical solution for the delta-v. The price paid by the refinement is paid back by the capability to refine the bounding box derived for circular coplanar orbits on the actual constant delta-v contour

line associated to either simplified or real ephemerides and by the possibility to specify the grid-size on a reduced solution space. Future work will question the actual gain in computational time.

In Ch. 5, the spatial Flyby map is derived from the planar one and allows to obtain new insights on the third-body interaction for the 3D dynamics. In particular, two families of flyby have been observed: type I and type II, also known as prograde and retrograde. Differently from the predictions of patched conics their effect is not identical and type II flyby appears less efficient compared to type I.

Future works foresees the application of the spatial flyby map to low-energy trajectories and to a treatment of the elliptic three-body dynamics to improve the knowledge of close encounters with Europa.

Ch. 6 offers an overview of the refinement techniques that can be used to improve the accuracy of grid solutions. The first paragraph deals with the optimisation of the flyby from initial guess derived at the close approach or at the SOI. Although the first strategy is legitimated by the interest in improving the convergence of the optimisation breaking the insensitivity of the flyby from a condition at infinite, the second does not show these symptoms, converges to the solution of the first strategy when initialised with the same problem and appears ideal to treat different scenarios in an operational perspective. The second paragraph offers a root-finding approach to extract resonant flyby by the attainable set of the Flyby map and a psuedo-archlength continuation method to continue in inclination the refined solutions associated to a resonant flyby with prescribed close approach distance.

In future, the continuation method will be applied to characterise the whole family of resonant flyby along the inclination.

Ch. 7 concludes the doctoral research with an application of the Flyby map to improve the design of COTs for Europa Clipper. In particular, differently from what patched conics theorizes, Ch. 7 proves the existence of a natural direction in crank angle (forward) for the sequence of resonant flyby and the fact that "back-cranking" does not allow to return to the initial condition of departure. In the end, the Flyby map demonstrate its capability to generate good initial guesses despite obtained through an interpolation process.

Future work foresees the optimisation of a complete sequence of resonant flyby to answer about the existence of a manifold in CR3BP to which the COTs belongs.

Appendix

8.1 Appendix A: The coordinate chart, φ

At the crossing with the Poincaré section, the transformation φ allows to switch from a description of the particle's motion in the CRTBP to the coordinate system of the Flyby parameters, and vice versa through φ^T. The first/last step consists into moving from the CRTBP to the system of reference of the two-body problem.

$$\{t, X, Y, Z, \dot{X}, \dot{Y}, \dot{Z}\} \xrightarrow{3B \to 2B} \{X + \mu, Y, Z, \dot{X} - Y, \dot{Y} + X + \mu, \dot{Z}\} \tag{8.1}$$

Eq. 8.1 shows the change of origin from the barycentre of system to the location of the primary $(-\mu, 0)$ and the increase in velocity of its tangential component due to the switch from a co-rotating frame to an inertial one in which the osculating Flyby map parameters can be computed. The time of flight of the propagation, which is initialised at the close approach, must be considered to take into account the movement of the secondary during the time of flight that the particle spends travelling from the close encounter to the position of the Poincaré section.

$$\mathbf{r} = \mathcal{R}_3(t - f) \begin{bmatrix} X + \mu \\ Y \\ Z \end{bmatrix} \qquad \mathbf{v} = \mathcal{R}_3(t) \begin{bmatrix} \dot{X} - Y \\ \dot{Y} + X + \mu \\ \dot{Z} \end{bmatrix} \tag{8.2}$$

The possibility to use the time an angle in Eq. 8.2 is ensured by the non-dimensionalisation of the state and the dynamics in the CR3BP.

Direct transformation $\{t, X, Y, Z, \dot{X}, \dot{Y}, \dot{Z}\} \xrightarrow{\varphi} \{a, T, i, \varpi, \omega, f\}$

Starting from the Cartesian state derived for the two-problem from the barycentric co-rotating solutions of the CR3BP, the direct transformation calculates the osculating Flyby map parameters. In particular:

1. the semi-major axis, a, is computed directly from the vis-viva equation, see Eq. 8.3:
$$a = \left(\frac{2}{r} - v^2\right)^{-1} \tag{8.3}$$

2. the inclination, i, is derived by the angular momentum $\mathbf{h}$, see Eq. 8.4:
$$\mathbf{h} = \mathbf{r} \times \mathbf{v} \quad i = \cos^{-1} \mathbf{h} \cdot \mathbf{z} \tag{8.4}$$

3. the eccentricity vector, $\mathbf{e}$, in Eq. 8.5, allows to determine the Tisserand parameter, T, see Eq. 8.6:
$$\mathbf{e} = (v^2 - \frac{1}{r})\mathbf{r} - \mathbf{r} \cdot \mathbf{v}\mathbf{v} \tag{8.5}$$
$$T = \frac{1}{a} + 2\sqrt{(}a(1 - e.^2))\cos i) \tag{8.6}$$

4. the line of nodes, $mathbfn$, enables the derivation of the argument and osculating longitude of the periapsis, ω and ϖ, see Eq. 8.7:
$$\mathbf{n} = \mathbf{h} \times \mathbf{z} \quad \begin{cases} \omega = \cos^{-1} \mathbf{n} \cdot \mathbf{e} \\ \varpi = \cos^{-1} \mathbf{n} \cdot \mathbf{x} + \omega - t \end{cases} \tag{8.7}$$

5. and the true anomaly is conventionally defined by Eq. 8.8:
$$f = \cos^{-} 1(\mathbf{e} \cdot \mathbf{r}) \tag{8.8}$$

The osculating longitude of the periapsis must be reduced of the time of flight component since its value must be evaluated from the position of the secondary at the close approach position and therefore $t - f$ degree in advance.

Inverse transformation $\{a, T, i, \varpi, \omega, f\} \xrightarrow{\varphi^{-1}} \{X, Y, Z, \dot{X}, \dot{Y}, \dot{Z}\}$

The inverse transformation allows to initialise the propagation from the reference apsis (either the apoapsis or the periapsis depending whether the non-dimensionalised semi-major axis is greater or smaller than one), by converting the osculating Flyby map parameters into Cartesian states. In particular:

1. the velocity magnitude, v, in polar coordinates is computed directly from the semi-latus rectum, p [6], see Eq. 8.10:

$$p = \left(\frac{T - \frac{1}{a}}{2\cos i}\right)^2 \qquad (8.9) \quad \Rightarrow \qquad v = \sqrt{\frac{1}{p}} \qquad (8.10)$$

2. the distance of the positon vector, r, can be determined by the famous orbit equation, knowing the semi-latus rectum, see Eq. 8.11:

$$r = \frac{p}{1+e\cos f} \quad \text{with} \quad e = \sqrt{1 - \frac{p}{a}} \qquad (8.11)$$

3. the position and velocity vector can be derived in the peri-focal frame defined by the tern $\{\mathbf{i}_e, \mathbf{i}_p, \mathbf{i}_h\}$ directed along the eccenticity, peri-focal and angular momentum vectors respectively, see Eq. 8.12:

$$\mathbf{r}^T = r\,[\cos f, \sin f, 0] \quad \mathbf{v}^T = v\,[-\sin f, \cos f + e, 0] \qquad (8.12)$$

4. and rotated into the inertial Cartesian frame centered in primary applying the rotation, $\mathcal{R}$, described by Eq. 8.13:

$$\mathcal{R} = \mathcal{R}_3\,(\omega - \varpi - t)\,\mathcal{R}_1\,(-i)\,\mathcal{R}_3\,(-\omega) \qquad (8.13)$$

as a 3-1-3 sequence of rotations with respect to argument of the periapsis, ω, the inclination, i, and the right ascension of the ascending node expressed in terms of the osculating longitude of the periapsis, ϖ, and the time of flight at the close approach, Δt in Eq. 8.14:

$$\begin{aligned} E_{/p} &= 2\tan^{-1}\left(\frac{1-e}{1+e}\tan\frac{f_{/p}}{2}\right) \\ \Delta M &= E_p - E - e\,(\sin E_p - \sin E) \\ t &= \sqrt{a^3}\Delta M \end{aligned} \qquad (8.14)$$

measured with Kepler equation from the reference apsis, f, to the true anomaly of the encounter, f_p. This quantity results from imposing that the orbit associated to the Flyby map parameter intercepts the secondary in a patched conics perspective. In the case of high energy flybys, it can be derived from Eq. 8.11 imposing that r equals the orbital distance of the secondary from the primary. Eq. 8.14 ensures, on one side, that the fictituos close encounter occurs at the position of the secondary and at 0 instant. The term fictituos indicates the patched conics assumption that confuses the location of the close encounter with the position of the secondary which represents limiting case of the zero flyby distance.

8.2 Appendix B: The symmetries of the Flyby map

The Flyby map, $\mathcal{F}$, is the result of three sequential operations, $\varphi \circ f(t) \circ \varphi^{-1}$ that enable mapping the Flyby parameters evolution subjected to the CR3BP dynamics, with $f(t)$ describing the flow from the Poincaré sections $Sigma_A$ to $Sigma_B$. It is interesting to note that the symmetries of the dynamical model, described by Eq. 8.15, Eq. 8.16 and Eq. 8.17 [71] :

$$\{x, y, z, \dot{x}, \dot{y}, \dot{z}, t\} \xrightarrow{S_1} \{-x, y, z, \dot{x}, -\dot{y}, -\dot{z}, -t\} \tag{8.15}$$

$$\{x, y, z, \dot{x}, \dot{y}, \dot{z}, t\} \xrightarrow{S_2} \{x, -y, z, -\dot{x}, \dot{y}, -\dot{z}, -t\} \tag{8.16}$$

$$\{x, y, z, \dot{x}, \dot{y}, \dot{z}, t\} \xrightarrow{S_3} \{x, y, -z, \dot{x}, \dot{y}, -\dot{z}, t\} \tag{8.17}$$

are preserved by the Flyby map limited to the transformation φ, that translates these relations expressed in the Cartesian state into Flyby map parameters identifying properties of the mapping that can be exploited to reduce the computational effort required to scan the solution space. In particular, the symmetry about the orbital plane, in Eq. 8.17, can be translated the inverse transformation into Eq. 8.18:

$$(a, T, i, \varpi, \omega) = \varphi(x, y, z, \dot{x}, \dot{y}, \dot{z}, t) \Longleftrightarrow \varphi(x, y, -z, \dot{x}, \dot{y}, -\dot{z}, t) = (a, T, i, \varpi, \omega + \pi) \tag{8.18}$$

which allows to reduce the study of the flyby effect to half of the domain of the argument of the periapsis ω.

The combination of S_2 and S_3 resulting in the time symmetry S_6, in Eq. 8.19:

$$\{x, y, z, \dot{x}, \dot{y}, \dot{z}, t\} \xrightarrow{S_3} \{x, -y, -z, -\dot{x}, \dot{y}, \dot{z}, -t\} \tag{8.19}$$

permits to derive the inverse map $\mathcal{F}^{-1}$ from $\mathcal{F}$ by changing the sign of the control variables, ϖ and ω. Indeed, with F^{-1} defined as:

$$(a, T, i, \varpi, \omega)_A = \mathcal{F}^{-1} (a, T, i, \varpi, \omega)_B$$

and existing the equivalence:

$$(a, T, i, -\varpi, -\omega)_A = \mathcal{F} (a, T, i, -\varpi, -\omega)_B$$

then the inverse transformation can be described by Eq. 8.20:

$$\mathcal{F}^{-1} = \Theta \circ \mathcal{F} \circ \Theta \quad \text{where} \quad \Theta(a, T, i, \varpi, \omega) = (a, T, i, -\varpi, -\omega) \tag{8.20}$$

Bibliography

[1] Fernando Abilleira. Broken-plane maneuver applications for earth to mars trajectories. 2007.

[2] Elisa Maria Alessi and Joan Pau Sánchez. Semi-Analytical Approach for Distant Encounters in the Spatial Circular Restricted Three-Body Problem. *Journal of Guidance, Control, and Dynamics*, 39(2):351–359, 2015.

[3] Roberto Armellin, Pierluigi Di Lizia, Francesco Topputo, Michele Lavagna, Franco Bernelli-Zazzera, and Martin Berz. Gravity assist space pruning based on differential algebra. *Celestial mechanics and dynamical astronomy*, 106(1):1, 2010.

[4] Giulio Avanzini. A simple lambert algorithm. *Journal of guidance, control, and dynamics*, 31(6):1587–1594, 2008.

[5] Martin Avendano and Daniele Mortari. A closed-form solution to the minimum ${\Delta V_{\rm tot}}^2$ lambert's problem. *Celestial Mechanics and Dynamical Astronomy*, 106(1):25, 2010.

[6] Richard H Battin. *An introduction to the mathematics and methods of astrodynamics*. AIAA, 1999.

[7] VM Becerra, DR Myatt, SJ Nasuto, JM Bishop, and D Izzo. An efficient pruning technique for the global optimisation of multiple gravity assist trajectories. *Acta Futura*, 2005:35, 2003.

[8] Julia L Bell and Jennie R Johannesen. Galileo europa mission (gem) tour design. 1997.

[9] Christian Blum, Andrea Roli, and Michael Sampels. *Hybrid metaheuristics: an emerging approach to optimization*, volume 114. Springer, 2008.

[10] Claudio Bombardelli, Juan Luis Gonzalo, and Javier Roa. Approximate analytical solution of the multiple revolution lambert's targeting problem. *Journal of Guidance, Control, and Dynamics*, 41(3):792–801, 2018.

[11] Dylan R Boone, Sumita Nandi, Julie Kangas, and Brian Young. Orbit determination sensitivity analysis for the europa multiple flyby mission concept. In *AIAA/AAS Astrodynamics Specialist Conference*, page 5429, 2016.

[12] Brent Buffington. Trajectory design concept for the proposed europa clipper mission. In *AIAA/AAS Astrodynamics Specialist Conference*, page 4105, 2014.

[13] Brent Buffington, Stefano Campagnola, and Anastassios Petropoulos. Europa multiple-flyby trajectory design. In *AIAA/AAS Astrodynamics Specialist Conference*, page 5069, 2012.

[14] Brent Buffington, Tray Lam, Stefano Campagnola, J Ludwinski, E Ferguson, B Bradley, C Scott, M Ozimek, A Haapala Chalk, and F Siddique. Evolution of trajectory design requirements on nasa's planned europa clipper mission. In *68th International Astronautical Congress (IAC)*, 2017.

[15] Brent Buffington, Nathan Strange, and John Smith. Overview of the cassini extended mission trajectory. In *AIAA/AAS Astrodynamics Specialist Conference and Exhibit*, page 6752, 2008.

[16] Stefano Campagnola, Arnaud Boutonnet, Johannes Schoenmaekers, Daniel J Grebow, Anastassios E Petropoulos, and Ryan P Russell. Tisserand-leveraging transfers. *Journal of Guidance, Control, and Dynamics*, 37(4):1202–1210, 2014.

[17] Stefano Campagnola, Brent B Buffington, Try Lam, Anastassios E Petropoulos, and Etienne Pellegrini. Tour design techniques for the europa clipper mission. *Journal of Guidance, Control, and Dynamics*, pages 1–12, 2019.

[18] Stefano Campagnola and Yasuhiro Kawakatsu. Jupiter magnetospheric orbiter: trajectory design in the jovian system. *Journal of Spacecraft and Rockets*, 49(2):318–324, 2012.

[19] Stefano Campagnola and Ryan P Russell. Endgame problem part 1: V-infinity-leveraging technique and the leveraging graph. *Journal of Guidance, Control, and Dynamics*, 33(2):463–475, 2010.

[20] Stefano Campagnola and Ryan P Russell. Endgame problem part 2: multibody technique and the tisserand-poincare graph. *Journal of Guidance, Control, and Dynamics*, 33(2):476–486, 2010.

[21] Stefano Campagnola, Paul Skerritt, and Ryan P Russell. Flybys in the planar, circular, restricted, three-body problem. *Celestial Mechanics and Dynamical Astronomy*, 113(3):343–368, 2012.

[22] Matteo Ceriotti. *Global optimisation of multiple gravity assist trajectories*. PhD thesis, 2010.

[23] Pablo Miguel Cincotta, Claudia Marcela Giordano, and C Simó. Phase space structure of multi-dimensional systems by means of the mean exponential growth factor of nearby orbits. *Physica D: Nonlinear Phenomena*, 182(3-4):151–178, 2003.

[24] Thomas F Coleman and Yuying Li. An interior trust region approach for nonlinear minimization subject to bounds. *SIAM Journal on optimization*, 6(2):418–445, 1996.

[25] Louis A D'Amario, Larry E Bright, and Aron A Wolf. Galileo trajectory design. *Space science reviews*, 60(1-4):23–78, 1992.

[26] Louis A D'Amario, Dennis V Byrnes, and Richard H Stanford. Interplanetary trajectory optimization with application to galileo. *Journal of Guidance, Control, and Dynamics*, 5(5):465–471, 1982.

[27] A David. Vallado. fundamentals of astrodynamics and applications. 1997.

[28] R Diehl, D Kaplan, and P Penzo. Satellite tour design for the galileo mission. In *21st Aerospace Sciences Meeting*, page 101, 1983.

[29] Fabio Ferrari, Michele Lavagna, Marc Scheper, Bastian Burmann, Ian Carnelli, et al. The european asteroid impact mission: Phase a design and mission analysis. In *Proceedings of AIAA/AAS Astrodynamics Specialist Conference, Vail, CO, USA*, 2015.

[30] D Garcia, P De Pascale, R Jehn, S Campagnola, C Corral, et al. Bepicolombo mercury cornerstone consolidated report on mission analysis. *ESA-ESOC Mission Analysis Office, MAO Working Paper*, (466), 2007.

[31] Frank W Gobetz. Optimum transfers between hyperbolic asymptotes. *AIAA Journal*, 1(9):2034–2041, 1963.

[32] Yanping Guo and Robert W Farquhar. New horizons mission design. *Space science reviews*, 140(1-4):49–74, 2008.

[33] R Haw, J Johannesen, A Halsell, M Wilson, and J Pojman. The gem extension satellite tour: Galileoâs mission across the millennium. *Adv. Astronaut. Sci., Astrodynamics*, 103:879–894, 1999.

[34] Andrew F Heaton, Nathan J Strange, James M Longuski, and Eugene P Bonfiglio. Automated design of the europa orbiter tour. *Journal of Spacecraft and Rockets*, 39(1):17–22, 2002.

[35] Dario Izzo, Victor M Becerra, Darren R Myatt, Slawomir J Nasuto, and J Mark Bishop. Search space pruning and global optimisation of multiple gravity assist spacecraft trajectories. *Journal of Global Optimization*, 38(2):283–296, 2007.

[36] Herbert B Keller. Global homotopies and newton methods. In *Recent advances in numerical analysis*, pages 73–94. Elsevier, 1978.

[37] Herbert B Keller. Lectures on numerical methods in bifurcation problems. *Applied Mathematics*, 217:50, 1987.

[38] CE Kohlhase and PA Penzo. Voyager mission description. *Space science reviews*, 21(2):77–101, 1977.

[39] Yuriy. V Kondratyuk. To those who will read to build.. 1938.

[40] Wang Sang Koon, Martin W Lo, Jerrold E Marsden, and Shane D Ross. The genesis trajectory and heteroclinic connections. In *AAS/AIAA Astrodynamics Specialist Conference*, pages 99–451, 1999.

[41] Wang Sang Koon, Martin W Lo, Jerrold E Marsden, and Shane D Ross. Heteroclinic connections between periodic orbits and resonance transitions in celestial mechanics. *Chaos: An Interdisciplinary Journal of Nonlinear Science*, 10(2):427–469, 2000.

[42] Alexei V. Labunsky, Oleg V. Papkov, and Konstantin G. Sukhanov. *Multiple gravity assist interplanetary trajectories*. Routledge, 1998.

[43] Try Lam, Juan J Arrieta-Camacho, and Brent B Buffington. The europa mission: multiple europa flyby trajectory design trades and challenges. 2015.

[44] Try Lam, Brent Buffington, and Stefano Campagnola. A robust mission tour for nasa's planned europa clipper mission. In *2018 Space Flight Mechanics Meeting*, page 0202, 2018.

[45] Gregory Lantoine, Ryan P Russell, and Stefano Campagnola. Optimization of low-energy resonant hopping transfers between planetary moons. *Acta Astronautica*, 68(7-8):1361–1378, 2011.

[46] Demyan Vasilyevich Lantukh et al. *Preliminary design of spacecraft trajectories for missions to outer planets and small bodies*. PhD thesis, 2015.

[47] Steve Matousek. The juno new frontiers mission. *Acta Astronautica*, 61(10):932–939, 2007.

[48] Steve Matousek and Andrey Sergeyevsky. To mars and back-2002-2020: Ballistic trajectory data for the mission architect. In *AIAA/AAS Astrodynamics Specialist Conference and Exhibit*, page 4396, 1998.

[49] Alexander May, Brian Sutter, Timothy Linn, Beau Bierhaus, Kevin Berry, and Ron Mink. Osiris-rex touch-and-go (tag) mission design for asteroid sample collection. 2014.

[50] Jay W McMahon and Daniel J Scheeres. Linearized lambert's problem solution. *Journal of Guidance, Control, and Dynamics*, pages 2205–2218, 2016.

[51] Michael A Minovitch. The determination and characteristics of ballistic interplanetary trajectories under the influence of multiple planetary attractions(ballistic interplanetary trajectories under influence of multiple planetary attractions- many-body problem). 1963.

[52] Daniel M Novak and Massimiliano Vasile. Improved shaping approach to the preliminary design of low-thrust trajectories. *Journal of Guidance, Control, and Dynamics*, 34(1):128–147, 2011.

[53] Fernando Peralta and Steve Flanagan. Cassini interplanetary trajectory design. *Control Engineering Practice*, 3(11):1603–1610, 1995.

[54] Anastassios E Petropoulos and James M Longuski. Shape-based algorithm for the automated design of low-thrust, gravity assist trajectories. *Journal of Spacecraft and Rockets*, 41(5):787–796, 2004.

[55] Anastassios E Petropoulos, James M Longuski, and Eugene P Bonfiglio. Trajectories to jupiter via gravity assists from venus, earth, and mars. *Journal of Spacecraft and Rockets*, 37(6):776–783, 2000.

[56] John E Prussing. Simple proof of the global optimality of the hohmann transfer. *Journal of Guidance, Control, and Dynamics*, 15(4):1037–1038, 1992.

[57] John E Prussing and Bruce A Conway. *Orbital mechanics*. Oxford University Press, USA, 1993.

[58] Javier Roa, Jesús Peláez, and Juan Senent. Spiral lambert's problem. *Journal of Guidance, Control, and Dynamics*, pages 2250–2263, 2016.

[59] Shane D. Ross and Daniel J. Scheeres. Multiple Gravity Assists, Capture, and Escape in the Restricted Three-Body Problem. *SIAM Journal on Applied Dynamical Systems*, 6(3):576–596, 2007.

[60] Johan Schoenmaekers and Rainer Bauske. Re-design of the rosetta mission for launch in 2004. In *18th International Symposium on Space Flight Dynamics*, volume 548, page 227, 2004.

[61] Haijun Shen and Panagiotis Tsiotras. Optimal two-impulse rendezvous between two circular orbits using multiple-revolution lambert's solutions. In *AIAA Guidance, Navigation, and Control Conference and Exhibit*, page 4844, 2002.

[62] Haijun Shen and Panagiotis Tsiotras. Using battin's method to obtain multiple-revolution lambert's solutions. *Advances in the Astronautical Sciences*, 116:1067–1084, 2003.

[63] Jon Andrew Sims, Andrew James Staugler, and James Michael Longuski. Trajectory options to pluto via gravity assists from venus, mars, and jupiter. *Journal of Spacecraft and Rockets*, 34(3):347–353, 1997.

[64] N J Strange, Ryan Russell, and Brent Buffington. Mapping the v-infinity globe. *AAS Paper*, (07-277), 2007.

[65] Nathan J Strange and James M Longuski. Graphical method for gravity-assist trajectory design. *Journal of Spacecraft and Rockets*, 39(1):9–16, 2002.

[66] Jonathan S Townley, Jonathan L Sharma, and Jarret M Lafleur. Cost-based launch opportunity selection applied to rendezvous with 99942 apophis.

[67] KT Uesugi. Space engineering spacecraft (muses) program in isas featuring its latest mission" hayabusa". In *International Conference on Recent Advances in Space Technologies, 2003. RAST'03. Proceedings of*, pages 464–471. IEEE, 2003.

[68] GB Valsecchi, EM Alessi, and A Rossi. An analytical solution for the swing-by problem. *Celestial Mechanics and Dynamical Astronomy*, 123(2):151–166, 2015.

[69] Giovanni B Valsecchi, Andrea Milani, Giovanni F Gronchi, and Steve R Chesley. Resonant returns to close approaches: Analytical theory. *Astronomy & Astrophysics*, 408(3):1179–1196, 2003.

[70] Massimiliano Vasile and P De Pascale. Preliminary design of multiple gravity-assist trajectories. *Journal of Spacecraft and Rockets*, 43(4):794–805, 2006.

[71] Benjamin F Villac and Daniel Jay Scheeres. Escaping trajectories in the hill three-body problem and applications. *Journal of guidance, control, and dynamics*, 26(2):224–232, 2003.

[72] Peter J Westwick. *Into the black: JPL and the American space program, 1976-2004*. Yale University Press, 2008.

[73] AA Wolf and JC Smith. Design of the cassini tour trajectory in the saturnian system. *Control Engineering Practice*, 3(11):1611–1619, 1995.

[74] Ryan C Woolley and Charles W Whetsel. On the nature of earth-mars porkchop plots. 2013.

[75] Ren Yuan, Cui Pingyuan, and Luan Enjie. Exploration opportunity search for near earth small body. In *2006 Chinese Control Conference*, pages 639–643. IEEE, 2006.